# AN OPTIMIZED DUAL-POLARIZED QUAD-RIDGED HORN ANTENNA WITH PYRAMIDAL SIDEWALLS

by

**Pieter Hugo van der Merwe**

Submitted in partial fulfilment of the requirements for the degree
Master of Engineering (Electronic Engineering)

in the

Department of Electrical, Electronic and Computer Engineering
Faculty of Engineering, Built Environment and Information Technology

UNIVERSITY OF PRETORIA

April 2013

# SUMMARY

## AN OPTIMIZED DUAL-POLARIZED QUAD-RIDGED HORN ANTENNA WITH PYRAMIDAL SIDEWALLS

by

**Pieter Hugo van der Merwe**

Supervisor: Prof. J.W. Odendaal

Co-Supervisor: Prof. J. Joubert

Department: Electrical, Electronic and Computer Engineering

University: University of Pretoria

Degree: Master of Engineering (Electronic Engineering)

Keywords: Quad-ridged horn antenna, dual-polarization, ultra wideband, higher order modes.

It is well known that quad-ridged horn antennas in general have impedance and radiation characteristics that are significantly worse than that of their double-ridged counterparts. Normally a voltage standing wave ratio (VSWR) of 3 over the operational bandwidth is used for the design specification of quad-ridged horn antennas. The bandwidth of operation is severely restricted due to the excitation of higher order modes in the co-axial to waveguide transition of the antenna. The higher order modes cause a break-up in the radiation pattern of the antenna and large dips in the boresight gain.

The performance of the quad-ridged horn antenna with pyramidal sidewalls is improved by separating the antenna into the transition and flared horn sections, and optimizing these sections individually. It is shown that a transition section with a pyramidal cavity and steps, and a flared horn section with an exponential profile with a circular segment for the ridges deliver the best performance. These configurations for the transition and flared horn sections are combined in the complete antenna. The optimized antenna has a 12.5:1 operational bandwidth with improved performance in terms of the VSWR, the coupling between the ports and the boresight gain. A prototype of this antenna is manufactured. Good agreement between the measured and simulated performance is achieved.

# OPSOMMING

## 'n GE-OPTIMISEERDE DUBBEL GEPOLARISEERDE KWAD-RIF HORING-ANTENNA MET PIRAMIDALE SYWANDE

deur

**Pieter Hugo van der Merwe**

Studieleier: Prof. J.W. Odendaal

Mede studieleier: Prof. J. Joubert

Departement: Elektriese, Elektroniese en Rekenaaringenieurswese

Universiteit: Universiteit van Pretoria

Graad: Magister in Ingenieurswese (Elektroniese Ingenieurswese)

Sleutelwoorde: Kwad-rif horing-antenna, dubbel gepolariseerde, ultra wyeband, hoër orde modusse.

Dit is bekend dat kwad-rif horing-antenna's oor die algemeen swakker impedansie en straling-eienskappe het as hulle dubbel-rif eweknieë. 'n Spannings-staande golf-verhouding (SSGV) van 3 oor die operasionele bandwydte word gewoonlik gebruik as 'n ontwerp-spesifikasie. Die bandwydte word erg beperk as gevolg van die opwekking van hoër orde modusse in die ko-aksiale tot gerifde golfleier-oorgang van die antenna. Die hoër orde modusse veroorsaak dat die stralings-patroon opbreek en groot variasies in die siglyn-wins ontstaan.

Die werkverrigting van die kwad-rif horing-antenna met piramidale sywande is verbeter deur die antenna te verdeel in die oorgang- en horing-gedeeltes, en hierdie gedeeltes individueel te optimiseer. Daar word aangetoon dat 'n oorgang-gedeelte met 'n piramidale holte en trappe, en 'n horing-gedeelte met 'n eksponensiële profiel met 'n ronde segment vir die riwwe die beste werkverrigting lewer. Hierdie konfigurasies vir die oorgang- en die horing-gedeeltes is bymekaar gevoeg in die volledige antenna. Die optimale antenna het 'n 12.5:1 operasionele bandwydte met verbeterde prestasie in terme van die SSGV, die koppeling tussen die inset-poorte en die siglyn-wins. 'n Prototipe van hierdie antenna is

vervaardig. Goeie ooreenkoms tussen die gemete en gesimuleerde werkverrigting is behaal.

# ACKNOWLEDGEMENTS

This dissertation would not have been possible without the support of the following persons:

My Lord Jesus Christ, who has blessed me with the ability and strength to complete this work.

My love, Annine le Roux, who during the course of this work became my friend, girlfriend and fiancée. Since you have walked into my life, everyday has been a joy-filled adventure.

My beloved father and mother, Paul and Mia van der Merwe, who have always supported me and provided me with the opportunities to follow my dreams.

My supervisors, Professor Wimpie Odendaal and Professor Johan Joubert for all their patience and guidance. I am especially grateful for all the opportunities they created for me. I would also like to thank Mr. Lukas Naudé of the Compact Antenna Test Range for his assistance with the measurements.

My friend, Herman Carstens, for showing me how to develop the machine drawings of the designed antenna. Mr. Machiel van Niekerk, of M & H engineering, for the manufacturing of the prototype.

Lastly, I would like to thank the National Research Foundation for providing financial support for this work.

## LIST OF ABBREVIATIONS

| | |
|---|---|
| CNC | Computer Numerically Controlled |
| EM | Electromagnetic |
| FEM | Finite Element Method |
| FIT | Finite Integration Technique |
| MoM | Method of Moments |
| OMT | Orthomode Transducer |
| RF | Radio Frequency |
| SMA | SubMiniature version A |
| TE | Transverse Electric |
| TEM | Transverse Electromagnetic |
| VSWR | Voltage Standing Wave Ratio |

# TABLE OF CONTENTS

# CHAPTER 1 INTRODUCTION

## 1.1 Problem statement

The insertion of ridges into waveguide structures lowers the cut-off frequency of the dominant transverse electric (TE) mode to extend the bandwidth of operation [1]. Over the last 70 years numerous studies have been published that investigate the cut-off frequencies of the modes inside double-ridged [2]-[8] and quad-ridged waveguides [9]-[11] as a function of the geometric parameters. A horn antenna is formed by opening or flaring the sidewalls of a waveguide in order for the TE modes propagating inside the waveguide to propagate from the aperture of the antenna into free space. The concept of placing ridges inside the waveguide structure to extend the usable bandwidth can be applied to horn antennas as well. The first ridged horn antenna designs were published in 1964 [1]. It was shown in 1973 that it was possible to manufacture a double-ridged horn antenna with a short axial length with good characteristics over an 18:1 bandwidth [12]. Since then the 18:1 double-ridged horn antenna has become the preferred antenna to use as the source antenna in electromagnetic measurement facilities. Recently an improved design for a double-ridged horn antenna has been published with a VSWR of less than 2 and no break-up in the radiation patterns over the entire 1-18 GHz bandwidth [13]. In this design a gridded sidewall is used to improve the gain performance in the lower frequency band and the transition section is redesigned to help suppress the excitation of higher order modes that lead to a break-up in the radiation patterns [13].

Quad-ridged horn antennas are dual-polarized, i.e. they are able to transmit either the vertical or horizontal polarization or a combination of both polarizations. If a quad-ridged horn antenna is used as the source antenna in a measurement facility, the switching of polarizations can be done electronically rather than physically rotating the source antenna. Thus, the co- and cross-polarizations of the antenna undergoing tests can be measured in two consecutive sweeps in either the azimuth or the elevation plane, without any physical changes being made in the measurement set-up. Consequently, there is a higher level of measurement repeatability and measurement time can be reduced [14].

Quad-ridged horn antenna designs are published in different variations. These variations have either pyramidal ([15]-[24]), conical ([24]-[27]) or shaped sidewalls ([28]-[30]) or the

sidewalls are entirely removed as in the case of the open-boundary ([14] and [33]-[37]) and super-open-boundary variations ([38]).

The widest bandwidths for the different variations of the quad-ridged horn antenna are shown in Table 1.1. A comparison of all the published designs is given in Chapter 2. As can be seen from this table, the widest bandwidths achieved with quad-ridged horn antennas are still less than the 18:1 bandwidth achieved with their double-ridged counterparts. In almost all the variations of the quad-ridged horn antenna the value for the VSWR is also greater than 2 in portions of the operational bandwidth.

**Table 1.1.** Performance comparison of the different variations of published quad-ridged horn antennas with the widest bandwidths.

| **Variation** | **Widest bandwidth [Reference number]** | **Maximum value for the VSWR** | **Boresight gain range** |
|---|---|---|---|
| Pyramidal sidewalls | 13.25:1 [17] | 3 | 6.4-16.1 dBi |
| Conical sidewalls | 10:1 [25] | 2 | 12-22 dBi |
| Shaped sidewalls | 6:1 [28] | 2 | Not published |
| Open-boundary | 16:1 [37] | 2.5 | 4-17 dBi |
| Super-open-boundary | 15:1 [38] | 3 | 4-13 dBi |

Quad-ridged horn antennas with sidewalls support the transmission of TE polarized electromagnetic (EM) waves. In some of the variations of the quad-ridged horn antenna the sidewalls of the flared horn section have been removed (the open- and super-open-boundary variations) to achieve stable radiation patterns with no break-up in the main beam. As a result of this, a stable boresight gain without large dips in the gain is achieved. However, the removal of the sidewalls effectively changes the antenna into a dual-polarized transverse electromagnetic (TEM) horn antenna, which only supports the propagation of TEM modes, i.e. the mechanism of radiation is changed when the sidewalls are removed. The open-boundary variation can therefore be considered to be a variation of a Vivaldi antenna rather than a variation of a quad-ridged horn antenna [36].

In the years when the first ridged horn antennas were designed the dimensions for the different components of the antennas were determined empirically through the construction of a number of prototypes [1], [12]. Nowadays, the designs for the antennas are simulated and optimized with commercial software packages before any prototypes are manufactured. The traditional method for simulating antennas is to simulate the antenna as a complete unit. Recently is has been shown that a Vivaldi antenna used as a feed in a gridded antenna array can be divided into different sections which can be simulated and optimized separately [40]. Quad-ridged horn antennas can also be divided into two sections, namely the co-axial-to-ridged-waveguide transition (the feeding structure) and the flared horn sections. This method of dividing the antenna into sections has already been applied to successfully design an orthomode transducer for an open-boundary dual-polarized quad-ridged horn antenna [34]. It has also been applied to quad-ridged horn antennas with pyramidal sidewalls with narrow 3:1 bandwidths [21], [23]. Normally the transition section is analyzed as a separate unit, whereas the flared horn section is analyzed as part of the complete antenna. However, an in-depth study into how the performance of both sections can be improved has not yet been published.

The computing resources needed to simulate the quad-ridged horn antenna can be used much more efficiently and sparingly if the two sections are simulated separately. A typical step to optimize the performance of the quad-ridged horn antenna is to change one parameter of the transition section while the rest of antenna is left unchanged. In such a step of the optimization process a lot of time and memory resources can be saved if the transition section is simulated on its own rather than as a part of the complete antenna.

Quad-ridged horn antennas in general exhibit a VSWR performance that is significantly worse than that of their double-ridged counterparts. They also severely suffer from large gain variations and pattern break-up due to the excitation of higher order modes in the co-axial to ridged waveguide transition section. This results in severely restricted frequency bands over which the quad-ridged horn antenna shows satisfactory performance.

It is proposed that the performance of the quad-ridged horn antenna can be improved if the best configurations, for the transition and the flared horn sections, are found and connected together in the final design of the complete antenna. In this dissertation the performance of

the two sections is individually optimized through simulation. The ideal would be to achieve an 18:1 bandwidth for both polarizations of the antenna with a VSWR of 2 or less and a stable boresight gain with no deterioration in the radiation pattern across this bandwidth.

## 1.2 Scope and objectives

It is shown in Table 1.1 that the widest operational bandwidth, for quad-ridged horn antennas with sidewalls, has thus far been achieved with an antenna with pyramidal sidewalls. The main objective of this dissertation is the improvement of the performance of a quad-ridged horn antenna with pyramidal sidewalls. A design of an optimized antenna is developed through the employment of the technique to divide the antenna into the transition and flared horn sections. The size of [17], in terms of wavelength at the lowest frequency of operation, is used as a benchmark for the design. The antenna is optimized in terms of the VSWR and radiation characteristics such as the boresight gain. The scope and specific objectives of this dissertation are detailed in the points below.

- The development of accurate numerical models to predict the performance of the transition and flared horn sections. The transition and flared horn sections are simulated separately, which is faster and uses less memory than in the case when the complete antenna is simulated. The choice of numerical technique used in the simulations is based on the computational requirements for the wide bandwidth of analysis in this research.
- Three configurations for the transition section are investigated to determine which configuration delivers the best performance. The differences in the configurations include the shape of the cavity as well as the insertion of steps into the cavity. Higher order modes can be excited in the transition section. The higher order modes lead to a break-up in the radiation patterns and dips in the boresight gain of the complete antenna. The three configurations for the transition section are optimized in such a way to achieve a VSWR of less than 2 and suppress the excitation of higher order modes across the widest possible bandwidth of operation.
- A parametric study is performed on the best transition section to determine the effect of manufacturing tolerances on the performance.

- A parametric study is performed on the flared horn section to determine whether better performance can be achieved with a design for the complete antenna which has smaller boxed dimensions than that of [17].
- Four configurations for the flared horn section are investigated to determine which configuration delivers the lowest VSWR across the widest bandwidth. The differences between the configurations of the flared horn section are the profiles used to taper the ridges.
- The best configurations for the transition and flared horn sections are combined in the final design of the complete antenna. The aim is to develop an antenna that has a VSWR of equal or less than 2 and a stable boresight gain across the widest possible bandwidth. The complete antenna is simulated to predict the performance of a manufactured prototype.
- A comparison is made between the final design of the complete antenna and two other antennas where one of the other configurations is used for either the transition or flared horn sections. This comparison is used to confirm that when the best transition and flared horn sections are combined, the best performance is achieved.
- A comparison between the simulation results achieved with CST Microwave Studio and FEKO is performed to validate the accuracy of the results achieved with CST Microwave Studio.
- A prototype of the final design of the complete antenna is manufactured. The performance of the prototype is measured in the Compact Antenna Test Range of the University of Pretoria. The measured results are compared to the simulation results to validate the accuracy of the simulation model as well as the design approach. The VSWR, the coupling between the ports, the boresight gain and the radiation patterns of the prototype are measured.

## 1.3 Research contribution

The main research contribution of this dissertation is the development of an optimized quad-ridged horn antenna with pyramidal sidewalls. The antenna is optimized in terms of the VSWR and the boresight gain. The optimized antenna is developed through the application of the technique to separate the antenna into the transition and flared horn

sections and to optimize the performance of each section individually. This technique saves time and computer memory (RAM) resources.

A transition section with a pyramidal cavity and steps that connect the ridges to the backshort is identified as the best configuration to use for the transition section. The steps help to suppress the excitation of higher order modes. The gap between the ridges is identified as a critical parameter and the manufacturing tolerance of this parameter should be made as small as possible to achieve the desired performance. A flared horn section with an exponential profile with a circular segment for the ridges is identified as the best configuration to use for the flared horn section. The best transition and flared horn sections are combined in the final design of the complete antenna.

The final design has the same boxed dimensions (in terms of wavelength at the lowest frequency of operation) as that of [17]. The published design of [17] has a 13.25:1 operational bandwidth for a VSWR of less than 3, as shown in Table 1.1. The published design has a maximum VSWR of 3 for the front port. The maximum VSWR for the back port is 2.5. The measured VSWR of the published design is below 2 for 41% and 65% of the operational bandwidth of the front and back ports respectively. The measured coupling for the published design is below -25 dB for almost the entire operational bandwidth and is below -30 dB for approximately 57% of the bandwidth. Only a few values for the boresight gain at certain frequencies are given in [17], instead of a plot of the gain curve. Whether the published design suffers from dips in the boresight gain is unclear. The range for the measured boresight gain of the published design is 6.4 to 16.1 dBi.

The final design of the optimized antenna is simulated and it has the following performance characteristics:

- An operational bandwidth from 0.8 to 10 GHz, i.e. a 12.5:1 bandwidth.
- A simulated VSWR of less than 2 over the entire bandwidth for port 1. A maximum simulated VSWR of 2.2, with the simulated VSWR less than 2 over 94% of the bandwidth for port 2.
- The simulated coupling between the ports is less than -30 dB over the entire operational bandwidth.

- A relatively stable, simulated boresight gain with no dips larger than 2 dBi. The range for the gain is between 6.4 and 19.4 dBi for port 1 and between 6.8 and 18.9 dBi for port 2. Similar gain curves are achieved for the two input ports.

The end product of this research is a manufactured prototype of the final design. The performance characteristics of the prototype are listed below.

- The prototype has a 12.5:1 operational bandwidth from 0.8 to 10 GHz.
- Across this bandwidth a maximum measured VSWR of 2.7 and 2.3 is achieved for port 1 and port 2 respectively. The measured VSWR is equal to or less than 2 for 88% and 92% of the bandwidth of the respective ports.
- The measured coupling between the ports is below -25 dB from 0.8 to 2.5 GHz and below -30 dB across the rest of the bandwidth. The measured coupling is below -30 dB for 82% of the 0.8 to 10 GHz bandwidth.
- The measured boresight gain of the prototype is relatively stable with no dips larger than 3 dBi. The range for the measured boresight gain is between 6.2 and 19.2 dBi for port 1 and between 6.5 to 18 dBi for port 2. The measured boresight gain performance of the two input ports is very similar.

Good agreement is achieved between the simulated and measured results. The differences in the measured and simulated performance are ascribed to manufacturing tolerances as well as the non-perfect conditions of the measurement set-up. It is clear from the discussion above, on the performance of the published design of [17] and the optimized antenna, that an improvement in the performance of the quad-ridged horn antenna with pyramidal sidewalls has been achieved. Thus, the performance of the complete antenna has been successfully improved through the application of the technique to separate the antenna into the transition and flared horn sections and to optimize the performance of each section individually. This technique can also be applied to quad-ridged horn antennas with conical or shaped sidewalls as well to the open- and super-open-boundary variations of the antenna.

## 1.4 Overview of dissertation

This chapter provides the context of the research problem, the scope and objectives as well as presenting the research contributions of this dissertation. The outline of the rest of the dissertation is given below.

Chapter 2 is a literature survey that presents additional background. The chapter starts with a short discussion on square quadruple ridged waveguides. Thereafter all of the published designs of the different variations of the quad-ridged antennas are discussed. The modern day numerical methods used in the EM software packages are discussed and the advantages and disadvantages of each method are given. The choice of numerical method and consequently the choice of software package that is used for the simulations performed in this dissertation are presented.

Chapter 3 focuses on the co-axial to ridged waveguide transition. The simulation model of the transition section is discussed. A couple of ideas used in the published designs are incorporated into three different configurations for the transition section. The three configurations are optimized and the simulation results are shown. The excitation of the dominant and higher modes is investigated through the transmission coefficient. The best configuration to use for the transition section is identified. A parametric study is performed on the best transition section to determine the effect of manufacturing tolerances on the performance.

Chapter 4 presents the model used for the flared horn section of the antenna. A parametric study is performed to determine whether better performance can be achieved with a design of the complete antenna that has smaller boxed dimensions than those of [17]. Simultaneously this illustrates the effect of changing the length or aperture dimensions on the VSWR performance of the flared horn section. Four different configurations for the flared horn section are investigated to determine which profile for the ridges delivers the best performance. The best configuration is identified and used in the final design of the complete antenna.

Chapter 5 discusses the performance of the complete antenna when the transition and flared horn sections are combined. Comparisons are made between the optimized antenna,

where the best configurations for the sections are combined, and other antennas where one of the other configurations are used for either the transition or flared horn section. The mechanical implementation of a prototype of the optimized antenna is presented. The measured and simulated results are compared. The performance of the implemented antenna is evaluated in terms of VSWR, coupling between the input ports, boresight gain and radiation patterns. Differences between the measured and simulated results are discussed.

Chapter 6 concludes this dissertation. It summarizes the content of the dissertation and the research contribution of the dissertation. Suggestions for future research are also given.

# CHAPTER 2 BACKGROUND

## 2.1 Introduction

Horn antennas are usually used as standard calibration antennas to measure the gain of other antennas. The bandwidths of these standard gain horn antennas are usually limited to the standard waveguide frequency bands. A number of set-ups with different standard gain horns have to be built when the performance of the antenna undergoing tests are measured across a very wide bandwidth. Across these limited bandwidths, the standard gain horn antennas have very flat gain curves, i.e. there are no break-ups in their radiation patterns.

Ridges were first inserted into structures of horn antennas in the 1970s to extend the operational bandwidth. This was the birth of double- and quad-ridged horn antennas. In the past double- and quad-ridged horn antennas suffered from a break-up in the radiation patterns with consequent dips in the gain at certain frequency points. One solution to eliminate the break-up in the radiation patterns that has been published is to remove the sidewalls of the flared horn section [14], [48]. This solution has been applied to double- as well as quad-ridged horn antennas. However, it has been recently shown for double-ridged horn antennas that the removal of the sidewalls reduces the value of the boresight gain in the lower frequency portion of the bandwidth [13]. In the design of [13] metallic grids are used for the sidewalls of the flared horn section to improve the gain performance in the lower frequency portion of the band. The transition section is also redesigned to help suppress the higher order modes that cause the break-up in the radiation patterns. The design of [13] has a very stable gain curve across the 1-18 GHz bandwidth. It is theorised that if the higher order modes can be suppressed inside the transition section of a quad-ridged horn antenna with pyramidal sidewalls, the operational bandwidth can be extended where the antenna has good impedance and radiation characteristics.

Ridged waveguides are the building blocks of ridged horn antennas. An analysis of the modes inside the quad-ridged waveguide is therefore critical to get an understanding of how the higher order modes can be suppressed inside the transition section of the quad-ridged horn antenna. A short discussion of the modes inside the quad-ridged waveguide is given in section 2.2 of this chapter.

A number of different variations of quad-ridged horn antenna designs have been published. In this dissertation, the designs are classified according to the type of sidewalls used in the flared horn section of the antenna. The type of sidewalls used in the design has a significant effect on the radiation patterns of the antenna. In section 2.3 of this chapter, the different variations of quad-ridged horn antenna are discussed. The designs are compared in terms of operational bandwidth, VSWR, boresight gain and size. The designs with the widest operational bandwidths have already been identified in Chapter 1. The modifications to improve the performance of the different variations of quad-ridged horn antennas are also discussed.

The published quad-ridged horn antenna designs have been simulated in a couple of commercial software packages, like CST Microwave Studio, FEKO and HFSS. Each software package is based on a different numerical method. These numerical methods are discussed in section 2.4. The advantages and disadvantages of the numerical methods are given. It is crucial to understand the advantages and disadvantages of these methods as the choice of numerical method has an influence on the amount of computing resources, in terms of memory and time, required. Section 2.5 summarizes the content of this chapter and presents some of the most important findings.

## 2.2 Ridged waveguides

The important parameters that determine the cut-off frequencies of the modes are the width of the waveguide, *wg_w*, the width of the ridges, *r_w*, and the gap between the ridges, *r_g*, as shown in Figure 2.1. These parameters also determine the impedance of the ridged waveguide. In order to achieve a low value for the impedance a very small gap between the ridges must be used.

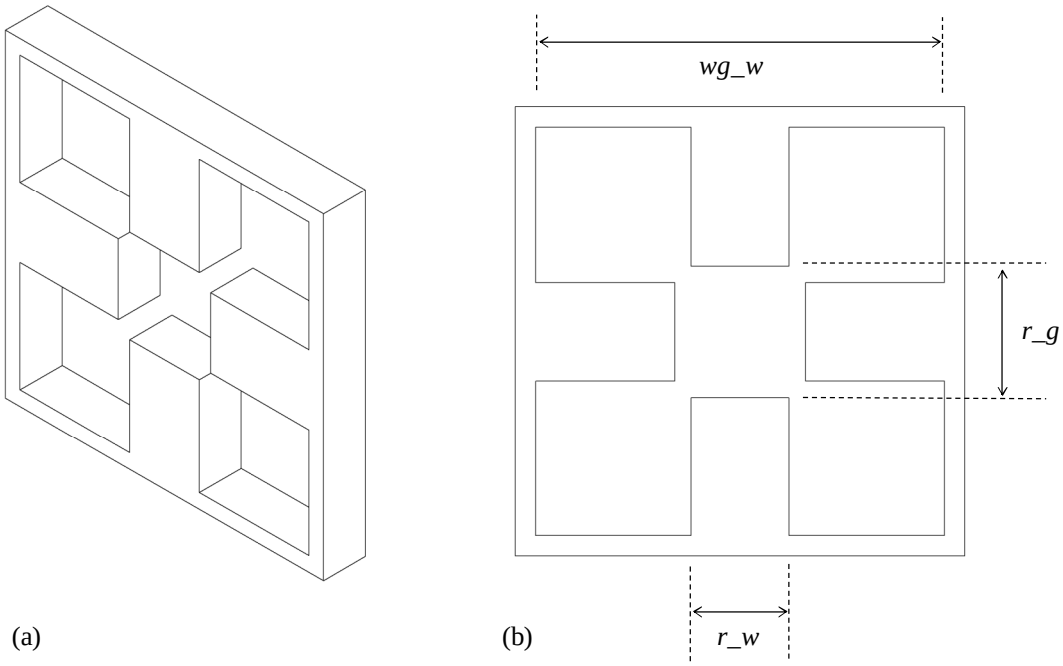


**Figure 2.1.** The square quad-ridged waveguide shown in (a) an isometric view and (b) a frontal view with the geometrical parameters.

The four lowest order modes that can propagate in a square quad-ridged waveguide are the $TE_{10}$, $TE_{11}$, $TE_{20L}$ and the $TE_{20U}$ modes [9]. The $TE_{20L}$ and $TE_{20U}$ modes are derived from the mode splitting of the $TE_{20}$ mode. The $TE_{20L}$ is evolved from two in-phase $TE_{20}$ modes, each polarized in one of two orthogonal directions, in a square waveguide. The $TE_{20U}$ is evolved from two anti-phase $TE_{20}$ modes in a square waveguide [9]. The field distributions in a waveguide with wg_w = 100 mm, r_w = 0.24*wg_w and r_g = 0.32*wg_w for the four lowest order modes are shown in Figure 2.2. These field distributions are found from simulations with CST Microwave Studio. The field distributions correspond with those published in [9]. It can be seen that for most of the modes the fields are confined to the edge of the ridges and the gap between the ridges, except for the $TE_{20U}$ mode. Thus, it can be theorised that if only the dominant mode is to be excited in the co-axial to ridged waveguide transition section of the antenna, efforts must be made to confine the fields to the edges of and the gap between the ridges.

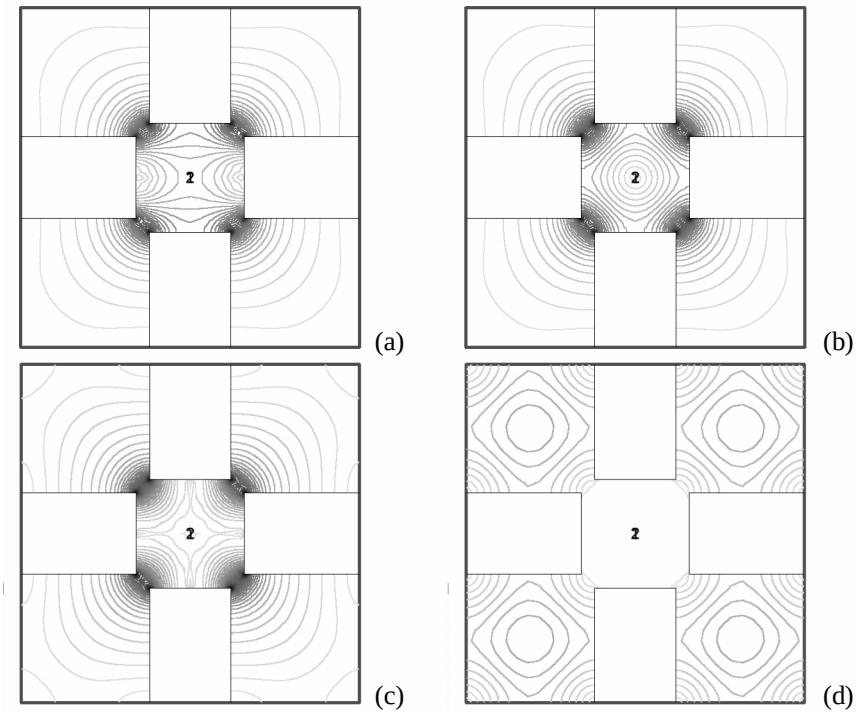


**Figure 2.2.** Electric field distribution of the four lowest order modes in a square quad-ridged waveguide. (a) $TE_{10}$, (b) $TE_{11}$, (c) $TE_{20L}$ and (d) $TE_{20U}$ mode.

The cut-off frequencies of these modes are found from the simulations to be

$$f_{c_{10}} = 0.80 \text{ GHz},$$

$$f_{c_{11}} = 0.84 \text{ GHz},$$

$$f_{c_{20L}} = 2.26 \text{ GHz and}$$

$$f_{c_{20U}} = 3.94 \text{ GHz}.$$

It is desirable that only the dominant mode is excited and propagated inside the ridged waveguide structure. The $TE_{11}$ mode has a cut-off frequency that is very close to that of the $TE_{10}$ mode. This corresponds to the findings of [9]. Therefore, there is a very narrow bandwidth of single mode operation. However, if the $TE_{11}$ mode is not excited the bandwidth is determined by the $TE_{10}$ and $TE_{20L}$ modes. The excitation of the $TE_{11}$ mode can be suppressed by making sure that the dominant mode is launched in a symmetrical waveguide structure, since the second lowest order is an odd mode [9]. It can be observed from the cut-off frequencies above that even if the $TE_{11}$ mode is not excited, the bandwidth between the $TE_{10}$ and the $TE_{20L}$ mode is only 2.26:0.80 = 2.83:1.

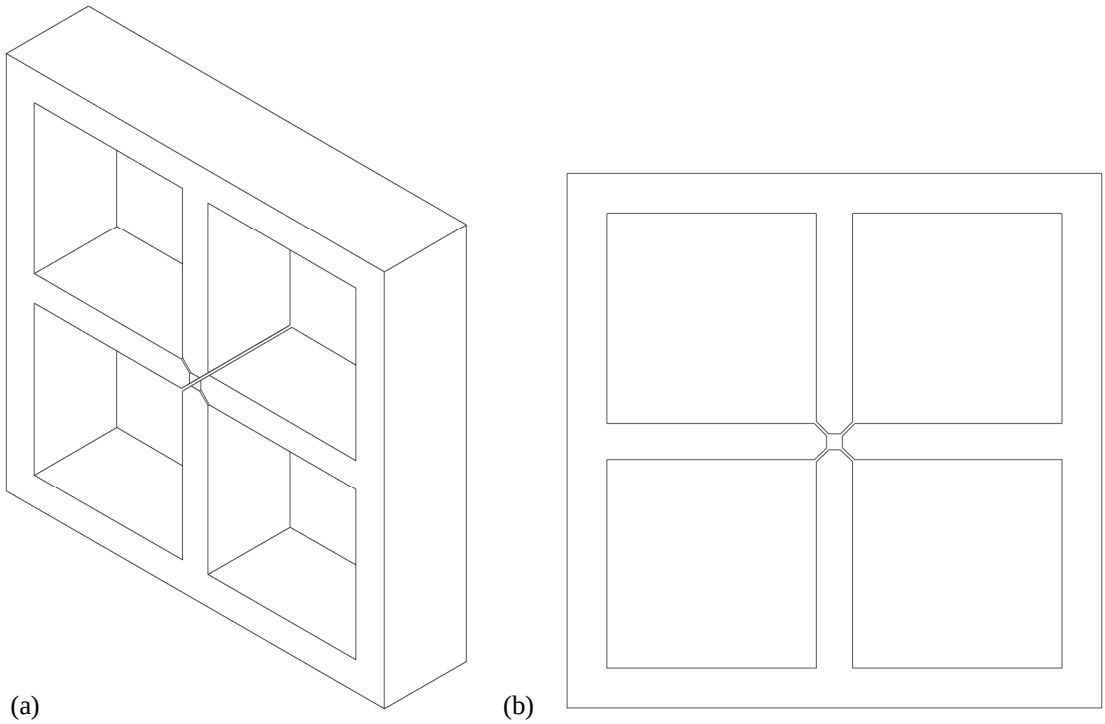


**Figure 2.3.** The square quad-ridged waveguide with chamfered ridges shown in (a) an isometric view and (b) a frontal view.

A bandwidth of up to 6:1 is achievable in a ridged waveguide with heavily loaded ridges, i.e. thin ridges with a small gap between them [9]. A smaller gap between the ridges can be achieved through the chamfering of the ridges. In the transition section that is discussed in Chapter 3 of this dissertation, chamfered ridges are used inside the waveguide as shown in Figure 2.3.

It is also clear that efforts must be made to suppress the excitation of higher order modes to extend the bandwidth where only the dominant mode propagates. An attempt is made to suppress the excitation of the higher modes in this dissertation through optimization of the geometrical parameters of the transition section.

## 2.3 Variations of quad-ridged horn antennas

In this dissertation, quad-ridged horn antennas are classified by the type of sidewalls they have. As mentioned in Chapter 1, quad-ridged horn antennas can have pyramidal, conical

or shaped sidewalls, or the sidewalls are entirely removed as in the open- and super-open-boundary variations.

A comparison of the different variations of the published quad-ridged horn antenna designs are given in Table 2.1, 2.3, 2.5, 2.7 and 2.9. The details of each design are discussed in Table 2.2, 2.4, 2.6, 2.8 and 2.10.

### 2.3.1 Quad-ridged horn antennas with pyramidal sidewalls

The quad-ridged horn antenna with pyramidal sidewalls is the focus of this dissertation. The widest bandwidth achieved in the published literature for this variation of the quad-ridged horn antenna is 13.25:1 of [17] as shown in Table 2.1. Across this bandwidth a maximum VSWR of 3 is achieved. One of the aims of this research is to achieve a VSWR equal to or less than 2 across the widest bandwidth, with no large dips in the boresight gain. This specification is to be met with a new antenna that has the same or smaller size (if possible) than the published design. The antenna design of [17] has a size of $1\times0.69\times0.69\,\lambda^3$ at the lowest frequency of operation. The boxed dimensions of the design of reference [17] are used as the benchmark for the antenna that is developed in this research.

**Table 2.1. A comparison of the published antenna designs with pyramidal sidewalls.**

| **Reference number** | **Bandwidth $f_L$ to $f_H$ GHz; $(f_H/f_L)$:1** | **Max. VSWR** | **Boresight gain range [dBi]** | **Length in mm and λ at $f_L$** | **Aperture size in $mm^2$ and $\lambda^2$ at $f_L$** |
|---|---|---|---|---|---|
| [15] | 2-12 GHz; 6:1 | 2.5 | 8.5-23 | $362.0$ mm $=2.4\lambda_{f_L}$ | $(114.3)^2$ mm$^2$ $=(0.76)^2\lambda_{f_L}^2$ |
| [16] | 3:1 | 3.5 | Not published. | $0.33\lambda_{f_L}$ | $(0.25)^2\lambda_{f_L}^2$ |
| [17] | 2-26.5 GHz; 13.25:1 | 3 | 6.4-16.1 | 150 mm $=1\lambda_{f_L}$ | $(104)^2$ mm$^2$ $=(0.69)^2\lambda_{f_L}^2$ |
| [18], [19] | 2-18 GHz; 9:1 | 3.5 | Not published. | 152 mm $=1.02\lambda_{f_L}$ | $(143)^2$ mm$^2$ |

| | | | | | |
|---|---|---|---|---|---|
| | | | | | $=(0.95)^2\lambda_{f_L}^2$ |
| [20] | 0.3-1.5 GHz; 5:1 | 1.8 | Not published. | 1320.8 mm $=1.32\lambda_{f_L}$ | $(914.4)^2$ mm$^2$ $=(0.91)^2\lambda_{f_L}^2$ |
| [21] | 8-18 GHz; 2.25:1 | 2.6 | 10.5-13 | 80 mm $=2.13\lambda_{f_L}$ | $(56)^2$ mm$^2$ $=(1.49)^2\lambda_{f_L}^2$ |
| [22] | 2-18 GHz; 9:1 | 2.2 | 7-15.5 | 140 mm $=0.93\lambda_{f_L}$ | $(100)^2$ mm$^2$ $=(0.67)^2\lambda_{f_L}^2$ |
| [23] | 1-3 GHz; 3:1 | 2.5 | 6.7-12.7 | Not published. | |
| [24] | 8-18 GHz; 2.25:1 | 2.2 | 10-11 | 87 mm $=2.32\lambda_{f_L}$ | $(60.5)^2$ mm$^2$ $=(1.61)^2\lambda_{f_L}^2$ |

**Table 2.2. Details of the published antenna designs with pyramidal sidewalls.**

| **Reference number** | **Transition section** | **Flared horn section** |
|---|---|---|
| [15] | A square cavity with steps is used. The edges of the ridges that point towards the backshort are chamfered. The insertion of the steps and the chamfering leads to an improvement of the VSWR and hence the widening of the operational bandwidth. | The profile for the ridges is a modified exponential function with 10 as the base instead of the natural number *e*. A linear taper is also applied to ridges to improve the VSWR performance. |
| [16] | The transition section is fed with a co-axial cable through the backshort. | The horn section of the antenna is not flared. Hence, the operational bandwidth of the antenna is limited to that of the ridged waveguide. The details of the profile for the ridges are not published, except that the ridges extend past the aperture. |
| [17] | A semi-spherical cavity is used. Steps connect the ridges to the backshort. Additional steps are inserted into the cavity for the one polarization as to | An exponential profile with a linear taper is used for the ridges. The additional linear taper improves the VSWR performance. |

| | | |
|---|---|---|
| | achieve an equal separation from the backshort for both input ports. This is done so that the input ports have approximately the same performance. | |
| [18], [19] | A square cavity is used. Ridges are connected to the backshort. No novel modifications are made to improve the performance of the transition section. | A modified exponential function with 10 as the base instead of the natural number *e* is used as profile for the ridges. The VSWR is further improved by applying an additional linear taper to the ridges. |
| [20] | Four ports are used to feed the antenna through a 180° hybrid. Opposing pairs of ports feed into the back face of the ridges. This is done to achieve good VSWR performance for both polarizations of the antenna. | No modifications are made to the sidewalls. The details of the profile used for the ridges are not published. Resistive films strips are added in the flared horn section to achieve an amplitude taper across the E-plane. This balances the E- and H-plane beamwidths and consequently reduces the levels of the sidelobes. |
| [21] | Square cavity without steps. No novel modifications are made to the transition section to improve the performance. | A modified exponential function with a linear taper is used as the impedance taper to design the profile for the ridges. The flared horn section is divided into segments. The dimensions for the segments are determined through simulations of ridged waveguides. In the simulations, the dimensions of the gap between the ridges and the aperture of the waveguides are changed until the desired impedance of each section is achieved. |
| [22] | Pyramidal cavity without steps. The pyramidal cavity improves the VSWR performance. | The same process as that of [21] is used to design the profile of the ridges. The edges of the sidewalls at the |

| | | |
|---|---|---|
| | | aperture are changed from straight lines to arches. This is done to prevent the break-up of the radiation patterns at high frequencies. |
| [23] | Square cavity without steps. Tapered co-axial lines are used to improve the return loss and hence the VSWR performance. | An exponential profile is used for the ridges. |
| [24] | Square cavity without steps. The centre conductors of the orthogonal co-axial lines are bent around each other at the feed point. Thus, the two ports are located at the same position in the transition section. This leads to a reduction in the phase difference and coupling between the ports, which prevent a break-up in the radiation patterns. | The same profile as that of [21] is used for the ridges. |

### 2.3.2 Quad-ridged horn antennas with conical sidewalls

The field distributions inside the transition sections of the antennas with pyramidal and conical sidewalls differ. The antennas with pyramidal sidewalls have square ridged waveguides inside the transition sections whereas the antennas with conical sidewalls have circular ridged waveguides. The four lowest order TE modes inside the square ridged waveguide are the $TE_{10}$, $TE_{11}$, $TE_{20L}$, $TE_{20U}$ modes. The four lowest order TE modes inside the circular ridged waveguide are the $TE_{11}$, $TE_{01}$, $TE_{21L}$ and $TE_{21U}$ modes. Hence, The TE modes, and consequently the EM fields, that propagate in the antennas with conical sidewalls are different from the ones that are propagated in the variations with pyramidal sidewalls. However, the methods that are used to improve the performance of the antennas with pyramidal sidewalls can also be applied to the antennas with conical sidewalls. The widest bandwidth achieved with this variation of the antenna is 10:1 as shown in Table 2.3.

**Table 2.3. A comparison of the published antenna designs with conical sidewalls.**

| Reference number | Bandwidth $f_L$-$f_H$ GHz; $(f_H/f_L)$:1 | Max. VSWR | Boresight gain range [dBi] | Length in mm and $\lambda$ at $f_L$ | Size of aperture in $mm^2$ and $\lambda^2$ at $f_L$ |
|---|---|---|---|---|---|
| [24] | 8-18 GHz; 2.25:1 | 1.9 | 12-19 | $77$ mm $= 2.05\lambda_{f_L}$ | $\pi(31.6)^2$ mm$^2$ $= \pi(0.84)^2 \lambda_{f_L}^2$ |
| [25] | 10:1 | 2 | 12-22 | Not published. | Not published. |
| [26] | 8-18 GHz; 2.25:1 | 2.2 | 10-16 | $77$ mm $= 2.05\lambda_{f_L}$ | $\pi(31.6)^2$ mm$^2$ $= \pi(0.84)^2 \lambda_{f_L}^2$ |
| [27] | 5-15 GHz; 3:1 | 2.5 | 5-12.5 | $85.09$ mm $= 1.42\lambda_{f_L}$ | $\pi(15.24)^2$ mm$^2$ $= \pi(0.25)^2 \lambda_{f_L}^2$ |

**Table 2.4. The details of the published antenna designs with conical sidewalls.**

| Reference number | Transition section | Flared horn section |
|---|---|---|
| [24] | The inner conductors of the co-axial lines are bent around each other at the feed point. Hence, the feed lines are located at the same position of the transition section. This reduces the phase difference between the ports, which leads to a reduction in the squint of the radiation patterns. A truncated conical cavity is used to improve the VSWR performance. | The profile for the ridges is designed in such a way that the dimensions for the gap between the ridges and the radius of the flared horn section give an impedance transition which has an exponential shape. The dimensions are found through simulation. |
| [25] | The precise details of the inside of the transition section are not published. The dimensions for the ridges are found by evaluating the cut-off frequencies and propagation characteristics of ridged waveguides. | A dielectric lens is used to increase the boresight gain and thus the efficiency of the antenna. The profile for the ridges is designed by impedance matching at locations along the axial length by controlling the dimensions for the ridged waveguide. |
| [26] | The same design, except for the bent co- | |

| | | |
|---|---|---|
| | axial probes, as [24] is used. | |
| [27] | The precise details of the transition section are not published. | An exponential profile is used to taper the ridges. A dielectric lens is used to reduce the phase error at the aperture of the antenna leading to an increase of the efficiency of the antenna. |

### 2.3.3 Quad-ridged horn antennas with shaped sidewalls

The variations that have shaped sidewalls are used in radio astronomy applications as feed antennas for reflectors. Stable radiation pattern behaviour with constant beamwidth and a good return loss are critical performance specifications in radio astronomy. The shaped sidewall variations have a narrow bandwidth of operation, since the variation in the beamdwidth is too large if the bandwidth is increased. The widest bandwidth achieved thus far is 6:1 as shown in Table 2.5.

The antennas with shaped sidewalls either have square or circular waveguides inside their transition sections. This is similar to the antennas with pyramidal or conical sidewalls. However, the flared horn sections of these antennas differ from that of their counterparts. A non-linear profile is applied to flare the sidewalls open towards the aperture instead of simply flaring the sidewalls linearly, as in the case of the antennas with pyramidal and conical sidewalls. It has been observed that the conical quad-ridged horn antenna with shaped sidewalls delivers radiation patterns that are rotationally symmetric and have a reasonably constant 10 dB beamwidth [32]. It delivers better results than the pyramidal and diagonal variations with shaped sidewalls, thus making it ideally suited to be used as a reflector antenna feed.

**Table 2.5. A comparison of the published antenna designs with shaped sidewalls.**

| **Reference number** | **Bandwidth $f_L$-$f_H$ GHz; ($f_H$/$f_L$):1** | **Max. VSWR** | **Boresight gain range [dBi]** | **Length in mm and λ at $f_L$** | **Size of aperture in mm$^2$ and λ$^2$ at $f_L$** |
|---|---|---|---|---|---|
| [28], [29], [30] | 2-12 GHz; 6:1 | 2 | Not published. | $219.38$ mm $= 1.46\lambda_{f_L}$ | $\pi(140.27)^2$ mm$^2$ $= \pi(0.94)^2\lambda_{f_L}^2$ |

| | | | | | |
|---|---|---|---|---|---|
| [31], [32] | 0.75-3 GHz; 4:1 | 1.4 | 10-16 | 585 mm $=1.46\lambda_{f_L}$ | $\pi(240)^2$ mm$^2$ $=\pi(0.6)^2\lambda_{f_L}^2$ |

**Table 2.6. Details of the published antenna designs with shaped sidewalls.**

| Reference number | Transition section | Flared horn section |
|---|---|---|
| [28], [29], [30] | A mode suppressor is inserted into the transition section in the form of a metallic ring at the feed point. | An exponential profile is used for the sidewalls of the flared horn section as well as for the ridges. Aperture matching is done where the sidewalls are curved back at the aperture. |
| [31], [32] | The transition section has a truncated conical cavity and steps connect the ridges to the backshort. | Sidewalls and ridges with elliptical profiles are used in the flared horn section. |

### 2.3.4 Open-boundary quad-ridged horn antennas

The variation of the antenna where the sidewalls are removed can be considered to be a variation of the Vivaldi antenna [36]. The antennas propagate quasi-TEM modes instead of pure TE modes since there are no sidewalls, i.e. each individual polarization transitions from a co-axial line to a two conductor balanced transmission line. The open-boundary variations typically have lower values for the boresight gain, at the low frequency portion of the operational bandwidth, than the variations with pyramidal, conical or shaped sidewalls. A 16:1 bandwidth for a VSWR of less than 2.5 has been achieved as shown in Table 2.7.

**Table 2.7. A comparison of the published open-boundary antenna designs.**

| Reference number | Bandwidth $f_L$-$f_H$ GHz; $(f_H/f_L)$:1 | Max. VSWR | Boresight gain range [dBi] | Length in mm or λ at $f_L$ | Size of aperture in mm$^2$ or λ$^2$ at $f_L$ |
|---|---|---|---|---|---|
| [14], [33] | 2-18 GHz; 9:1 | 3 | 6-14 | 152.4 mm $=1.02\lambda_{f_L}$ | $(152.4)^2$ mm$^2$ $=(1.02)^2\lambda_{f_L}^2$ |

| | | | | | |
|---|---|---|---|---|---|
| [34] | 1-15 GHz; 15:1 | 2 | 5-14 | Not published. | Not published. |
| [35] | 0.6-6 GHz; 10.1 | 3 | 1-15 | $348$ mm $= 0.7\lambda_{f_L}$ | $(288)^2$ mm$^2$ $= (0.57)^2 \lambda_{f_L}^2$ |
| [36] | 1-3 GHz; 3:1 | 1.7 | 9-14 | Not published. | Not published |
| [37] | 2-32 GHz; 16:1 | 2.5 | 4-17 | Not published. | Not published. |

**Table 2.8. The details of the published open-boundary antenna designs.**

| Reference number | Transition section | Flared horn section |
|---|---|---|
| [14], [33] | A semi-spherical cavity is used in the transition section to improve the VSWR. | The profile for the ridges is adapted from a double-ridged horn antenna design [48]. |
| [34] | An orthomode transducer (OMT) is optimized and used as the transition section of the antenna. A cylindrical cavity with steps is used. | The ridges have an exponential profile in the flared horn section. The ridges are added to the OMT to form the antenna. |
| [35] | A square shape is used for the cavity. Steps are inserted into the cavity. A diagonal quad-ridged waveguide is used for the transition section. | Although the design has no sidewalls in the flared horn section, a shorting strip is connected across the ridges to achieve a better VSWR. An exponential impedance taper is used to design the profile for the ridges. |
| [36] | The transition section has a semi-spherical cavity as the back of the ridges are tapered in a non-linear way towards the backshort. | The profile for the ridges has an exponential curve, which ends in a circular segment near the aperture. |
| [37] | A conical cavity is used. Steps connect the ridges to the backshort. | A new profile is used for the ridges. The ridges curl back at the aperture and the back wall of the ridges has a unique shape. This minimizes the diffraction from the aperture. |

### 2.3.5 Super-open-boundary quad-ridged horn antennas

The difference between the open- and super-open-boundary variations is that in the open-boundary variation the co-axial to ridged waveguide transition section still has sidewalls while in the super-open-boundary variation the sidewalls of the transition section are also removed. The idea to remove the sidewalls of the transition section came up when the open-boundary quad-ridged horn antenna was scaled to operate at the low frequency of 100 MHz. A simple scaling of the transition section of the open-boundary antenna required a transition section that was very big, heavy and difficult to manufacture. The removal of the sidewalls of the transition section made the manufacturing process easier and saved weight, whilst the performance of the antenna was not degraded [39]. The performance of this antenna is shown in Table 2.9. This variation of the antenna is closely related to the traditional TEM horn.

**Table 2.9. Performance of the published super, open-boundary antenna design.**

| Reference number | Bandwidth $f_L$-$f_H$ GHz; ($f_H$/$f_L$):1 | Max. VSWR | Boresight gain range [dBi] | Length in mm or λ at $f_L$ | Size of aperture in $mm^2$ or $\lambda^2$ at $f_L$ |
|---|---|---|---|---|---|
| [39] | 0.1-1.5 GHz; 15:1 | 3 | 4-13. | $1520\ mm^3 = 0.51\lambda_{f_L}$ | $(1670)^2\ mm^2 = (0.56)^2\lambda_{f_L}^2$ |

**Table 2.10. The details of the published super-open-boundary antenna design.**

| Reference number | Transition section | Flared horn section |
|---|---|---|
| [39] | The sidewalls of the transition section are removed to make the manufacturing easier. Steps connect the ridges to the backshort. | The ridges are made of lightweight honeycomb sandwiched in between thin aluminium sheets to save weight. The profiles of the ridges are similar to those of [14] and [33]. |

## 2.4 Numerical methods and software packages

The modern day radio frequency (RF) engineer can choose from a couple of EM simulation software packages to pick the one which is best suited for his or her needs.

Some of the most popular of these packages are CST Microwave Studio, FEKO and ANSYS HFSS. Each of these packages incorporates a number of solvers and each of these solvers uses a different numerical method. It should be noted that the quad-ridged horn antenna designs that have been published in the last decade, have been simulated in at least one of these software packages.

CST Microwave Studio incorporates both time and frequency domain solvers. The most flexibility is offered by the time domain solver, which can obtain the entire broadband frequency behaviour of the simulated device from only one calculation run. These solvers are remarkably efficient for most high frequency applications such as connectors, transmission lines, filters and antennas amongst others. The frequency domain solver is more suited to devices that are electrically small or have high Q values [41]. The finite integration technique (FIT) is the numerical method that is used in the time domain solver to find the EM properties of a modelled structure.

FEKO is a frequency domain solver. It incorporates a few different numerical methods as well as hybridisations between these methods. The size of the structure as well as the complexity of the materials determine which numerical method to use [42]. Since quad-ridged horn antennas consist mostly of metal with only small pieces of dielectric in the connectors of the co-axial cables and the size of the antenna is electrically relatively small, the method of moments (MoM) is the best choice of numerical method to use in FEKO.

A time and frequency domain solver is incorporated into ANSYS HFSS. The numerical method used in the solvers is based on the finite element method (FEM). The type of structure and the requirements of the RF engineer determine which solver to use [43].

The FIT, MoM and FEM are all full wave methods which are used to solve Maxwell's equations numerically in order to obtain the EM properties of a modelled structure. A short description with the advantages and disadvantages of each method follows below. A detailed discussion of these numerical methods can be found in [44] and [45].

### 2.4.1 Finite integration technique

The FIT discretizes the integral rather than the differential form of Maxwell's equations [44]. Hence the name of this technique. The FIT algorithm used in CST Microwave Studio is closely related to the finite difference time domain technique [45]. When this method is used in simulation, the entire structure of the model is broken down into a staggered grid. The grid can have either a Cartesian, or a cuboid hexahedral or a cylindrical coordinate form. A time integration scheme is applied to the grid through a leapfrog algorithm [44]. The input to the simulation is a pulse or time signal that has a certain pattern. The pattern of the signal or shape of the pulse depends on the smallest mesh size in the grid. This also determines the simulation time, since the shorter the pulse, the shorter the simulation time becomes. The transmitted and reflected signals are monitored, and as soon as a requirement, like the amount of energy left inside the structure is met, the simulation is stopped. The frequency spectrum of the modelled structure is then calculated by applying the Fourier transform to the transmitted and reflected time domain signals.

**Advantages:**

- A broadband frequency sweep can be done with a fine resolution in only one simulation. Therefore, no resonances can be missed due to a lack of calculation points in the frequency sweep.
- It can handle modelled structures with inhomogeneous materials, such as different dielectric layers, very efficiently.

**Disadvantages:**

- The FIT discretizes the entire structure of the model, instead of only the surfaces, as is the case with the MoM. Thus, the amount of memory required depends on the volume of the modelled structure and the size of the mesh cells.
- Resonances inside the structure can be excited by the input signal. This can lead to long simulation times since long after the input pulse signal has decayed away, the energy can be trapped inside the structure or only decay with a very slow rate. The simulation is stopped by placing a limit on the amount of energy left inside the structure. Frequency domain methods do not have this problem [44].

### 2.4.2 Method of moments

The MoM is a very widely used numerical technique to simulate radiating structures. The algorithm of the MoM replaces the physical structure of the model with equivalent surface currents. The MoM only discretizes the surface of the structure rather than the entire volume as in the case of FIT or FEM. It is particularly suited to model structures which consist mostly of metal parts [44]. Wires are represented as wire segments of surface currents, while surfaces are divided into triangular patches of surface currents. A matrix representation of the equivalent currents is thereafter derived. This matrix represents the effect of every wire or surface current on every other wire or surface current inside the matrix. The interaction of the elements of the matrix is computed through the application of the Green function. After the boundary conditions are applied to all the interactions between the elements, a set of linear equations is derived. The surface currents can then be calculated by solving the linear equations [45]. The EM properties (far field radiation patterns, VSWR, gain etc.) of the modelled structure can then be calculated from the surface currents. The MoM code of FEKO has been expanded with Planar Green functions, the surface equivalence principle (SEP) as well as the volume equivalence principle (VEP) to handle inhomogeneous dielectric materials (e.g. multilayered substrates) [42].

**Advantages:**

- The MoM is very efficient for structures that consist largely of metallic surfaces. Only the surface is meshed, and no free space or air region around the antenna needs to be meshed [45]. The amount of memory required depends on the surface area of the modelled structure and the size of the mesh segments or patches.
- The various properties of the antenna (radiation patterns, VSWR, gain etc.) can be easily calculated from the surface currents [45].

**Disadvantages:**

- It is a very memory intensive technique because the matrix used to represent the structure is not banded but populated almost entirely with non-zero elements [44].
- The properties of the modelled structure are calculated at discrete frequency points of the operational bandwidth. All of the calculations must be repeated at every discrete frequency point. The user specifies the number of frequency points in the simulations. If not enough points are used, resonances in the performance of the

modelled structure can be missed. The number of frequency points influences the simulation time.

- The MoM has a power of 6 scaling factor for the simulation time for an increase in the highest frequency of simulation. This means that a doubling in the value of the highest frequency of simulation can result in a simulation that runs 64 times longer [45].
- The MoM does not handle structures which consist of inhomogeneous materials (such as a structure with a number of dielectric regions) very efficiently. It can be used to simulate such structures but at a large expense of computational resources [45].

### 2.4.3 Finite element method

The FEM has its origins in mechanical engineering where it is used as a tool to analyze structural mechanics and thermodynamics [45]. The FEM can be applied in both the time and frequency domains. The FEM uses partial differential equations to solve Maxwell's equations subject to certain boundary conditions. The modelled structure is discretized into a finite element mesh. Triangular patches are used for surfaces and tetrahedrons are used for volumes. The basic principle of the FEM is to replace an unknown field or function on a domain with a set of elements with known shape but with unknown amplitude [45], similarly to the MoM. The FEM does not automatically incorporate the Sommerfeld radiation condition. Consequently, the mesh must be terminated in some way. This can be done by employing a numerical equivalent of an anechoic chamber through an artificial absorbing region inside the mesh [45]. The modern day FEM and FIT algorithms are very similar. The difference between the two is in the way material properties are discretized [44].

**Advantages:**

- The FEM handles structures that contain a large amount of dielectric materials quite efficiently, similarly to the FIT.
- It potentially has better frequency scaling than the MoM [45].

**Disadvantages:**

- If a very complex structure is modelled, the time it takes to generate the numerical mesh can start to exceed the actual simulation time [45]. This is especially true if a 3-dimensional structure is modelled, which requires a complex volumetric mesh.
- In the case where a structure that consists mostly of metal is modelled, the MoM is a much more effective method.

### 2.4.4 Choice of numerical method and software package

As quad-ridged horn antennas consist mostly of metal, only the FIT of CST Microwave Studio and the MoM of FEKO are considered. The broadband specification of this research requires that the entire frequency spectrum be simulated. If FEKO is used a large number frequency points has to be included in the simulation to ensure no resonances, narrow dips or spikes are missed in the performance of the antenna. This leads to simulations that take a very long time to complete. On the other hand, the transient domain solver of CST Microwave Studio, which uses the FIT, can determine the EM properties of the modelled antenna over the entire bandwidth from one single simulation run. Thus, CST Microwave Studio is the logical software package to use for the research conducted in this dissertation. FEKO is used as an additional method to verify the results obtained from simulations with CST Microwave Studio, since these two software packages incorporate different numerical techniques.

It is also observed that if the default settings are used for the mesh generation inside the two software packages, the simulations in CST Microwave Studio requires less computer memory than with FEKO for the same antenna model.

## 2.5 Summary

In this chapter additional background information on quad-ridged horn antennas was presented. The modes inside the square quad-ridged waveguide were discussed. The bandwidth of single mode operation was calculated from the cut-off frequencies of the different modes. It was discussed that a 6:1 bandwidth where only the dominant mode was propagated could be achieved with a ridged waveguide with very small gaps between the ridges. It was emphasised how important it was that the higher order modes should be

suppressed in the co-axial to ridged waveguide transition section of the antenna to extend the single mode operational bandwidth. If the higher order modes were not excited inside the transition section, stable radiation pattern behaviour could be achieved for the complete antenna.

The different variations of the published quad-ridged horn antenna designs were discussed. The antennas were classified according to the shape of the sidewalls in the flared horn section of the antenna. The designs were compared in terms of bandwidth, VSWR, boresight gain and size. For each variation of the antenna, the widest operational bandwidth was identified. The details of the published antennas were presented.

Lastly, some of the numerical methods used in the modern day EM simulation software packages were discussed. The advantages and disadvantages of each method were given. The conclusion was to use CST Microwave Studio for the simulations performed during the course of this research. FEKO was used as an additional method to verify the results obtained from the CST Microwave Studio simulations.

# CHAPTER 3 THE CO-AXIAL TO RIDGED WAVEGUIDE TRANSITION SECTION

## 3.1 Introduction

The co-axial to ridged waveguide transition acts as the connection between the complete antenna and the transmitter or receiver unit that is coupled to it. As such, it acts as the transformer of the TEM waves that are propagated along a co-axial cable to the TE modes that are propagated inside the ridged waveguide to the rest of the antenna. The aim is thus to design a transition section that is matched to the characteristic impedance of the input co-axial cables as well as to suppress the excitation of higher order modes inside the transition section, so as to minimize the amount of input power that is reflected back into the transmitter or receiver unit.

In this chapter the transition section is investigated. Two modifications to the transition section are identified in Chapter 2 as possible methods to improve the performance of the quad-ridged horn antenna with pyramidal sidewalls. This is to change the shape of the cavity and the insertion of steps into the cavity. These modifications are incorporated into three different configurations for the transition section that are discussed in section 3.2. The configurations are optimized in section 3.3 to determine which configuration delivers the best performance across the widest bandwidth. The performance is measured in terms of the VSWR and the suppression of higher order modes. The results of the optimization are shown and discussed in section 3.4. The best configuration to use for the transition section is identified from these results.

A parametric study is performed on the best transition section in section 3.5, to determine the effect of manufacturing tolerances (the deviation from the specified dimensions) on the performance of the transition section. The geometrical parameters that have a significant effect on the performance are identified. It is critical that the manufacturing tolerances for these parameters are kept as small as possible in order for the difference between the simulated and measured performance to be minimized. A summary of the chapter is given in section 3.6.

## 3.2 The different configurations

Three different configurations for the transition section, as shown in Figure 3.1 are investigated. Configuration I is the most basic with a rectangular cavity and no steps that connect the ridges to the backshort. Rectangular cavities are often used in the published quad-ridged horn antenna designs [15, 18, 19, 21, 23, 24 and 35]. The subsequent configurations are evolutions of the configurations that precede them. In configuration II the square cavity is replaced with a pyramidal cavity, similar to what is done in [22]. Then steps are inserted into the cavity to connect the ridges to the backshort in configuration III. Steps are used frequently in the published quad-ridged horn antenna designs [14, 15, 17, 28-35, 37-39]. However, the combination of a pyramidal cavity with steps is a novel design.

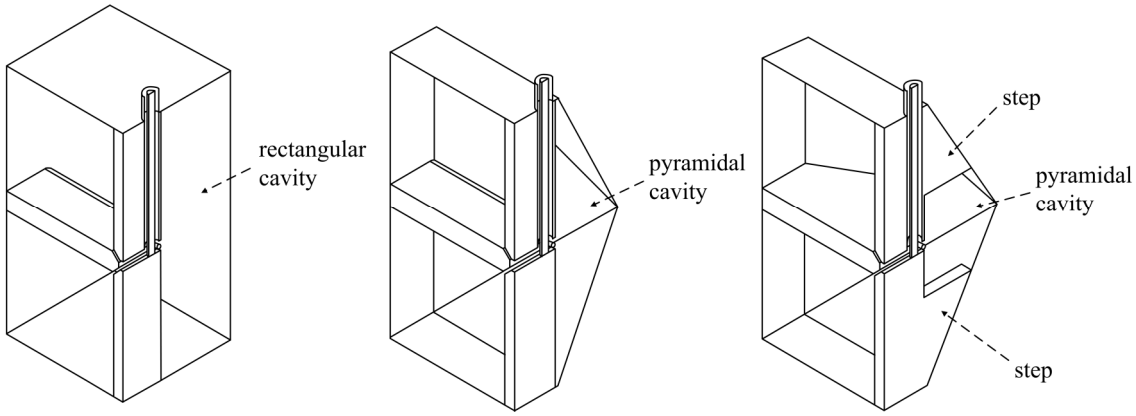


**Figure 3.1.** Section views through the three-dimensional structures of the different configurations used for the transition section. (Left) configuration I with a rectangular cavity, (middle) configuration II with a pyramidal cavity, (right) configuration III with a pyramidal cavity and steps.

The models for the transition section are excited by two orthogonal co-axial probes. No symmetry is used in the models. A waveguide port is put on the input face of each of the co-axial cables (Port 1 and 2). Another waveguide port is placed on the face of the ridged waveguide that leads to the rest of the antenna (Port 3). In CST Microwave Studio, a waveguide port is modelled as an infinitely long waveguide, thus acting as a perfectly matched load for the transition section. The ridges are chamfered at the feed point for a close fit, as the gap between the ridges is very small.

The geometrical parameters that determine the EM performance of the three different configurations of the transition section are shown in Figure 3.2 to Figure 3.4.

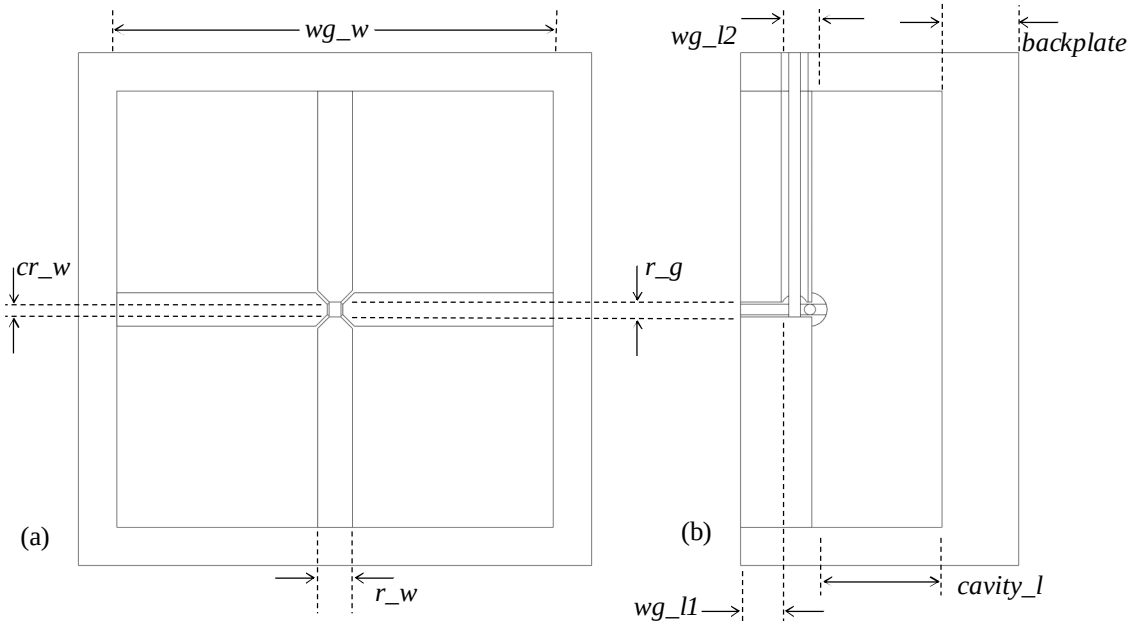


**Figure 3.2.** The geometrical parameters of configuration I of the transition section shown in (a), a front view and (b), a cross-section view.

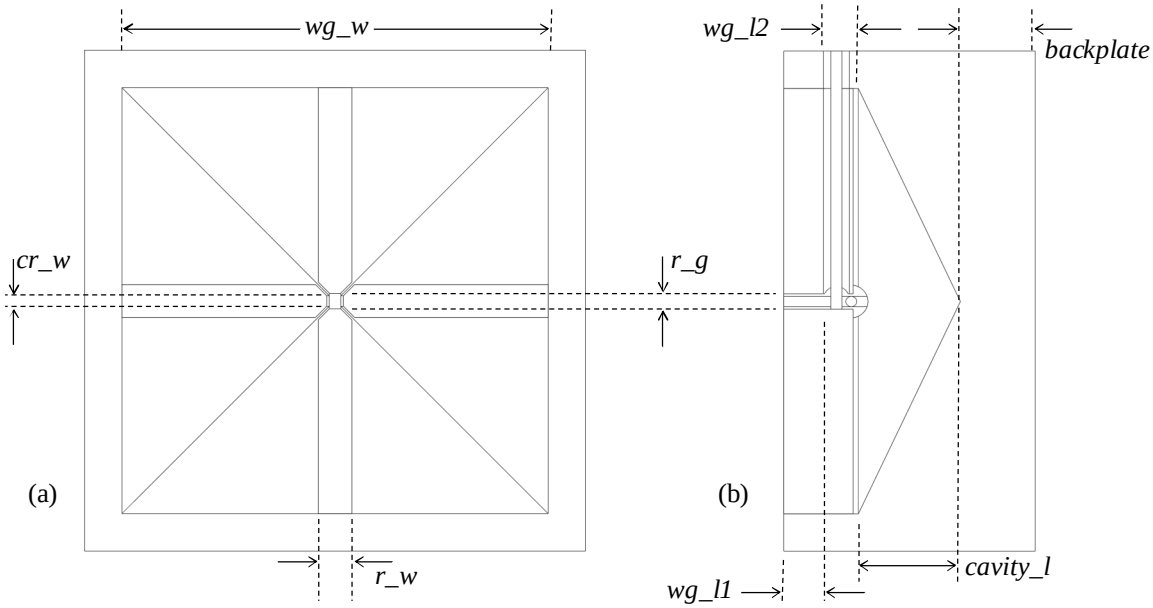


**Figure 3.3.** The geometrical parameters of configuration II of the transition section shown in (a), a front view and (b), a cross-section view.

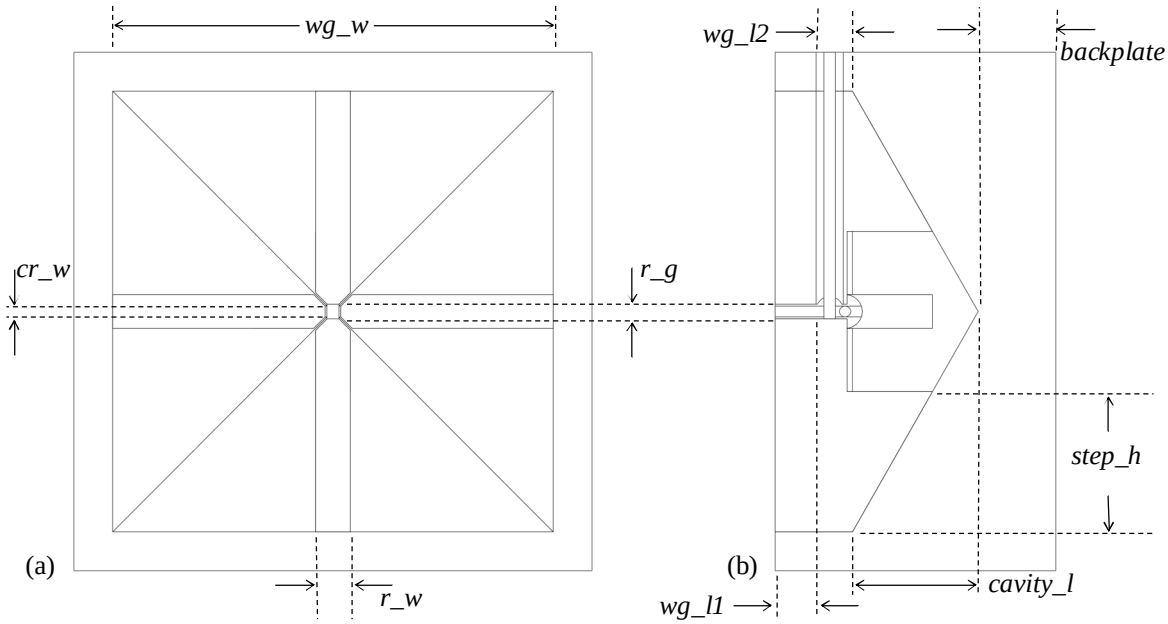


**Figure 3.4.** The geometrical parameters of configuration III of the transition section shown in (a), a front view and (b), a cross-section view.

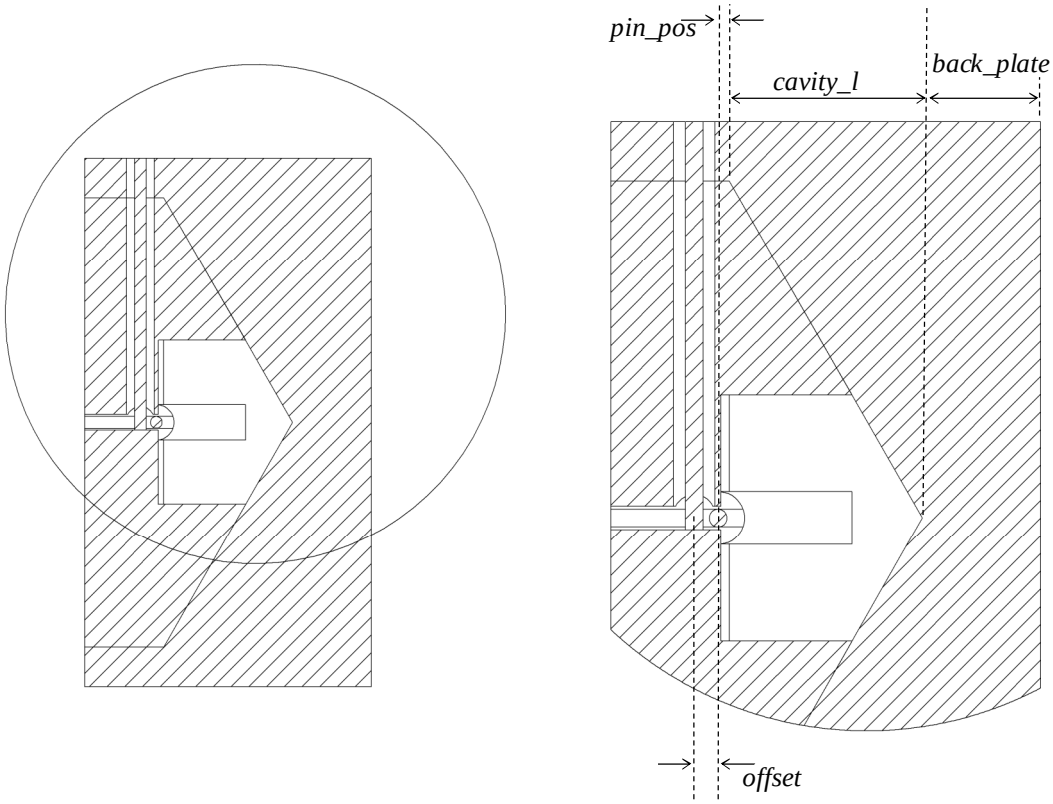


**Figure 3.5.** A detailed view of the parameters of the feed pins.

A more detailed view of the parameters of the two orthogonal feed pins is shown in Figure 3.5. A description of each of the parameters is given in Table 3.1. The built-in optimization

scheme of CST Microwave Studio is used to find the values of certain key geometrical parameters for all three configurations. This is discussed in the following section.

**Table 3.1.** The geometrical parameters of the transition section.

| **Name** | **Description** |
|---|---|
| *rad_inner* | Radius of the inner conductor of the co-axial cable |
| *rad_outer* | Radius of the outer conductor of the co-axial cable |
| *wg_w* | Width of the waveguide |
| *wg_h* | Height of the waveguide |
| *wg_l1* | Length of the first waveguide section |
| *wg_l2* | Length of the second waveguide section |
| *cr_w* | Width of the top edge of the chamfered ridge |
| *r_g* | Gap between the ridges |
| *r_w* | Width of the ridges |
| *cavity_l* | Length of the cavity |
| *step_h* | Height of the steps |
| *backplate* | Length of the backplate |
| *pin_pos* | Distance between the horizontal feed pin and the start of the cavity |
| *offset* | Distance between the centres of the orthogonal feed pins |

## 3.3 Optimization of the different configurations

All three configurations are optimized in CST Microwave Studio. The dimensions for the length of the cavity (*cavity_l*), the gap between the ridges (*r_g*) and the height of the steps (*step_h*) are used in the optimization to improve the performance. The ranges for the parameters in the optimization are

$$cavity\_l \in [10,25],$$

$$r\_g \in [2,5] \text{ and}$$

$$step\_h \in [10,25].$$

The starting value for *cavity_l* is chosen so that it is approximately equal to half a wavelength at 10 GHz (the highest frequency of operation.) The starting value for *r_g* is chosen so that the gap between the ridges is as small as possible, as this gives the widest separation between the cut-off frequency of the dominant mode and that of the next higher order mode [9]. The minimum value of *r_g* is limited by the width of the ridges. In this case the smallest possible value *r_g* is 2 mm, since *cr_w* is 1.5 mm. If *r_g* is smaller than 2 mm the gap between the ridges becomes too small. The starting value for *step_h* is chosen as the midpoint in the range of values for *step_h*. The maximum value of *step_h* is limited by the height of the ridges (which is defined by the height of the waveguide and the gap between the ridges). The values for the other parameters that are kept constant during the optimization process are shown in Table 3.2. These values are the same for all three configurations.

**Table 3.2.** The values for the constant parameters of the different transition sections.

| **Name** | **Value** |
|---|---|
| *rad_inner* | 0.75 mm |
| *rad_outer* | 1.75 mm |
| *wg_w* | 57 mm |
| *wg_h* | 57 mm |
| *wg_l1* | 4.6 mm |
| *wg_l2* | 4.7 mm |
| *cr_w* | 1.5 mm |
| *r_w* | 4.5 mm |
| *backplate* | 5 mm |
| *pin_pos* | 0.95 mm |
| *offset* | 2 mm |

The values for *rad_inner* and *rad_outer* are chosen to design an air-filled co-axial cable with a characteristic impedance of 50 Ω. Since the gap between the ridges is very small, the centre conductor of the co-axial has a small diameter (1.5 mm). However, the diameter of the centre conductor is not too thin to be difficult to manufacture. The value for *cr_w* is

equal to the diameter of the inner conductor of the co-axial cable, so that the inner conductor could be screwed into one of the ridges. The value for *cr_w* also ensures a small gap between the ridges. The values for *rad_inner* and *cr_w* place a limit on the minimum size for the gap between the ridges at the feed point. The value for *r_w* is chosen as 4.5 mm so that the ridges could be made from the standard aluminium plates that are commercially available, thus making the ridges easier to manufacture. The values for *wg_l1* and *wg_l2* are chosen in such a way that a Huber and Suhner subminiature version A (SMA) connector [46], can be connected to the side of the transition section of the antenna. The values for *wg_l1* and *wg_l2* also ensure that a hole does not have to be cut into the sidewalls of the flared horn section. A value of 2 mm is chosen as a minimum offset between the inner conductors of the two orthogonal co-axial cables that are used as the feeds. This ensures that approximately the same performance is achieved for both ports, while allowing enough space for the conductors not to touch. The parameters *r_g*, *cavity_l* and *step_h* are used in the optimization process described below.

The built-in optimization scheme of CST Microwave Studio is used. This software package allows the user to use a number of optimization algorithms, which work on a global or local basis. In this research a local interpolated quasi-Newton and a global CMA evolution strategy algorithm are used. All the optimization algorithms can simultaneously optimize several parameters.

The interpolated quasi-Newton method has a fast convergence rate. It makes use of the approximated gradient information to find local minima and maxima of a function [41]. It finds these minima and maxima by searching for the stationary points in the function where the gradient is zero, based on Newton's method.

The CMA evolution strategy is the abbreviation for Covariance Matrix Adaptation evolution strategy. In each iteration of this algorithm a set of possible solutions (values for the parameters used in the optimization algorithm) are generated by statistical variation (usually in a stochastic way). A set of possible solutions is efficiently sampled according to a multivariate normal distribution. The goal functions of the sampled solutions are evaluated and those solutions that deliver good results are selected for the next iteration (hence the evolution term). Pair wise dependencies between the parameters are defined in a

covariance matrix. The covariance matrix is updated as better and better solutions are selected during the course of this optimization algorithm. The sigma value (the standard deviation around the mean of the normal distribution) of the algorithm determines the initial step size and can be used to prevent the early convergence to a local minimum (large value for sigma), or to make the method search locally for a quick convergence (small value for sigma). This method can be thought of a hybrid local optimization with the robustness of a global optimization method [41]. It is observed during this research that the quasi-Newton method converged faster to a result that satisfied the specified goals, since the starting values for the parameters of the optimization are close to the optimum values.

The goals of the optimization are to achieve |S11| < -10 dB and $|S3_{TE\_1}1| = 0$ dB across the 0.8-10 GHz bandwidth. |S11| represents the reflection coefficient at the waveguide port of the co-axial feed (port 1). $|S3_{TE\_1}1|$ represents the transmission coefficient from the TEM mode in the waveguide port of the co-axial feed (port 1) to the dominant TE mode (TE_1) at the waveguide port at the output of the transition section (port 3). $|S3_{TE\_n}1|$ represents the transmission coefficient from the TEM mode in the waveguide port of the co-axial feed (port 1) to the $n_{th}$ TE mode (TE_n) at the waveguide port on the output face of the ridged waveguide transition (port 3). The specification that |S11| < - 10 dB requires that the impedance of the ridged waveguide is matched to the 50 Ω characteristic impedance at the feed point, as to minimize reflections. This also requires that the TEM mode travelling in the co-axial cable be easily converted into the dominant TE mode that travels inside the ridged waveguide. The optimization scheme is applied to all three configurations as shown in Figure 3.1. The values for the geometrical parameters after the optimization is completed are shown in Table 3.3.

**Table 3.3.** The optimized values for the parameters of the different transition sections.

| **Name** | **Configuration I** | **Configuration II** | **Configuration III** |
|---|---|---|---|
| *cavity_l* | 16.3 mm | 13.7 mm | 16.3 mm |
| *r_g* | 2.1 mm | 2.2 mm | 2.0 mm |
| *step_h* | No steps | No steps | 18.1 mm |

## 3.4 Simulation results of the optimization

### 3.4.1 The reflection and transmission coefficient

The simulation results for the magnitude of the S-parameters of the different, optimized transitions sections are shown in Figure 3.6 to Figure 3.8. $|S3_{TE\_1}1|$ is the transmission coefficient, which shows how much of the input power of the TEM mode travelling in the co-axial cable (Port 1) is coupled into the dominant TE mode that propagates in the ridged waveguide (Port 3). The frequency points at which there are losses in $|S3_{TE\_1}1|$ indicate that at these frequencies higher order modes are excited, since these modes receive some of the input power.

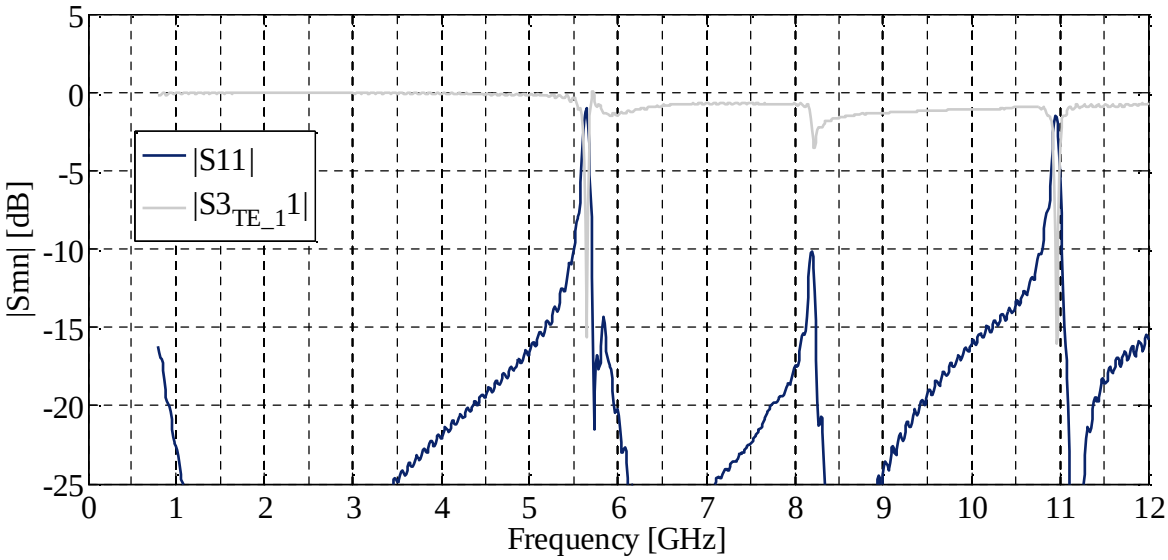


**Figure 3.6.** The magnitude of the S-parameters for configuration I.

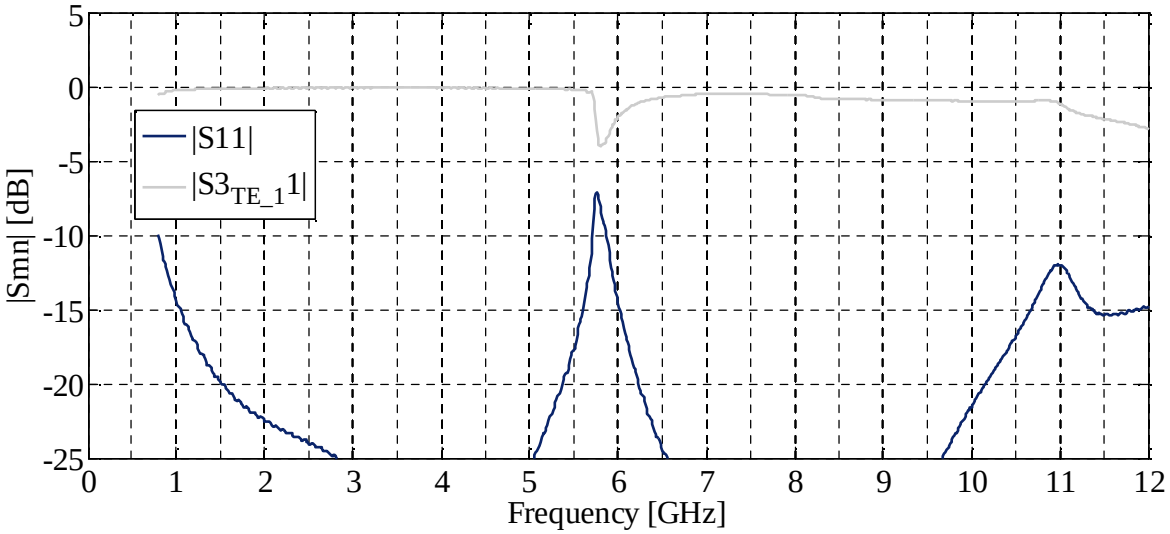


**Figure 3.7.** The magnitude of the S-parameters for configuration II.

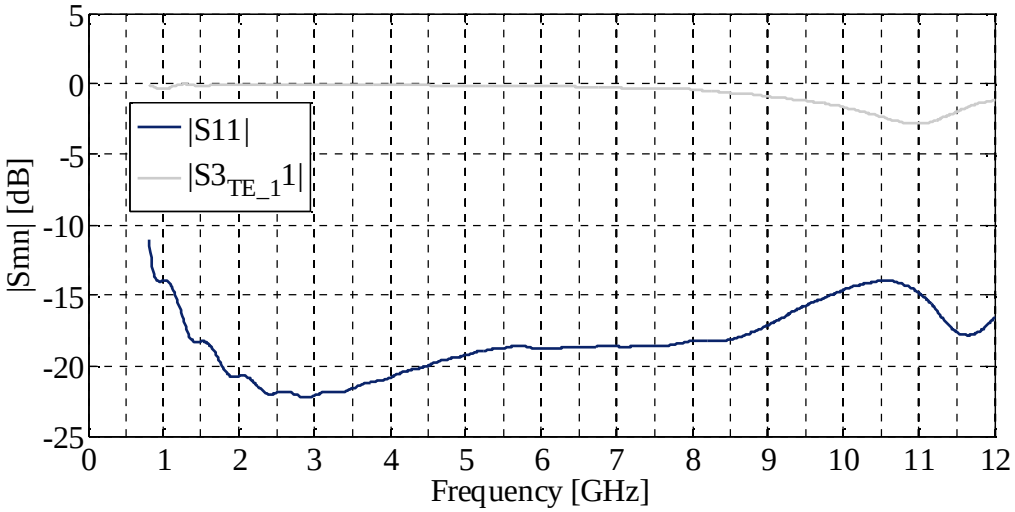


**Figure 3.8.** The magnitude of the S-parameters for configuration III.

It can be seen from Figure 3.6 that for configuration I there are deep, narrow dips in $|S3_{TE\_1}1|$, which coincide with large spikes in |S11|. At these frequency points the higher order TE modes are excited and start to propagate in the ridged waveguide. The first higher order modes for configuration I and II are excited at approximately 5.6 GHz. The dips in $|S3_{TE\_1}1|$ are smaller for configuration II, which indicate that less of the input power is coupled into the higher order modes. As soon as the steps are introduced into the transition structure the excitation of the higher order modes for the mid frequency band is suppressed, as can be seen in Figure 3.8. The first higher order modes for configuration III start to propagate at approximately 9 GHz.

It is expected that at the frequency points where the higher order modes start to propagate there are dips in the boresight gain of the complete antenna, since higher order modes cause break-ups in the radiation patterns of ridged horn antennas [13]. As the excitation of the higher order modes occurs at the highest frequency for configuration III, it is expected that the antenna with this configuration for the transition structure has the widest bandwidth before large dips in the gain occur.

### 3.4.2 The transmission coefficient of the dominant and higher order modes

The transmission coefficient, $|S3_{TE\_n}1|$, of the higher order modes, shows which of the higher order modes receive most of the input power, i.e. which higher order modes can be easily excited inside the ridged waveguide. The transmission coefficients of the dominant and higher orders modes for configurations I and III, after optimization, are shown in Figure 3.9 and Figure 3.11. Only the higher order modes for which $|S3_{TE\_n}1|$ goes above -10 dB are shown. Other higher order modes are excited, but their transmission coefficients are significantly smaller and can be neglected.

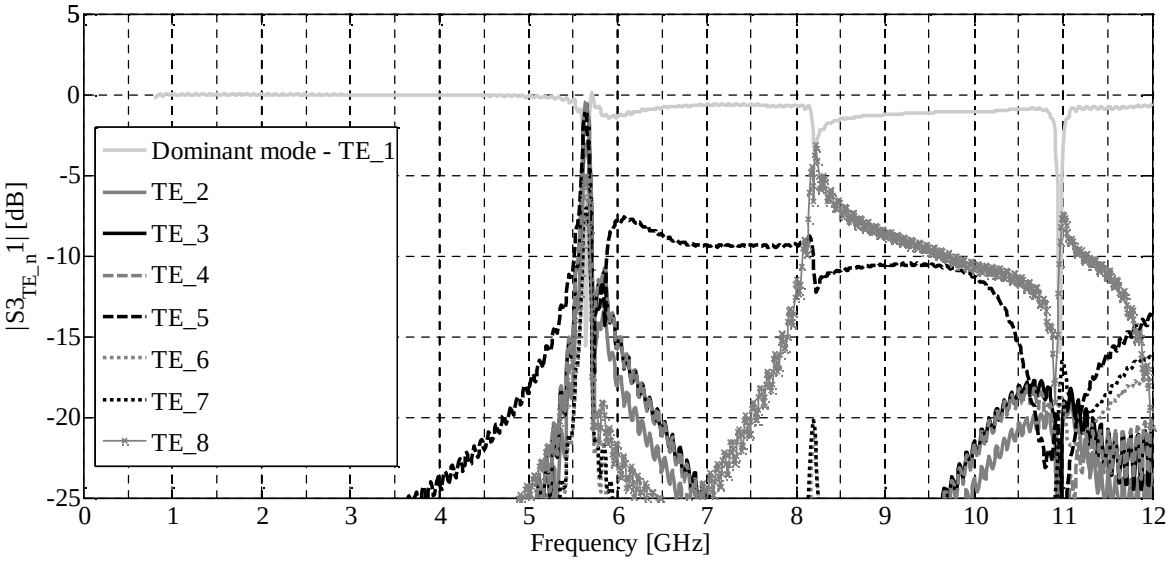


**Figure 3.9.** The transmission coefficient of the dominant and higher order modes for configuration I of the transition section.

The transmission coefficients for the different modes that are exited inside configuration I for the transition section is shown in Figure 3.9. It can be seen from this figure that at the points where there are sudden changes in $|S3_{TE\_1}1|$ of the dominant mode, there are

accompanying changes in the $|S3_{TE\_n}1|$ of the higher order modes. A dip in $|S3_{TE\_1}1|$ of the dominant mode indicates that instead of the input power of the TEM mode inside the co-axial cable being coupled into the dominant mode, some of the input power is coupled into one or more of the higher order modes instead. This is the case at approximately 5.6 GHz. At this frequency the first higher order modes are excited and start to propagate. The electric field distributions of the dominant and higher order modes (Figure 3.9) are shown in Figure 3.10.

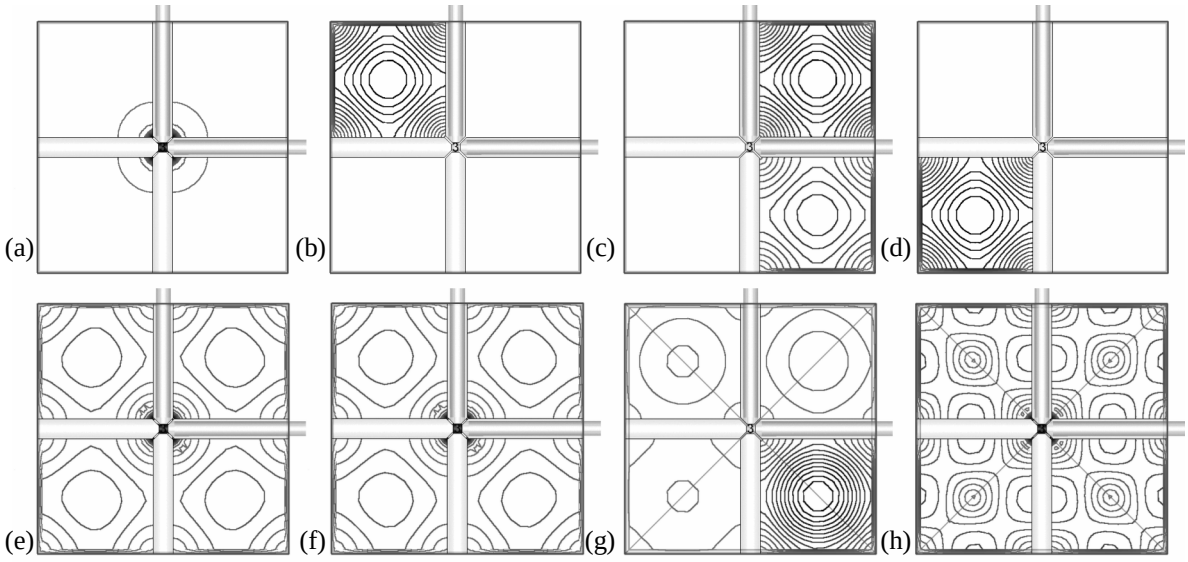


**Figure 3.10.** The field distributions of (a) the dominant modes and (b)-(h) the higher order modes in configuration I of the transition section.

The cut-off frequencies for the dominant and higher order modes shown in Figure 3.10 are found from the simulations to be

(a) $f_{c_{TE\_1}} = 0.59$ GHz,
(b) $f_{c_{TE\_2}} = 5.70$ GHz
(c) $f_{c_{TE\_3}} = 5.70$ GHz,
(d) $f_{c_{TE\_4}} = 5.70$ GHz,
(e) $f_{c_{TE\_5}} = 5.82$ GHz,
(f) $f_{c_{TE\_6}} = 5.83$ GHz,
(g) $f_{c_{TE\_7}} = 8.07$ GHz and
(h) $f_{c_{TE\_8}} = 8.15$ GHz.

It can be seen that the modes shown in Figure 3.10 (a), (b), (c), (d) and (g) do not have a symmetrical field distribution. The crosses in the field distributions of Figure 3.10 (g) and (h) indicate that these are evanescent modes. Consequently, these modes can only travel a short distance in a ridged waveguide with these dimensions before the modes are completely attenuated.

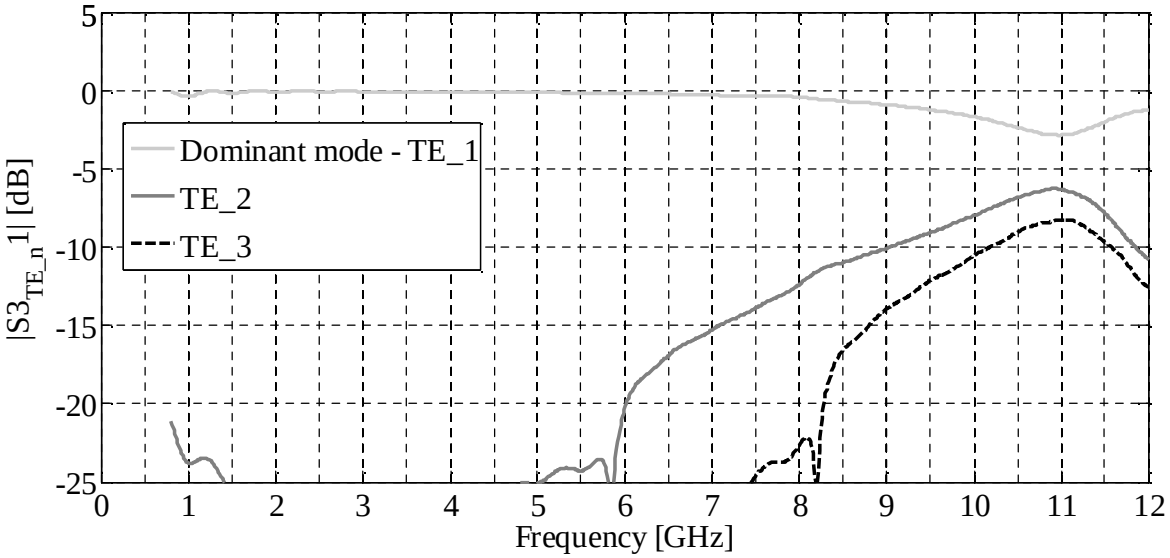


**Figure 3.11.** The transmission coefficient of the dominant and higher order modes inside configuration III for the transition section.

The transmission coefficients for the different modes that are excited inside configuration III for the transition section are shown in Figure 3.11. Only two higher order modes have values for $|S3_{TE\_n}1|$ that goes above -10 dB, instead of six higher order modes as in the case of configuration I. The value for $|S3_{TE\_n}1|$ for the higher order modes only goes above -10 dB at 9 GHz for configuration III instead of 5.6 GHz as in the case of configuration I. This gives an indication that the excitation of some of the higher order modes is suppressed in configuration III. Since configuration II has a similar $|S3_{TE\_1}1|$ curve for the dominant mode as configuration I, and both configurations have no steps inserted into the cavity, it is concluded that the insertion of the steps into the transition section of configuration III helps to suppress the excitation of higher order modes. The ideal would be that $|S3_{TE\_n}1|$ for the higher order modes stays below -15dB across the entire 0.8 to 10 GHz bandwidth. The electric field distributions of the modes that are excited inside configuration III for the transition section are shown in Figure 3.12.

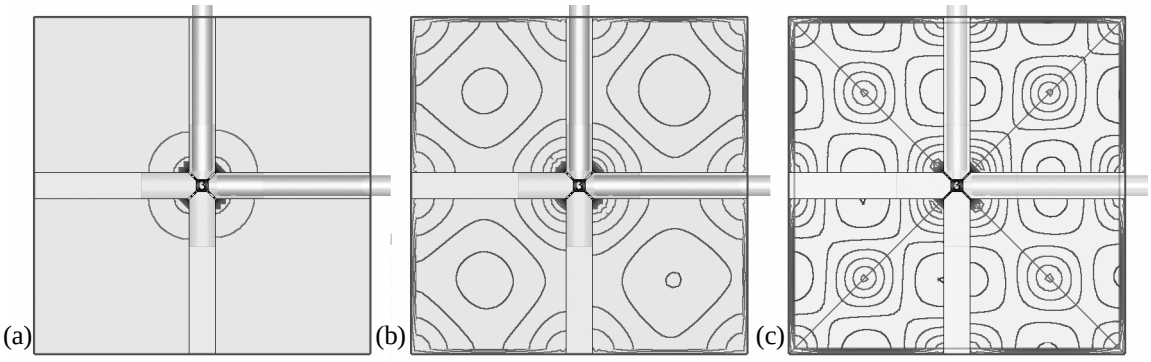


**Figure 3.12.** The field distributions of (a) the dominant mode and (b)-(c) the higher order modes for configuration III of the transition section.

It can be seen from Figure 3.10 and Figure 3.12 that the fields of the higher order modes are not confined to the edges and the gap between the ridges. It is theorised that this causes a break-up in the radiation patterns since most of the energy of the higher modes radiates into unwanted directions instead of in the boresight direction. Thus, the main beam splits into off-axis side beams with dips in the boresight gain. The cut-off frequencies for the modes inside configuration III are

(a) $f_{c_{TE\_1}} = 0.56$ GHz,

(b) $f_{c_{TE\_2}} = 5.81$ GHz and

(c) $f_{c_{TE\_3}} = 8.15$ GHz.

However, since the higher order modes only receive a significant amount of the input power above 9 GHz it is likely that the higher order modes only influence the radiation patterns of the antenna for this part of the operational bandwidth.

Configuration III is deemed to be the best configuration for the transition section as it delivers the best performance in terms of the reflection coefficient and the suppression of the excitation of higher order modes.

## 3.5 Parametric study of the best transition section

A parametric study, which gives a quantitative idea of how the geometrical parameters influence the performance of configuration III, follows below. The aim of the parametric

study is to determine the effect of manufacturing tolerances on the performance of the transition section. The critical geometrical parameters that have a significant effect on the performance are identified. The tolerances of these parameters must be kept as small as possible during manufacturing in order for the desired performance to be achieved. The geometrical parameters shown in Figure 3.2 to Figure 3.5 are used in the parametrical study. Only one parameter is changed during a certain parametric sweep, while the other parameters are kept to the dimensions shown in Table 3.4.

**Table 3.4.** The values of the parameters that are kept constant during the parametric sweeps.

| **Name** | **Values** |
|---|---|
| *rad_inner* | 0.75 mm |
| *rad_outer* | 1.75 mm |
| *wg_w* | 57 mm |
| *wg_h* | 57 mm |
| *wg_l1* | 4.6 mm |
| *wg_l2* | 4.7 mm |
| *cr_w* | 1.5 mm |
| *r_g* | 2 mm |
| *r_w* | 4.5 mm |
| *cavity_l* | 16.3 mm |
| *step_h* | 18.1 mm |
| *backplate* | 5 mm |
| *pin_pos* | 0.95 mm |
| *offset* | 2 mm |

### 3.5.1 Size of the waveguide

A change in the width and height of the waveguide (*wg_w* = *wg_h*), while the width of the ridges and the gap between the ridges are kept constant, changes the cut-off frequency of the dominant mode. This can be seen in Figure 3.13 of the VSWR, which decreases at the lower frequencies as the boxed dimensions of the waveguide are increased. The frequency

point where the VSWR goes below 2 determines the cut-off frequency of the dominant mode.

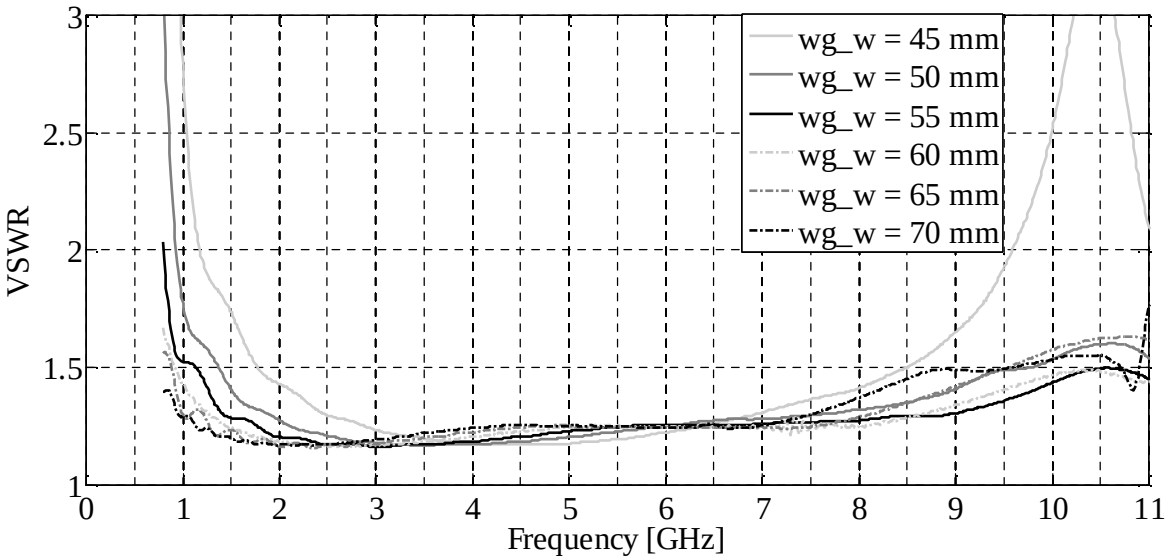


**Figure 3.13.** The VSWR of the transition as the width and height of the waveguide are changed.

At the higher frequency portion of the bandwidth it can be seen for *wg_w* = *wg_h* = 45 mm there is high spike in the VSWR. At this point a higher order mode starts to propagate. This shows that for these ratios of the ridge gap to the width of the waveguide, and the width of the ridges to the width of the waveguide, the cut-off frequencies of the dominant and next higher order mode are close to each other. This limits the bandwidth. The other values for the boxed dimensions of the waveguide produce ratios that deliver a wider gap between the cut-off frequencies of the dominant and next higher order modes. Consequently, a wider bandwidth is achieved. An increase in the boxed dimensions increases the impedance of the quad-ridged waveguide [9]. The effect of a change in the boxed dimensions of the waveguide is significant at the lower frequencies of the bandwidth.

### 3.5.2 Width of the ridges

A change in the width of the ridges influences the impedance of the ridged waveguide. An increase in the width of the ridges lowers the impedance of the quad-ridged waveguide, as can be seen from the plots in [9]. A decrease in the width of the ridges increases the impedance.

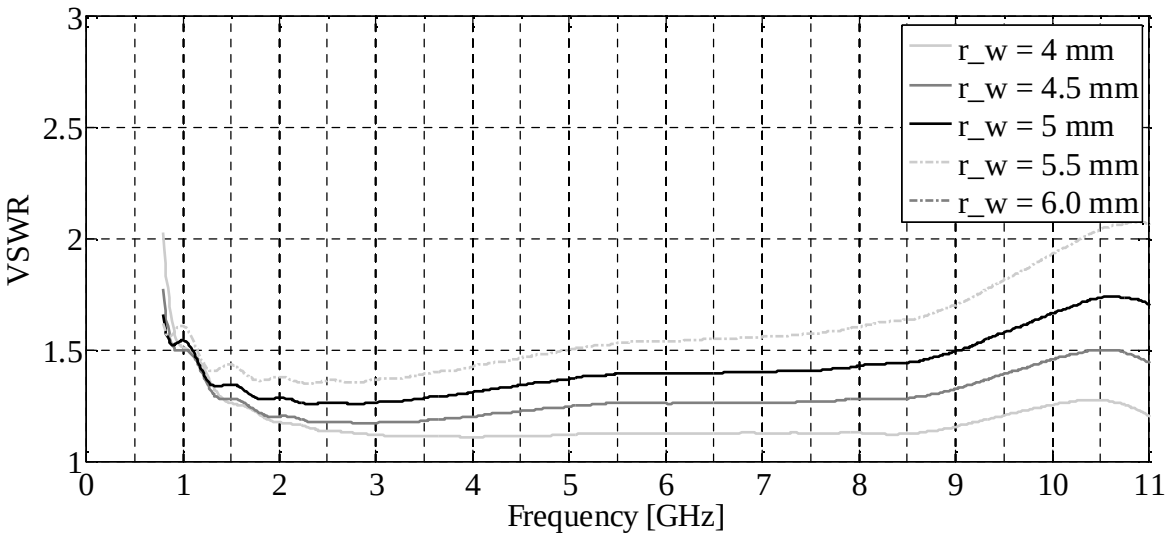


**Figure 3.14.** The VSWR of the transition section as the width of the ridges is changed.

Unlike the parameter *wg_w* (and consequently *wg_h*), the parameter *r_w* has a small influence on the lower frequency portion of the bandwidth. The effect of *r_w* is more pronounced in the higher frequency portion of the bandwidth. It can be seen from Figure 3.14 that the VSWR increases as the width of the ridges is increased. An increase in *r_w* lowers the impedance of the ridged waveguide, causing an impedance mismatch between the co-axial cable and the ridged waveguide.

### 3.5.3 Gap between the ridges

The gap between the ridges has a significant effect on the VSWR across the entire bandwidth, as can be seen from Figure 3.15. Therefore, it is a critical parameter and its manufacturing tolerance should be made as small as possible. Only a small change in the gap between the ridges causes an impedance mismatch between the co-axial cable and the ridged waveguide. The large impedance mismatch can be seen in the plot of the VSWR. An increase in the gap between the ridges increases the impedance of the quad-ridged waveguide and vice versa, as can be seen from the plots in [9].

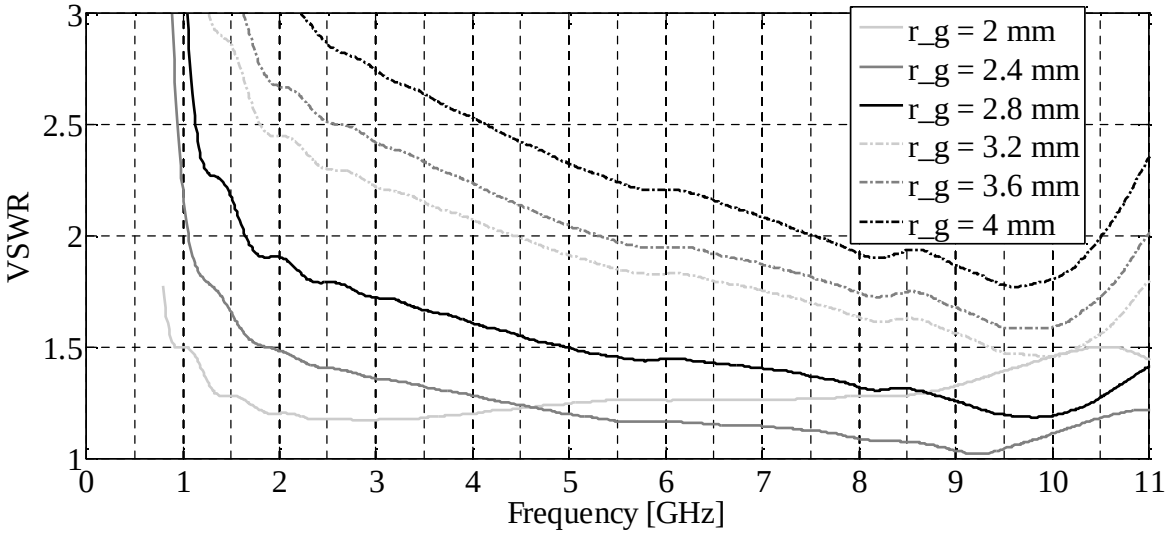


**Figure 3.15**. The VSWR as the gap between the ridges is changed.

### 3.5.4 Height of the steps

A change in the height of the steps does not make a significant change in the VSWR of the transition section, as shown in Figure 3.16. It is clear only a very large change (larger than 10 mm) in the dimension for step_h would make a drastic change in the VSWR. However, *step_h* can still be used in the optimization process to achieve the best possible performance for the transition section, as shown earlier in this chapter.

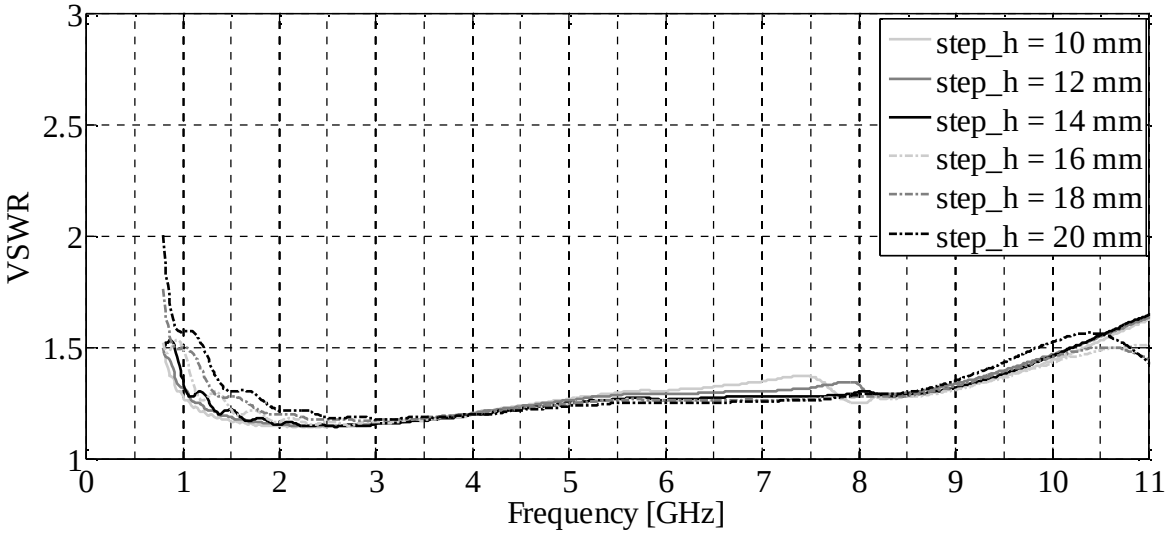


**Figure 3.16.** The VSWR of the transition section as the height of the steps is changed.

### 3.5.5 Length of the cavity

A change in the length of the cavity only produces small changes in the VSWR as shown in Figure 3.17. Thus, the height of the steps and the length of the cavity are not that critical. A large deviation in these parameters does not have a detrimental effect on the performance of the antenna.

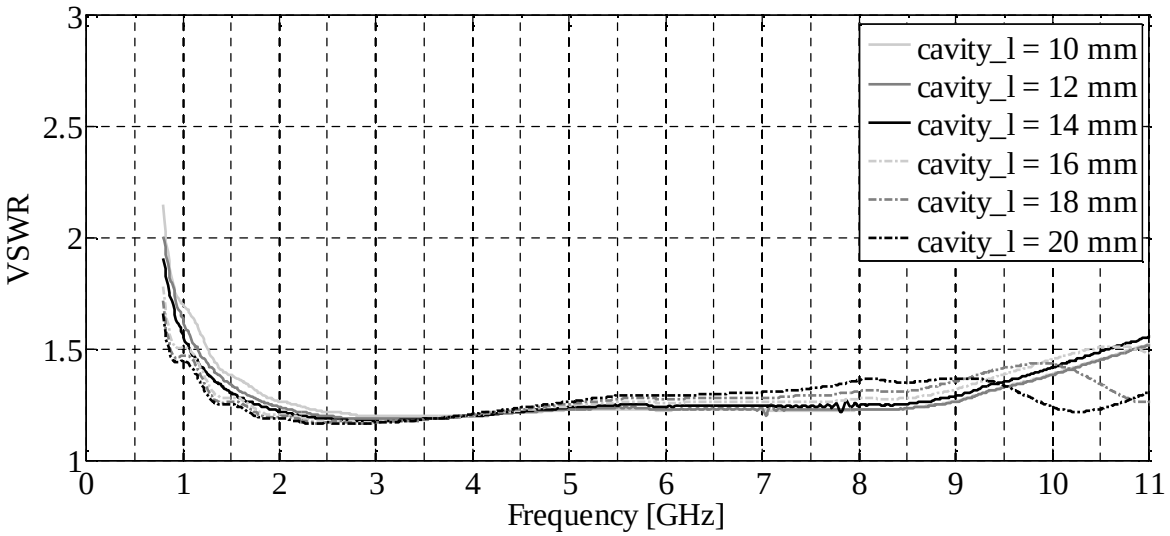


**Figure 3.17.** The VSWR of the transition section as the length of the cavity is changed.

### 3.5.6 Offset between the input ports

The dimension for the offset between the two input ports (input feed pins), i.e. the distance between the centre points of the two inner conductors of the co-axial cables, has a very small effect on the VSWR of the transition section as shown in Figure 3.18.

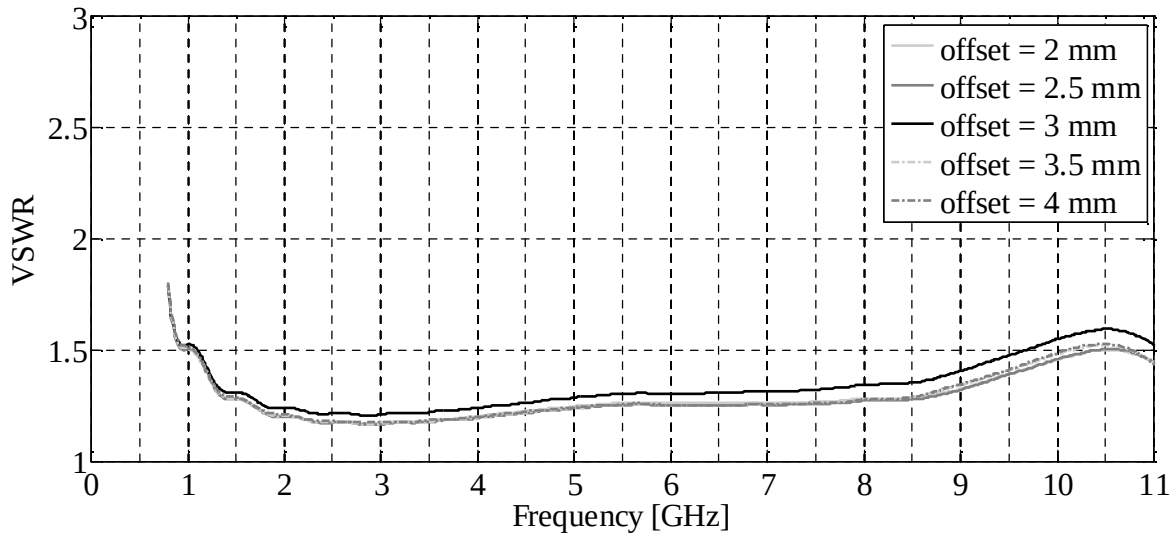


**Figure 3.18.** The VSWR of the transition section as the distance between the two input feed pins is changed.

However, this parameter has a significant effect on the coupling (and thus the isolation) between the ports as shown in Figure 3.19. A change of 0.5 mm produces a 5dB and larger change in the coupling between the ports. Thus, the isolation between the ports can be controlled by changing the offset between the ports. However, if the offset between the ports is quite large the performance of the two ports will differ. A large offset also produces a phase difference between the ports with deterioration in the radiation patterns of the antenna [24]. Thus, a trade off is made between the isolation and the other performance requirements.

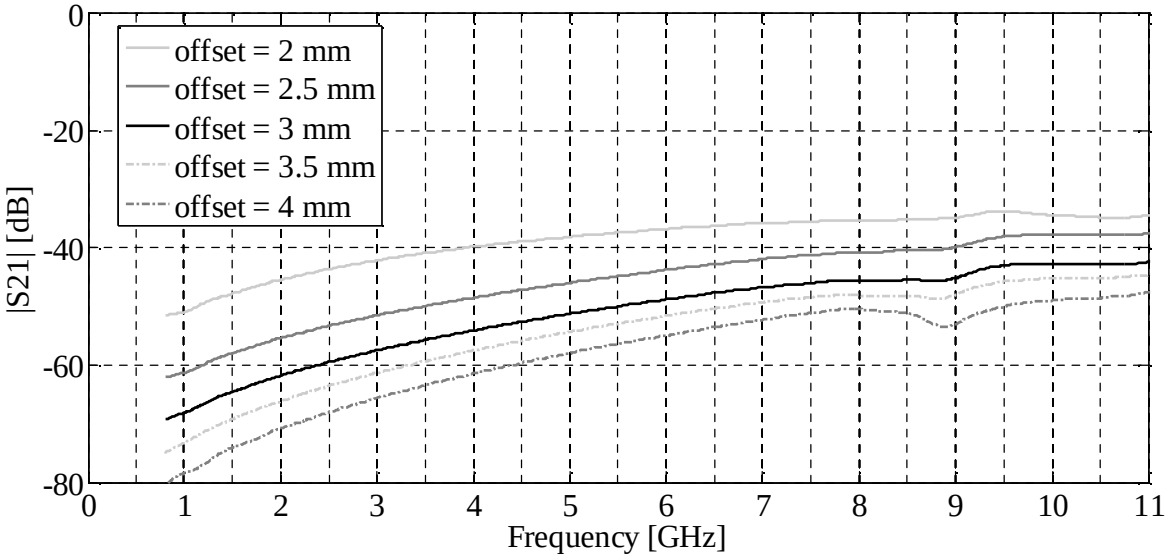


**Figure 3.19.** The coupling between the two ports of the transition section as the distance between the two input feed pins is changed.

## 3.6 Summary

In this chapter the transition section of the quad-ridged horn antenna was investigated in more detail. A couple of modifications were incorporated into three different configurations for the transition section. These configurations were a transition section with a square cavity, a transition section with a pyramidal cavity as well as a transition section with a pyramidal cavity with steps. An optimization process was applied to these configurations to achieve the widest bandwidth with the lowest VSWR, as well as to suppress the excitation of higher order modes. The excitation of the higher order modes was investigated through the transmission coefficients of the dominant and higher order modes. The field distributions of the modes were shown. It was expected there would be dips in the boresight gain of the complete antenna at the frequency points where the higher order modes received a significant amount of the input power. It was shown that adding steps into the cavity of the transition section helped to suppress the excitation of the higher order modes.

It was concluded that the configuration with a pyramidal cavity and steps inserted into the cavity delivered the best performance. This configuration was used in the final design of the quad-ridged horn antenna with pyramidal sidewalls.

A parametric study was conducted on the best configuration for the transition section to determine the effect of manufacturing tolerances on the performance of the transition

section. It was observed that the parameters for the width and height of the waveguide, the width of the ridges and the gap between the ridges had a significant effect on the performance of the transition section. In particular, the gap between the ridges was a critical parameter that had a significant effect on the performance over the entire operational bandwidth. Therefore, the tolerance of this parameter was minimized during manufacturing to minimize the difference between the simulated and measured performance.

# CHAPTER 4 THE FLARED HORN SECTION

## 4.1 Introduction

The pyramidal horn section can be thought of as a ridged waveguide where the sidewalls are slowly flared outwards towards the aperture. Consequently, the dimensions for the width and height of the waveguide as well as the width and gap between the ridges, determine the impedance of this quasi-ridged waveguide. A parametric study is performed in section 4.2 to determine whether or not better performance could be achieved with an antenna that has smaller boxed dimensions than those of [17]. At the same time the effect that the length and the size of the aperture has on the performance of the flared horn section is investigated. The length and the size of the aperture have an influence on the profile for the ridges.

In most of the published research on ridged horn antennas the flared horn section is seen as an impedance transformer. The flared horn section is designed in such a way that the wave impedance of the flared horn section changes smoothly from the characteristic impedance of 50 Ω, of the co-axial cable, to 377 Ω or 120π Ω, of free space, at the aperture. A low VSWR is therefore achieved. The profile of the ridges also influences how the dominant and higher order TE modes propagate along the axial length of the horn section. Sudden changes in the profile could cause higher order modes to be excited, which lead to unwanted spikes in the VSWR. The profile of the ridges is a very important parameter that is studied later in section 4.3 of this chapter. Four possible configurations for the flared horn section, with different profiles for the ridges, are investigated to determine for which configuration is the lowest VSWR achieved across the widest bandwidth. It is desirable for the EM fields to be confined between the ridges at the feed point, while a field distribution similar to that of a pyramidal horn is desired at the aperture [20]. This ensures that only the dominant mode is propagating.

In section 4.4 the main findings of this chapter are summarized.

## 4.2 A parametric study of the flared horn section

An exponential profile with a linear taper, similar to that of [17], is used in this parametric study. The parametric study is performed to determine whether or not better performance could be achieved with a complete antenna with smaller boxed dimensions than those of [17]. This also demonstrates the effect of changing the length and the size of the aperture on the performance of the flared horn section.

The flared horn section is investigated by placing a very short ridged waveguide (equal to *wg_l1* of the transition section) on the input side of the pyramidal horn. A waveguide port is placed on the input face of the ridged waveguide to act as the source in the simulations. The geometrical parameters of the flared horn section are shown in Figure 4.1.

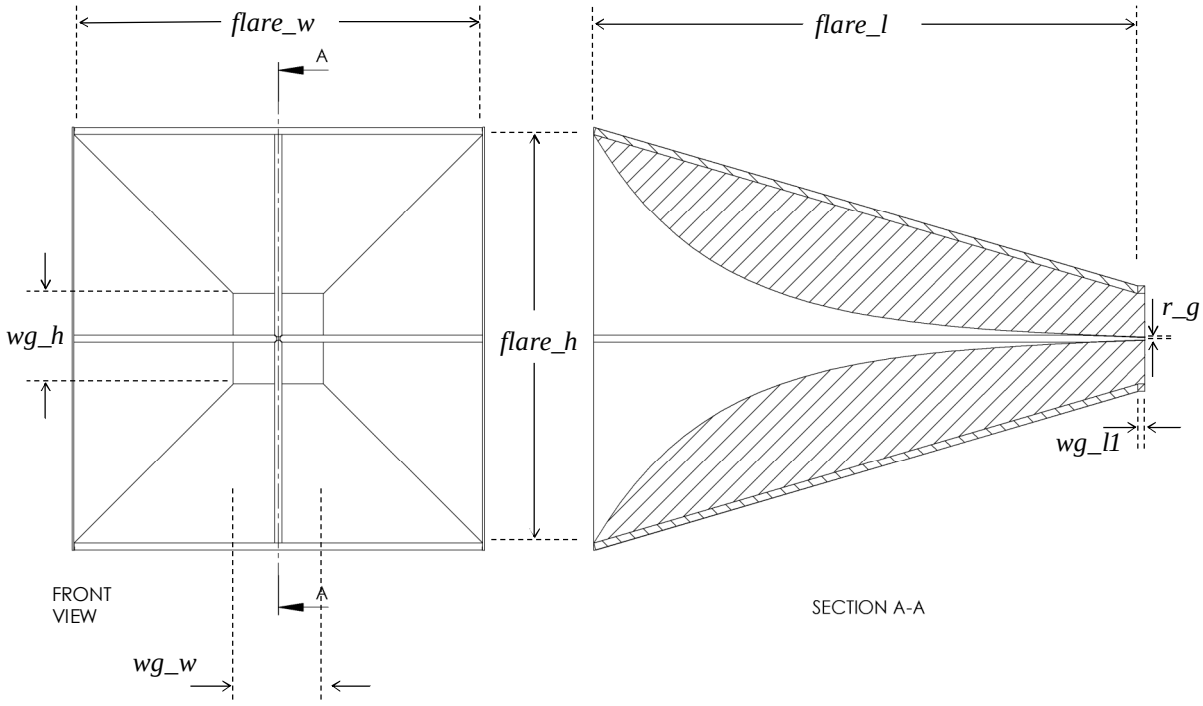


**Figure 4.1.** The parameters of the flared horn section.

A description of these parameters is given in Table 4.1. It should be noted that the values for *wg_l1*, *wg_w*, *wg_h*, *r_g* and *r_w* are the same as those of configuration III of the transition section.

**Table 4.1.** The parameters of the flared horn section.

| **Name** | **Description** |
|---|---|
| *flare_w* | Width of the flared horn section at the aperture |
| *flare_h* | Height of the flared horn section at the aperture |
| *flare_l* | Length of the flared horn section |
| *wg_l1* | Length of the first waveguide section |
| *wg_w* | Width of the waveguide |
| *wg_h* | Height of the waveguide |
| *r_g* | Gap between the ridges at the feed point |
| *r_w* | Width of the ridges |

### 4.2.1 Length of the flared section

The aim of this part of the parametric study on *flare*_l is to determine whether better performance could be achieved with an antenna that is shorter than the published design of [17]. A value of 375 mm (1λ at 0.8 GHz) is used as the benchmark length for the complete antenna, as discussed in section 2.3.1 of Chapter 2. The optimized total length of configuration III for the transition section is 26 mm (0.07λ at 0.8 GHz). In this study the values for *flare_l* are chosen in such a way that the length of the complete antenna is shorter than, equal to and longer than the benchmark of 375 mm. The crossover point, where the length of the complete antenna starts to exceed the benchmark, is when *flare_l* is made longer than 349 mm (0.93λ at 0.8 GHz). A change in the parameter *flare_l* influences the length of the flared horn section as well as the profile used to taper the ridges as shown in Figure 4.2. As *flare_l* increases, the tapering of the ridges occurs more gradually than in the case for smaller values for the parameter.

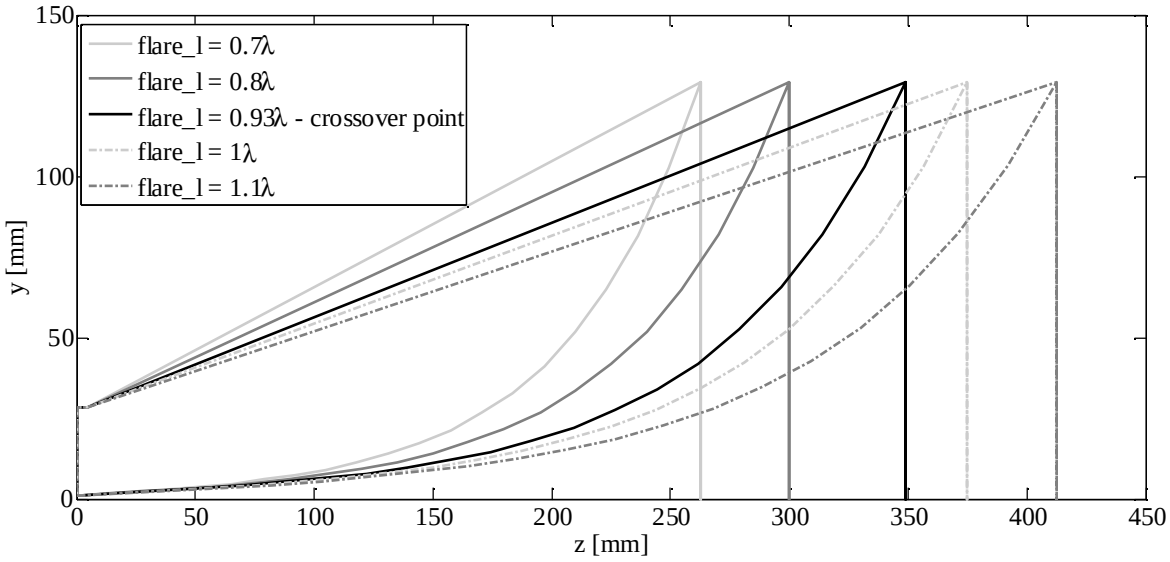


**Figure 4.2.** A section view through the flared horn section as the length is changed.

The VSWR of the flared horn section for variations in *flare_l* is shown in Figure 4.3 and Figure 4.4. It can be seen that the point where the VSWR goes below 1.5 is shifted downwards in frequency as *flare_l* is increased from 0.7λ to 0.93λ. As soon as *flare_l* is increased past 0.93λ there is no significant improvement in the VSWR performance. It can be seen that for *flare_l* > 0.93λ, the VSWR even goes slightly above 1.5 at frequencies higher than that of *flare_l* = 0.93λ. Thus, an improvement in performance cannot be achieved with a flared horn section that is shorter than 0.93λ. However, it can also be concluded that increasing the length of the flare past 0.93λ does not deliver better performance. Consequently, 0.93λ is used for the length of the flared horn section in the rest of this dissertation.

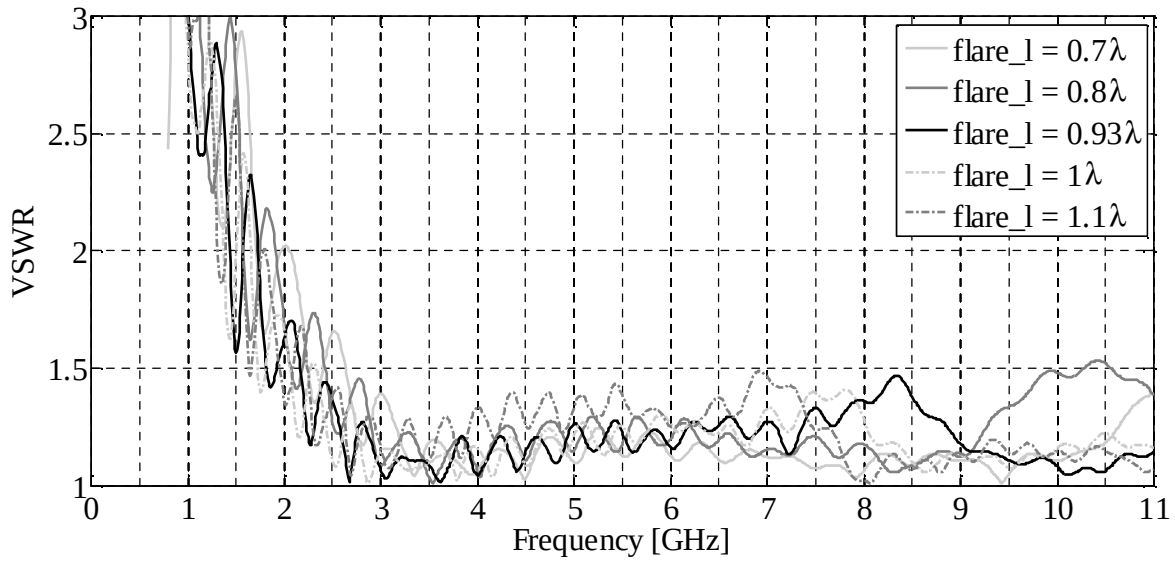


**Figure 4.3.** The VSWR as the length of the flare is changed.

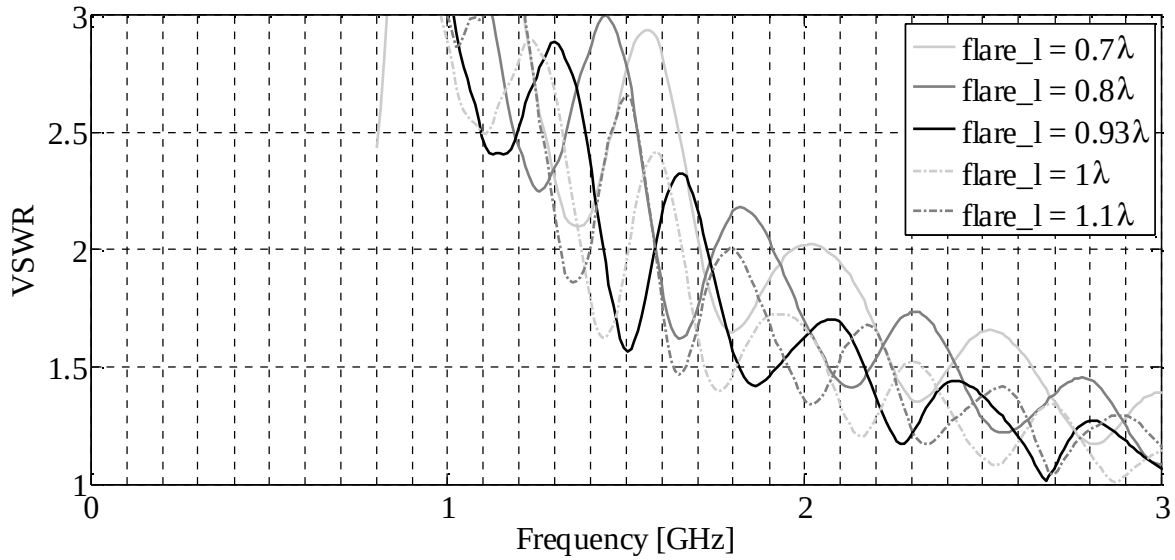


**Figure 4.4.** A close-up of the VSWR as the length of the flared horn section is changed.

### 4.2.2 Aperture of the flared section

The dimensions for the aperture of the antenna determine the cut-off frequency of the dominant mode at the aperture. It also influences the value of the boresight gain. The wider the aperture becomes the narrower the main beam becomes, thus increasing the boresight gain and vice versa. The dimensions for the aperture are described by the parameters *flare_h* and *flare_w*. In quad-ridged horn antennas the width and the height of the flared horn section at the aperture are equal, i.e. *flare_h = flare_w*.

The change in the flared horn section as the dimensions for the aperture are changed is shown in Figure 4.5. A change in the dimensions of the aperture also brings about a change in the profile of the ridges, as is the case when the length of the flared horn section is changed. It can be seen from Figure 4.5 that the rate of opening for the profiles is more or less the same near the feed point for all values of *flare_h*. The flared horn sections with larger apertures have a faster rate of opening near the aperture than the ones with smaller apertures, as shown in Figure 4.5. The benchmark size for the aperture is 0.69λ by 0.69λ at 0.8 GHz. The aim of this part of the parametric study is to determine whether better performance can be achieved with a flared horn section that has an aperture smaller than that of the published design of [17]. In two of the cases the aperture is made bigger than the benchmark size for the aperture, as shown in Figure 4.5.

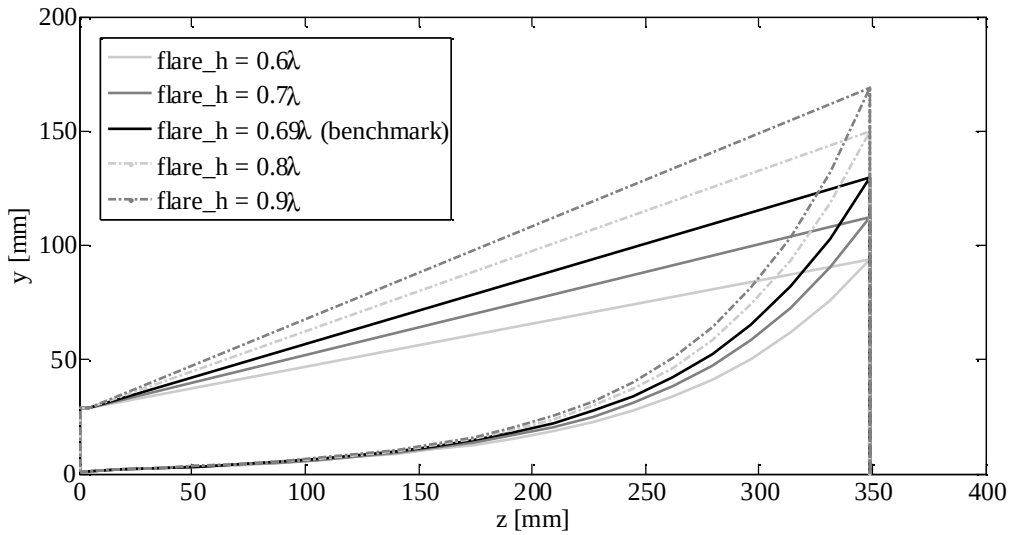


**Figure 4.5.** A section view through the flared horn section as the dimensions for the aperture are changed.

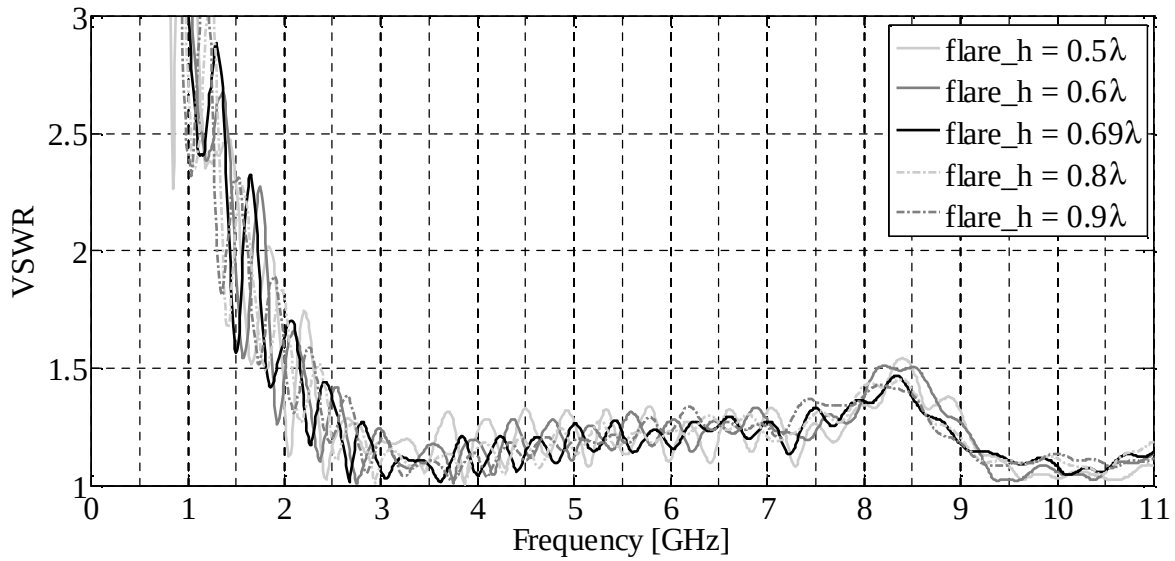


**Figure 4.6.** The VSWR as the dimensions for the aperture are changed.

The VSWR as the dimensions for *flare_h* and *flare_w* are changed are shown in Figure 4.6 and Figure 4.7. As can be seen from Figure 4.6, a change in the dimensions of the aperture does not bring about a significant change in the VSWR at frequencies higher than 3 GHz. A close up of the VSWR between 0.8 and 3 GHz is shown in Figure 4.7. It can be seen from this figure that as the size for the aperture is increased the frequency point where the VSWR goes below 1.5 decreases. This continues up to approximately *flare_h* = 0.8λ, for which the VSWR goes below 1.5 at approximately 2.15 GHz. As the parameter is increased past 0.8λ, the VSWR goes below 1.5 at frequencies higher than 2.15 GHz. It is concluded that better performance cannot be achieved with a design that has a smaller aperture than that of the benchmark. The specification of the new design is that it should not exceed the size of the published benchmark design. Therefore, the benchmark size of 0.69λ by 0.69 λ is used for the aperture for the flared horn section in the rest of this dissertation.

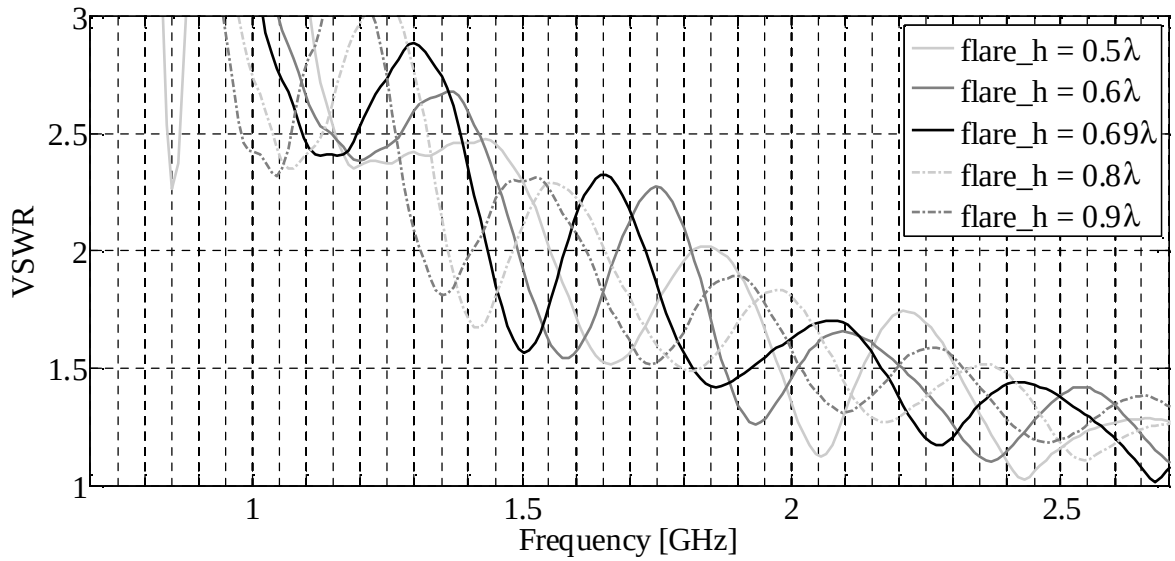


**Figure 4.7.** A close up of the change in the VSWR as the dimensions for the aperture are changed.

## 4.3 The different configurations

It is concluded from the background presented in Chapter 2 that a change in the profile for the ridges can help to improve the performance of the flared horn section. In this research four profiles for the ridges are investigated, to determine which profile delivers a VSWR of less than 1.5 across the widest bandwidth. Fixed dimensions are used for the axial length and the aperture of the antenna. It is discussed in the previous section that the best performance is delivered by a flared horn section that has dimensions of

$$flare\_h = flare\_w = 258.75 \text{ mm and}$$
$$flare\_l = 349 \text{ mm},$$

as configuration III is chosen as the best transition section to use in the final design of the complete antenna.

The four profiles that are investigated are an exponential profile with a linear taper similar to [17], an elliptical profile similar to [32] and [47], a cubic Bézier profile based on the design of [48], as well as an exponential profile that ends in a circular segment near the aperture of the antenna similar to [36] and [49]. The four configurations for the different ridge profiles are shown in Figure 4.8. The aim is to keep the length and the aperture of the complete antenna the same for all the configurations. Consequently, for some of the

profiles shorter pyramidal horn sections are used, as the ridges extend past the aperture of the horn. In all four profiles a limited number of points are used to generate the curves of the profiles. Therefore, the actual modelled and manufactured ridges are linear approximations of the precise mathematical equations that describe the profiles in the sections below.

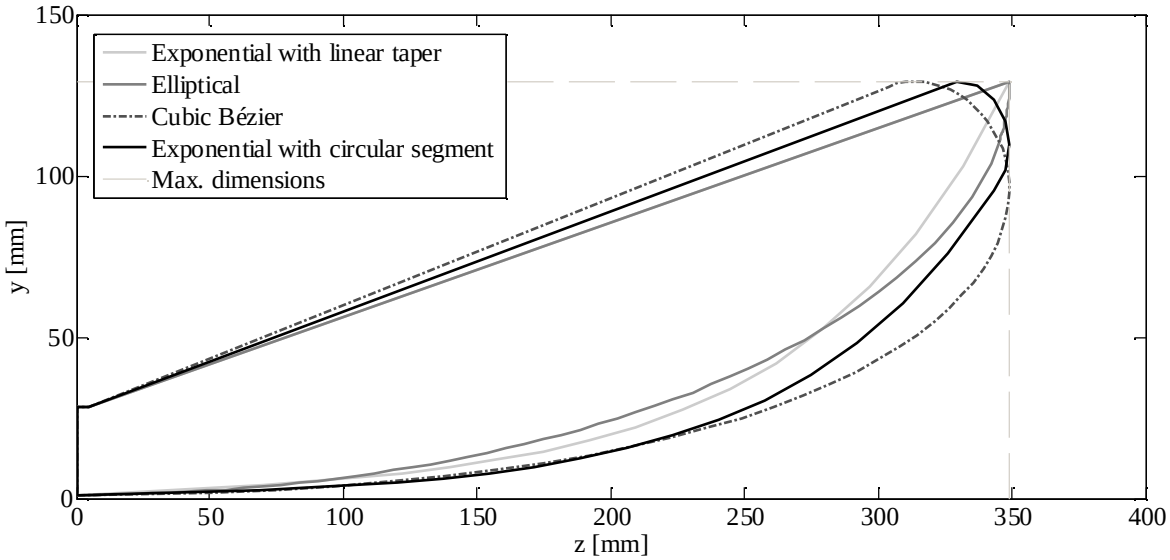


**Figure 4.8.** A comparison of the configurations of the flared horn section with different profiles for the ridges.

### 4.3.1 The exponential profile with a linear taper

The exponential profile with a linear taper is given by

$$y(z) = ae^{bz} + cz, \tag{4.1}$$

where $c$ is a constant equal to 0.02, which improves the return loss performance [12], [17]. The value of $a$ is equal to half the dimension of the gap between the ridges at the feed point. In this case the optimum value of 2 mm is used for the gap. The value of $b$ is given by

$$b = \frac{\ln\left[\frac{y_{end} - cz_{end}}{a}\right]}{z_{end}}, \tag{4.2}$$

where $z_{end}$ is the length of the flared horn section. $y_{end}$ is equal to half the dimension of the aperture. In this case, where the lowest frequency of operation is 0.8 GHz, these dimensions are

$$z_{end} = flare\_l = 349 \text{ mm and}$$
$$y_{end} = \frac{1}{2}(flare\_h) = 129.375 \text{ mm.}$$

The exponential profile with the linear taper is shown in Figure 4.9. It can be seen from this figure that as the ridges end at the aperture of the antenna, $z_{end}$ and $y_{end}$ (the maximum dimensions) can be used for the dimensions for the axial length and aperture of the pyramidal horn.

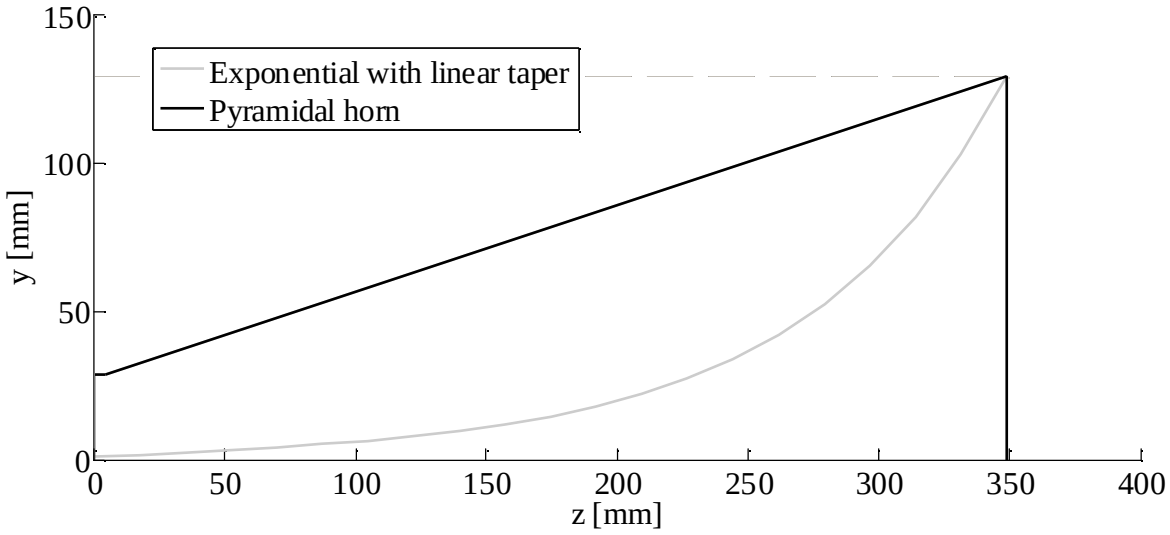


**Figure 4.9.** A section view of the flared horn section with the exponential with linear taper profile for the ridges.

### 4.3.2 The elliptical profile

A quarter of an ellipse is used to achieve the elliptical profile for the ridges. The profile is given by

$$y = \sqrt{\left(1 - \frac{z^2}{z_{end}^2}\right)(y_{end} - a)^2} + y_{end}, \tag{4.3}$$

where $a$, $y_{end}$ and $z_{end}$ has the same value as in the case of the exponential profile with a linear taper for the ridges. Similarly, it can be seen in Figure 4.10 that the ridges end at the aperture of the antenna. Thus, the maximum dimensions are used for the axial length and aperture of the pyramidal horn.

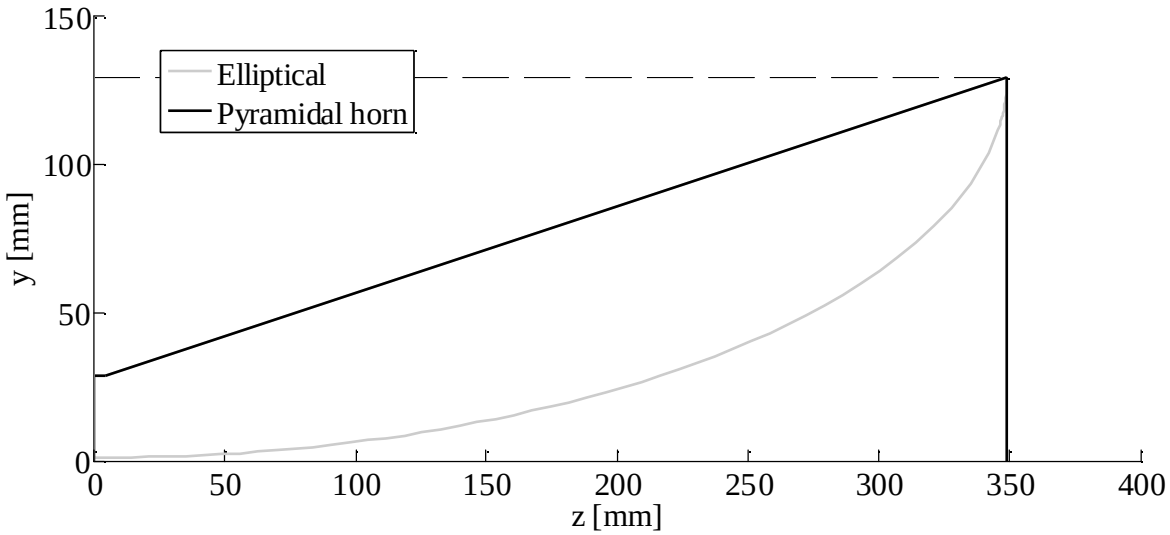


**Figure 4.10.** A section view of the flared horn section with the elliptical profile for the ridges.

### 4.3.3 The cubic Bézier profile

The cubic Bézier profile for the ridges is based on a design for a double-ridged horn antenna [48]. This profile has been used in a quad-ridged horn antenna by the same author [14], [33]. The co-ordinates of points along the profile are published in [48]. A cubic Bézier curve is used to approximate this profile. The profile is scaled in such a way that the ridges used do not exceed the maximum dimensions as shown in Figure 4.8.

The equations for the *y* and *z* coordinates for the cubic Bézier profile are

$$z = z_{P_0}(1-t)^3 + 3z_{P_1}(1-t)^2 t + 3z_{P_2}(1-t)t^2 + z_{P_3}t^3, t \in [0,1] \text{ and} \tag{4.4}$$

$$y = y_{P_0}(1-t)^3 + 3y_{P_1}(1-t)^2 t + 3y_{P_2}(1-t)t^2 + y_{P_3}t^3, t \in [0,1]. \tag{4.5}$$

In equations (4.4) and (4.5) $z_{P_0}$ to $z_{P_3}$ and $y_{P_0}$ to $y_{P_3}$ are the control points used to generate the profiles. The values for the control points in this case are

$$(z_{P_0}, y_{P_0}) = (0, a) = (0,1),$$
$$(z_{P_1}, y_{P_1}) = (443.9, a) = (443.9,1),$$
$$(z_{P_2}, y_{P_2}) = (358.9, 145.7) \text{ and}$$
$$(z_{P_3}, y_{P_3}) = (303.6, 127.7).$$

It is clear when looking at Figure 4.11 that the ridges extend past the aperture of the pyramidal horn section. Consequently, a shorter axial length is used for the pyramidal horn so that the ridges do not extend past $z_{end}$. In this case the axial length of the pyramidal horn is 303.6 mm. It can also be seen that a slightly smaller aperture with a value of 2*127.7 = 255.4 mm is used. This is due to the profile of the ridges that curls backwards near the end.

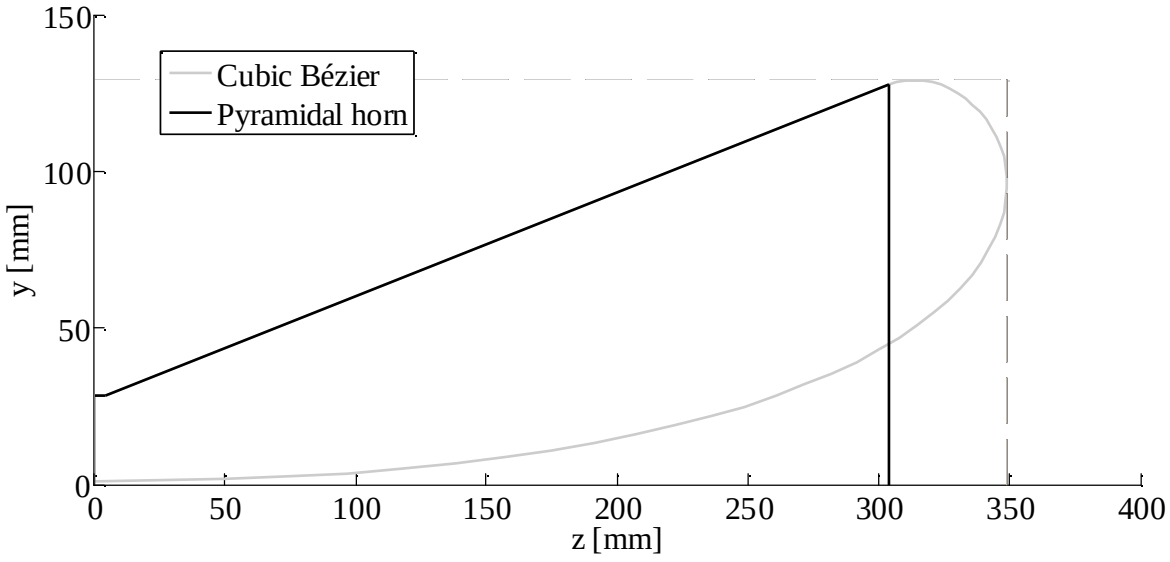


**Figure 4.11.** A section view of the flared horn section with the cubic Bézier profile for the ridges.

### 4.3.4 The exponential profile with a circular segment

In [36] and [49] a circular segment is added to an exponential profile for the ridges of a quad- and double-ridged horn antenna, respectively. The circular segment helps to achieve aperture matching, i.e. to reduce diffraction at the aperture of the antenna. This helps to reduce the reflections from the points where the ridges connect to the sidewalls at the aperture and consequently the amount of backward radiation [50]. A similar profile is used in this section. An exponential profile of the form

$$y = me^{nz} \tag{4.6}$$

is used. The value of $m$ is equal to 1 mm – half the dimension of the gap between the ridges. The value of $n$ is determined from

$$n = \frac{\ln\left[\frac{y_{circle}}{m}\right]}{z_{circle}}, \tag{4.7}$$

where $(z_{circle}, y_{circle})$ are the co-ordinates of the starting point of the circular segment. The co-ordinates for the starting point are

$$(z_{circle}, y_{circle}) = (343.2,\ 95.2).$$

Three eights of a full circle is used for the circular segment. The circle has a radius of $r$ = 20 mm or r = 0.05λ at 0.8 GHz. The co-ordinates for the centre point of the circles are

$$(z_{center}, y_{center}) = (z_{end} - r, y_{end} - r) = (329, 109.4).$$

If the centre point of the circle is used as the origin of the co-ordinate system for the circle, the circle is traced from -45° to 90°. This ensures a smooth transition from the exponential profile to the circular segment. The ridges extend past the aperture of the antenna as shown in Figure 4.12. Therefore, as in the case of the cubic Bézier profile for the ridges, the axial length of the pyramidal horn is made shorter than $z_{end}$ (the maximum dimension). The axial

length for the pyramidal horn in this case is 329 mm. The dimensions for the aperture are $2 * y_{end} = 258.8$ mm.

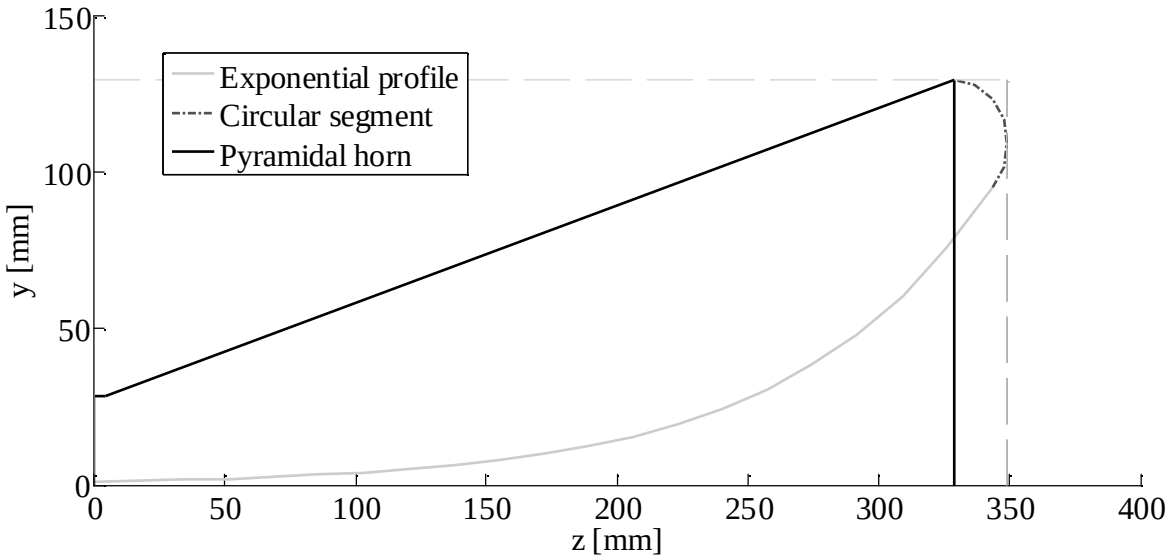


**Figure 4.12.** A section view of the flared horn section with the exponential profile with a circular segment for the ridges.

### 4.3.5 Simulation results

The VSWR performance for the pyramidal horn sections with the different profiles for the ridges is shown in Figure 4.13. It can be seen from this comparison that the configuration with the exponential profile with circular segment for the ridges goes below 1.5 at the lowest frequency of 1.5 GHz. The VSWR remains below 1.5 across the rest of the operational bandwidth. The VSWR for the other configurations only goes below 1.5 at 2 GHz and higher frequencies. Therefore, the configuration with the exponential profile for the ridges with a circular segment is deemed to deliver the lowest VSWR across the widest bandwidth and is consequently used in the final design of the complete antenna.

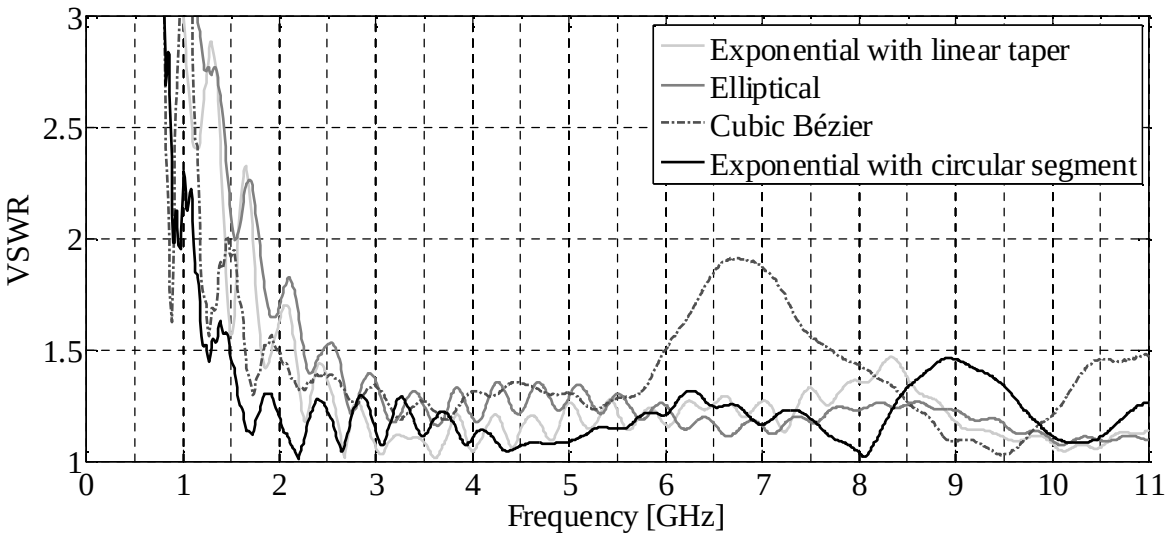


**Figure 4.13.** The comparison of the VSWR of the flared horn sections with the four different profiles.

## 4.4 Summary

In this chapter the flared horn section was investigated. A parametric study was performed to determine whether a smaller antenna than the published design of [17] could be obtained. The boxed dimensions for the complete antenna of [17] were used as a benchmark. It was found that if the dimensions of the flared horn section were decreased, so that the complete antenna was smaller than the benchmark, the performance was not improved. The performance was also not improved by increasing the dimensions for the flared horn section so that the complete antenna was larger than the benchmark. Thus, the optimum length of the flared horn section was 0.93λ and the optimum size for the aperture was 0.69λ by 0.69λ, which gives a complete antenna that had the same boxed dimensions as those of [17].

One modification to improve the performance of the antenna with pyramidal sidewalls was identified to be a change in the profile used in the flared horn section of the antenna. Four profiles were investigated to determine which one delivered the best VSWR performance across the widest bandwidth. The mathematical expressions for the profiles and the differences between the profiles were shown. It was concluded from the simulation results that the best performance was achieved when an exponential profile with a circular segment was used to taper the ridges. This profile was used in the final design of the complete antenna that was manufactured.

# CHAPTER 5 THE COMPLETE ANTENNA

## 5.1 Introduction

The final design of the complete antenna is a combination of the best transition section and the best flared horn section. It has already been discussed that the transition section with a pyramidal cavity with steps and the flared horn section with an exponential profile with a circular segment for the ridges, delivers the best performance. In this chapter they are combined and the complete antenna is simulated. This final design for the complete antenna is compared to other designs, with transition and flared horn sections that do not deliver the best performance, in section 5.2 and 5.3. The comparison is done in terms of the VSWR and boresight gain.

In section 5.4 the VSWR performance of the two separate sections and the complete antenna is compared. The computational requirements needed to simulate the sections and the complete antenna are also given. This will give an idea of how much resources, in terms of memory and time, can be saved by simulating the sections of the antenna separately.

A comparison between the simulation results achieved with FEKO and CST Microwave Studio is given in section 5.5. This is done to validate the simulation results achieved with CST Microwave Studio, since the two software packages use different numerical methods to calculate the EM properties of the modelled structure.

The mechanical design of the final antenna is discussed in section 5.6. Thereafter the measured and simulated results are compared in section 5.7. The antenna is evaluated in terms of the VSWR, the coupling between the ports, the boresight gain and the radiation patterns. Differences between the measured and simulated results are discussed. Lastly, the chapter is summarized in section 5.8 and the main findings are presented.

## 5.2 The simulated performance of the complete antenna with two different transition sections

The complete antenna is shown in Figure 5.1 with two different transition sections. In the first case, configuration I is used for the transition section where a square cavity is used without any steps that connect the ridges to the backshort. In the second case, configuration III is used for the transition section with a pyramidal cavity and steps that connect the ridges to the backshort. It should be noted that only the performance of port 1 of both models are compared to each other. It is shown later in this chapter that the performance of port 2 is very similar to that of port 1.

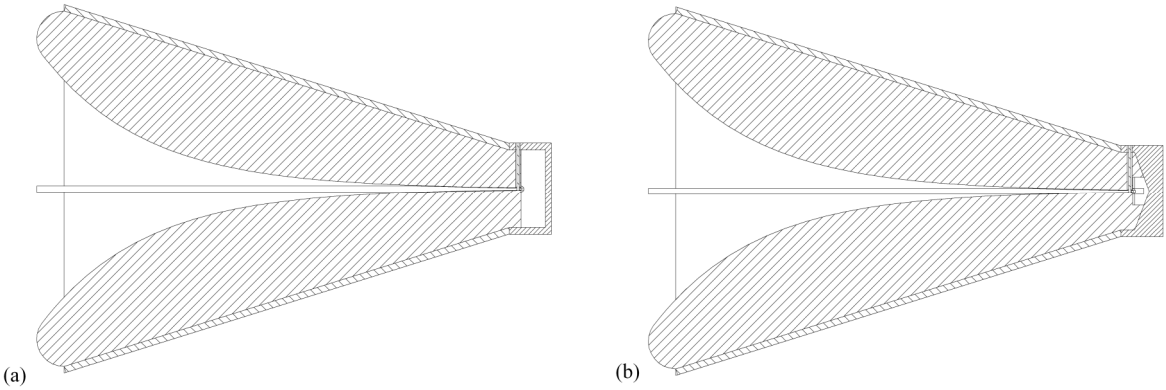


**Figure 5.1.** The complete antenna with (a) transition I and (b) transition III. The flare with an exponential profile with a circular segment is used in both simulations.

It is shown in section 3.4.2 of chapter 3 that a number of higher order modes are excited in configuration I for the transition section. These higher order modes receive a significant amount of the input power at approximately 5.6 GHz, which coincides with some of the cut-off frequencies of the higher order modes. This indicates that the higher order modes start to propagate at approximately 5.6 GHz. The comparison for the VSWR of the complete antenna with the two different transition sections is shown in Figure 5.2. It can be seen that the antenna that has configuration I for the transition section has a larger spike at 5.6 GHz than the antenna with configuration III for the transition section. This spike in the VSWR coincides with the point where the higher order modes start to propagate in configuration I for the transition section. The VSWR is also above 2 at 0.8 GHz and rises steeply above 2 at approximately 10.8 GHz for the antenna with configuration I for the transition section. The VSWR is below 2 from 0.8 GHz to 11 GHz for the antenna with

configuration III for the transition section. The VSWR for the complete antenna corresponds well with the reflection coefficients |S11| of the different transition sections, as shown in section 3.4.1 of chapter 3. Therefore, the bandwidth where the VSWR of the complete antenna is below 2 is limited by the performance of the transition section.

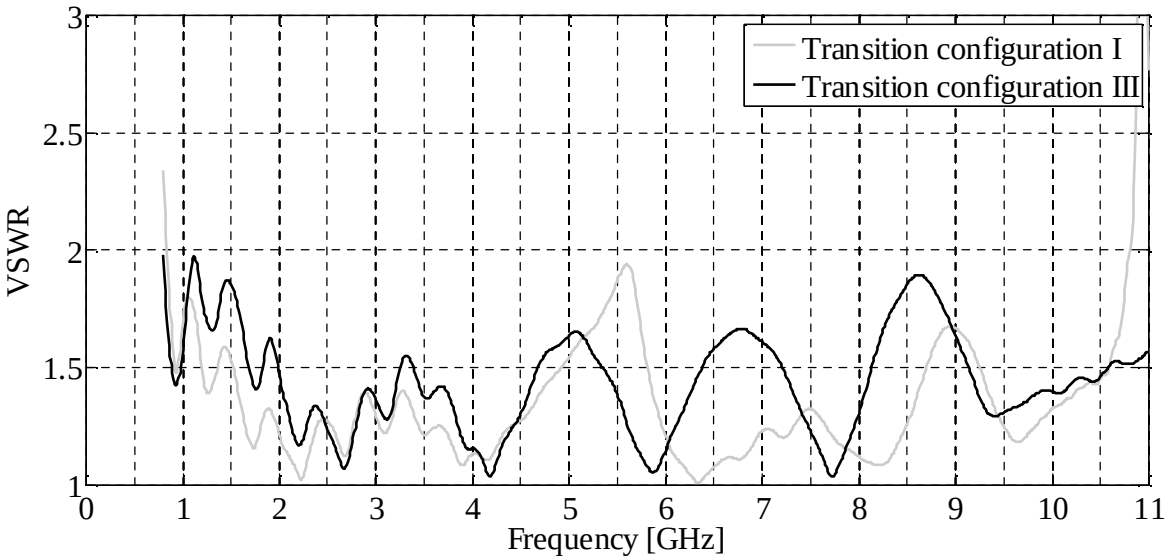


**Figure 5.2.** The VSWR of the complete antenna with an exponential profile with a circular segment for the ridges with different transition sections.

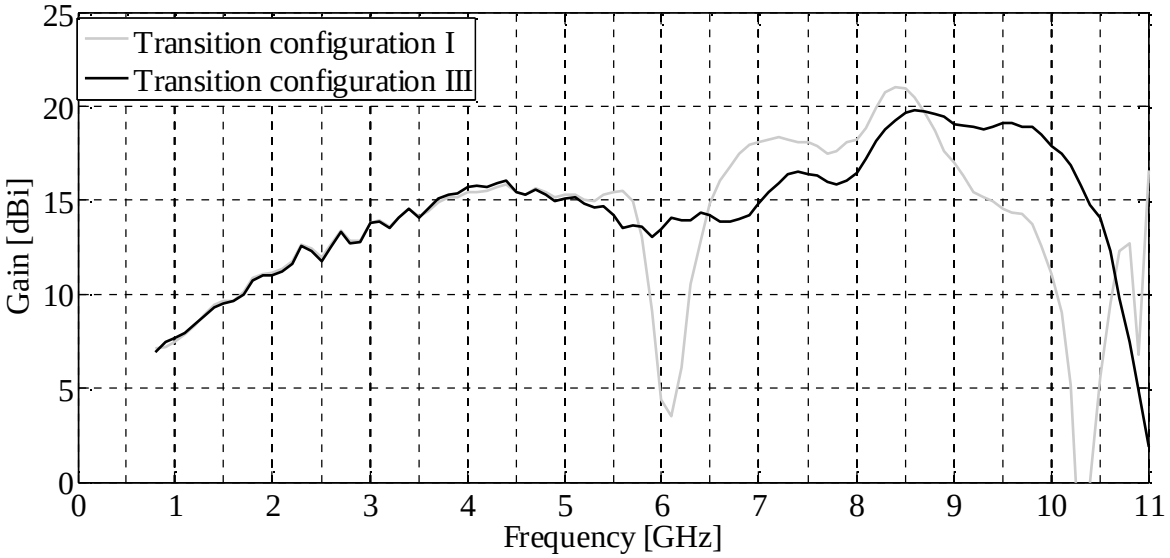


**Figure 5.3.** The boresight gain of the complete antenna with an exponential profile a circular segment for the ridges with different transition sections.

It is also shown in section 3.4.2 of chapter 3 that for configuration III the higher order modes only start to receive a significant amount of the input power for frequencies above 9

GHz, which is higher than the cut-off frequencies of the first two higher order modes. The boresight gain performance of the complete antenna with the two different transition sections is shown in Figure 5.3. It can be seen from this figure that in the case where configuration I is used for the transition section there are large dips in the gain between 5.7 and 6.5 GHz and for frequencies above 9 GHz. The dip in gain between 5.7 and 6.5 GHz corresponds well with the frequency point (5.6 GHz) where it is concluded that the higher order modes start to propagate in configuration I of the transition section. The large dip in the gain between 5.7 and 6.5 GHz is not present in the case where configuration III is used for the transition section. It is shown in section 3.4.2 of chapter 3 that the higher order modes only start to receive a significant amount of input power above 9 GHz for configuration III. This corresponds well to the drop in the boresight gain which slowly starts at 9 GHz in the case of the complete antenna with configuration III for the transition section. Thus, it is concluded that the dips in the boresight gain of the complete antenna occur at the points where the higher order modes start to propagate in the transition section. The higher order modes cause a break-up in the main beam of the radiation patterns with consequent dips in the boresight gain of the antenna. The VSWR performance of the transition section determines the VSWR of the complete antenna at high frequencies. It is clear from the results shown in this section that predictions for the performance of the complete antenna can be made by looking at the performance of the transition section.

## 5.3 The simulated performance of the complete antenna with two different flared horn sections

In this section the complete antenna is modelled with a flared horn section that has an elliptical profile for the ridges in the one case and an exponential profile with a circular segment for the ridges in the other case, as shown in Figure 5.4. In both of these cases the transition section with the best performance, i.e. configuration III, is used.

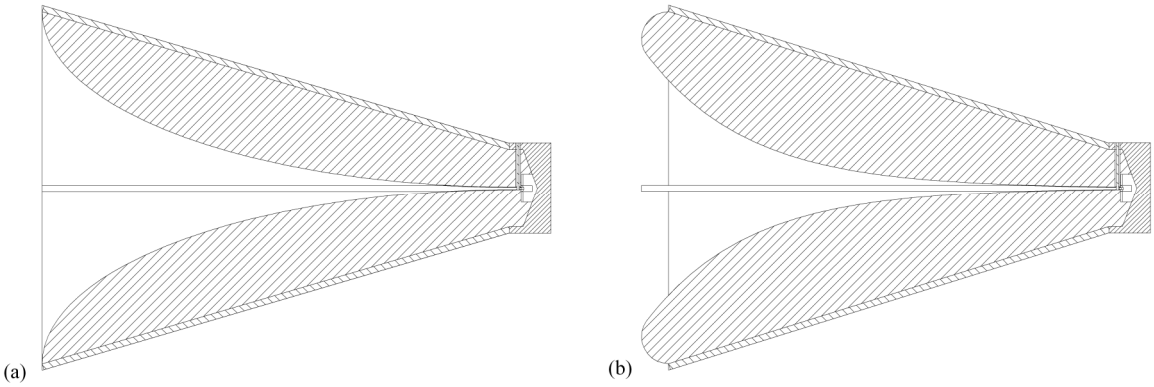


**Figure 5.4.** The complete antenna with flared horn sections with (a) an elliptical profile and (b) an exponential profile with a circular segment for the ridges.

The VSWR of the two antennas is shown in Figure 5.5. It is clear that in the case where the elliptical profile is used in the flared horn section, the VSWR of the complete antenna only goes below 2 at frequencies higher than 2 GHz. This is in comparison to the case where the exponential profile with circular segment is used to taper the ridges, where it can be seen that the VSWR is below 2 across the entire 0.8 to 11 GHz bandwidth.

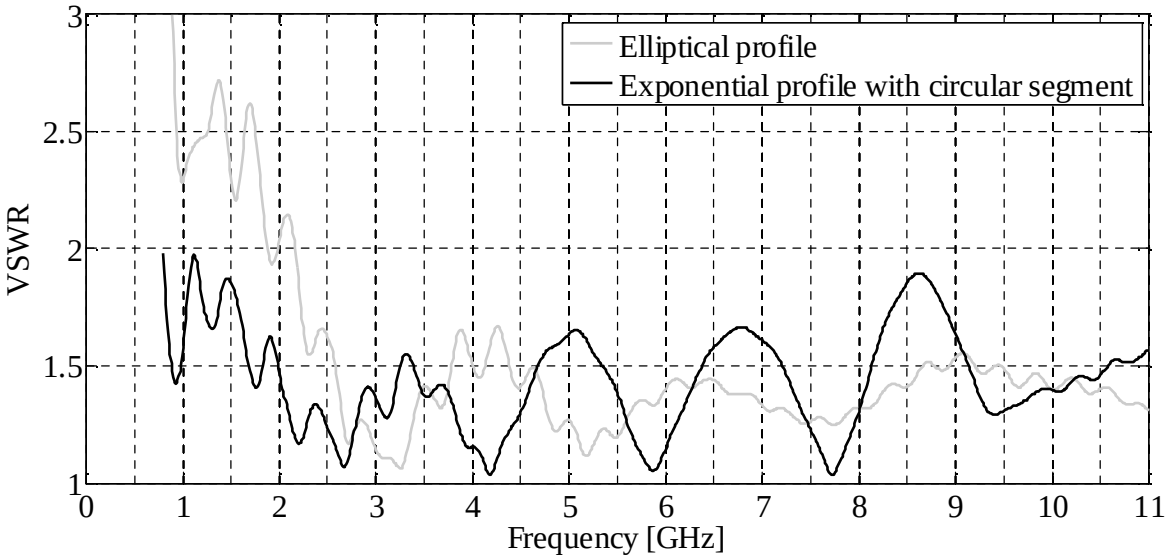


**Figure 5.5.** The VSWR for the complete antenna with the best configuration for the transition section with different flared horn sections.

It is shown in section 4.3.5 of chapter 4 that the VSWR goes below 1.5 at 2.25 GHz in the case where the elliptical profile is used and at 1.5 GHz in the case where an exponential profile with a circular segment is used in the flared horn section. The value of the VSWR is

also larger at frequencies below 2 GHz in the case where the elliptical profile is used. This corresponds well with the results achieved when the complete antenna is simulated. Thus, it is concluded that the VSWR performance of the flared horn section influences the VSWR performance of the complete antenna. This is especially true at the lower frequency portion of the bandwidth, where it is shown that the VSWR of the complete antenna has a high value in the same region where the VSWR of the flared horn section has a high value.

The boresight gain of the two antennas is shown in Figure 5.6. It can be seen that the largest difference in the gain is about 2 dBi between the two antennas. The drop in the boresight gain starts at 9 GHz for the antenna with an exponential profile with a circular segment. In the case when an elliptical profile for the ridges is used, the drop in the boresight gain only starts at 10 GHz. However, in both cases there is a rapid decrease in the gain from 10 GHz onwards.

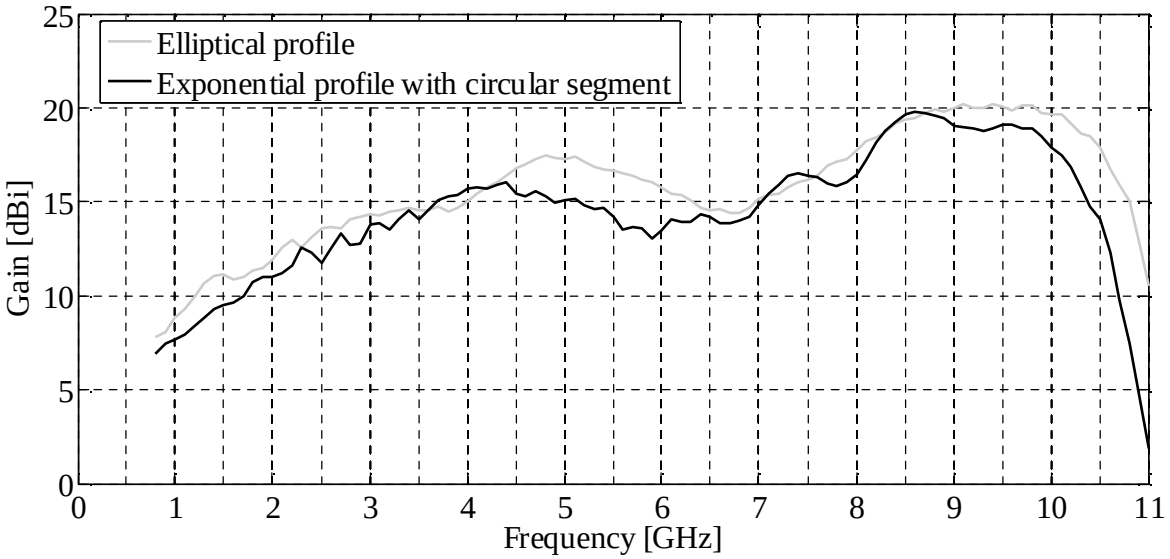


**Figure 5.6.** The boresight gain for the complete antenna with configuration III for the transition section with different flared horn sections.

It is shown in section 3.4.2 of chapter 3 that the higher order modes start to receive a significant amount of the input power at 9 GHz for configuration III of the transition section. Thus, the frequency point where the drop in the boresight gain of the complete antenna starts, corresponds well with the point where the higher order modes start to propagate. It is therefore concluded that the excitation of the higher order modes inside the transition section has a significant effect on the boresight gain of the complete antenna. It

is also concluded that changing the profile for the ridges inside the flared horn section does not have a significant effect on the boresight gain.

## 5.4 A comparison of the simulated performance of the different sections of the antenna

The simulated performance for the two sections and the complete antenna is shown in Figure 5.7. It can be seen from this figure that the VSWR performance of the complete antenna is determined by the performance of the two sections. In the lower frequency portion (1-4 GHz) of the bandwidth, the performance of the complete antenna is dominated by the performance of the flared horn section. On the other hand, the performance of the transition section determines the performance of the complete antenna in the higher frequency portion (9 GHz and upwards) of the bandwidth. In the band between 4-9 GHz the performance of the complete antenna is deemed to be a combination of the performance of the two sections.

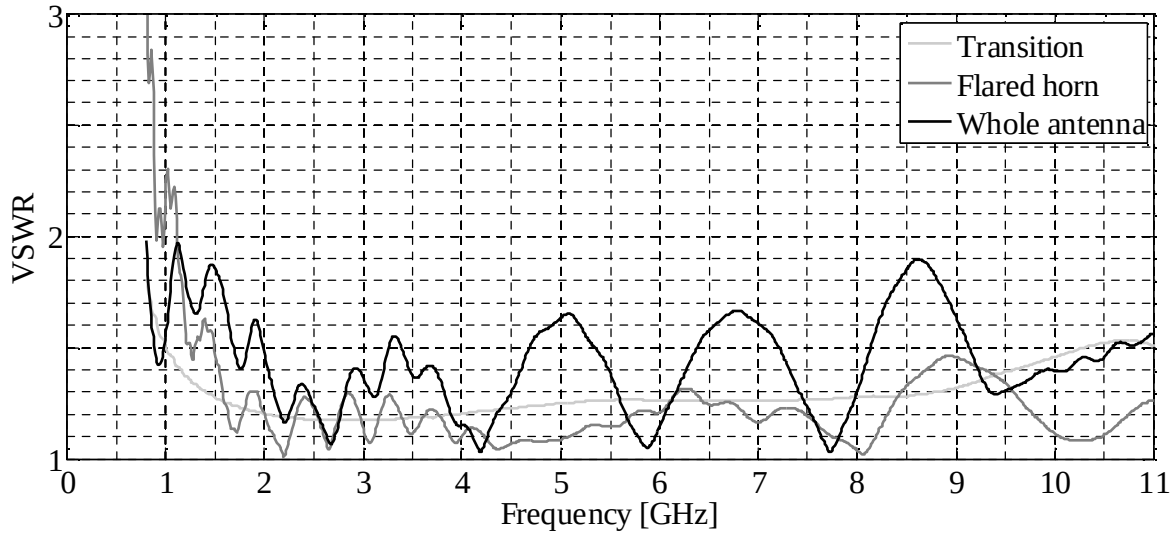


**Figure 5.7.** The VSWR of the different sections of the antenna as well the complete antenna.

The computational requirements needed to simulate the transition and flared horn sections as well as the complete antenna are shown in Table 5.1. The requirements to simulate the transition section are very small. Thus, if an improvement in the performance of the complete antenna is required through changing the parameters of the transition section, a lot of time and memory resources can be saved by only simulating the transition section.

Similarly, time and memory resources can be saved if the flared horn section is simulated alone, although the amount of resources that are saved are less than in the case of the transition section.

**Table 5.1.** Computational requirements.

| Structure | Peak physical memory | Simulation time |
|---|---|---|
| Co-axial to ridged waveguide transition | 0.08 GB | 0 h, 1 m, 40 s |
| Flared horn | 3.83 GB | 2 h, 11 m, 38 s |
| Complete antenna | 4.24 GB | 3 h, 21 m, 54 s |

## 5.5 FEKO versus CST Microwave Studio simulations

The final design of the antenna, with configuration III for the transition section and an exponential profile with a circular segment for the ridges in the flared horn section, is simulated with CST Microwave Studio (CST MWS) as well as with FEKO. In CST MWS the FIT of the time domain solver is used, while in FEKO the MoM of the frequency domain solver is used. In this section only port 1 is included in the comparison between the results achieved with the two software packages. Since there is only a small offset between the orthogonal ports of the antenna, a very similar performance can be expected with port 2.

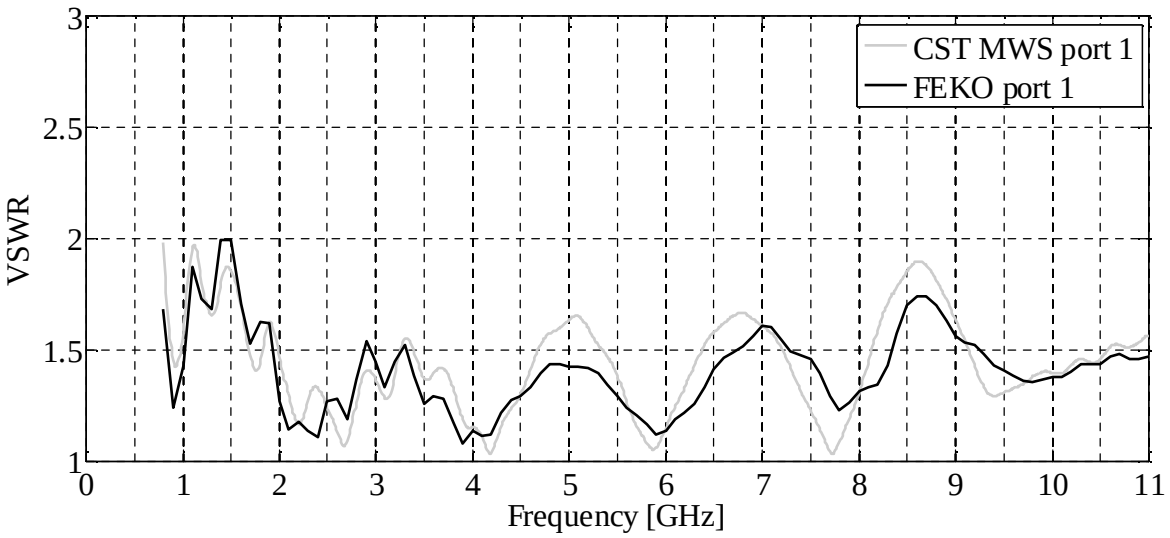


**Figure 5.8.** A comparison of the VSWR performance of the complete antenna using CST MWS and FEKO.

A comparison of the VSWR of the antenna when CST MWS and FEKO are used is shown in Figure 5.8. It can be seen that there is a good agreement between the results achieved in CST MWS and FEKO. A relative coarser mesh is used in the FEKO model compared to that of the CST MWS model. This is done to reduce the amount of memory as well as the simulation time needed for the FEKO model.

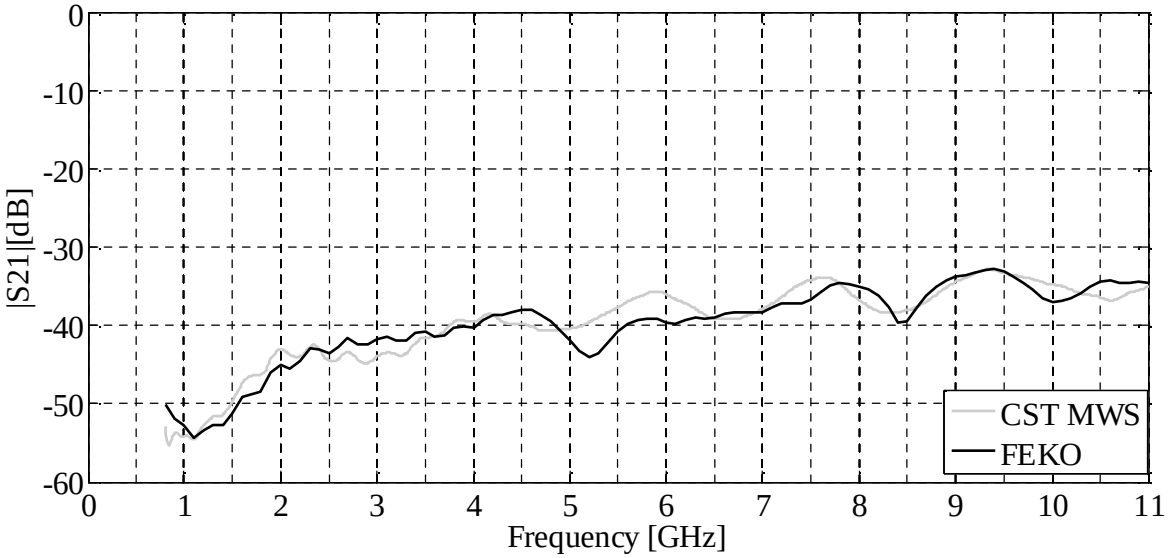


**Figure 5.9.** A comparison of the coupling between the two input ports using CST MWS and FEKO.

A comparison of the coupling between the two orthogonal ports of each model is shown in Figure 5.9. There is a good agreement between the results achieved with the two software packages.

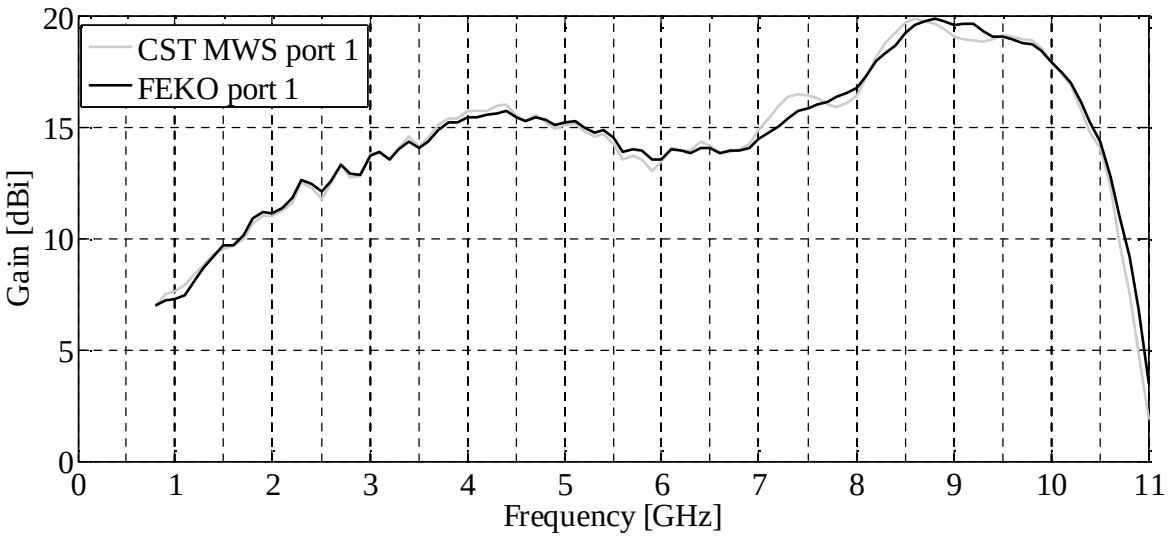


**Figure 5.10.** A comparison of the boresight gain performance using CST MWS and FEKO.

A comparison of the boresight gain performance is shown in Figure 5.10. It can be observed that there is excellent agreement between the results achieved with FEKO and CST Microwave Studio.

The good agreement between the results achieved with the two software package verifies the results achieved with CST Microwave Studio. Therefore, it is concluded that if there are differences between the measured and simulated performance that these differences can be due to manufacturing tolerances in the manufactured antenna.

## 5.6 Mechanical implementation of manufactured antenna

In the simulations with CST Microwave Studio ideal conditions exist, where pieces of metal that have zero thickness can be implemented in the modelled antenna. However, such pieces of metal can only exist in the simulations where a mathematical representation of the modelled structure is created. A variation of the antenna that can be actually manufactured is designed in SolidWorks. The manufactured antenna consists of the waveguide transition, the ridges, the feed pins and the sidewalls. Stainless steel screws are used to attach the different parts of the antenna to each other. A description of how each of the parts is made follows in the sections below.

### 5.6.1 The waveguide transition

The machine drawing of the manufactured waveguide transition is shown in Figure 5.11. It is machined from a solid aluminium cube on a 3-axis computer numerically controlled (CNC) mill. Two off-the-shelf Huber and Suhner SMA connectors [46] are used for the prototype. The co-axial cables that go to the transmitter or receiver unit are attached to these connectors. The manufactured feed pins and the holes that are cut through two of the ridges as well as the sides of the transition section form the air-filled co-axial cables of the transition section. The feed pins are the inner conductors while the sides of the holes are the outer conductors of the co-axial cables. The feed pins are connected to the Huber and Suhner SMA connectors. This is described in further detail in section 5.6.3. It can be observed from Figure 5.11 that recessed squares are cut into the sides of the transition at the places where the Huber and Suhner SMA connectors are attached to the transition. Through-holes are also cut into the sides and the backplate of the waveguide transition. These holes are used to fasten the ridges to the transition with screws. Countersink screws are used. The ridges fit into the slots cut into the transition as shown in Figure 5.12. All of the recessed corners in the transition section shown in Figure 5.11 are perfectly square with precise angles. However, it is impossible to cut absolute square corners on a CNC mill, as the mill uses a round bit to cut away the metal. Therefore, in the actual manufactured transition these corners have small radii.

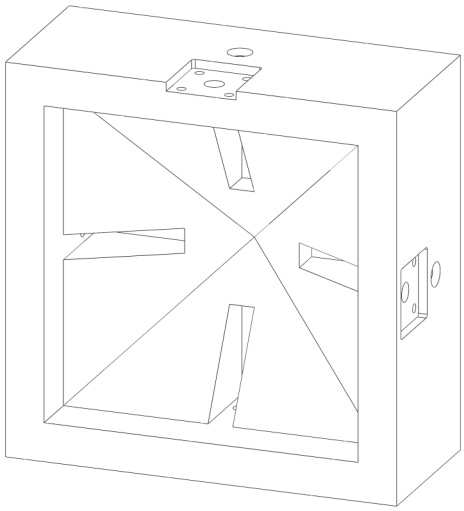

**Figure 5.11.** A dimetric view of the manufactured waveguide transition.

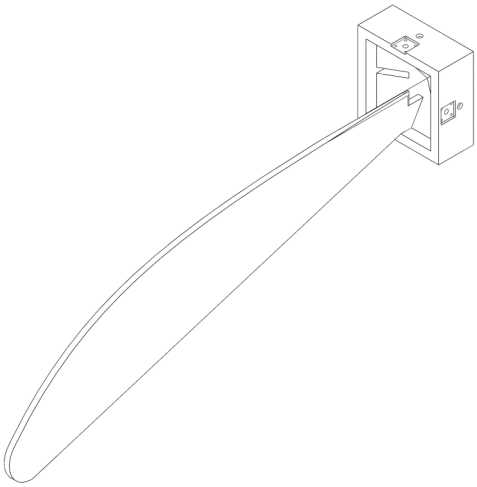

**Figure 5.12.** The fitment of the ridges into the waveguide transition.

### 5.6.2 The ridges

The ridges are machined on a 3-axis CNC mill. The CNC mill is programmed to follow the curve of the profile of the ridges of the parasolid file that is created in SolidWorks. The ridges are cut from standard, commercially available aluminium plates that have a thickness of 4.5 mm. One of the four ridges is shown in Figure 5.13.

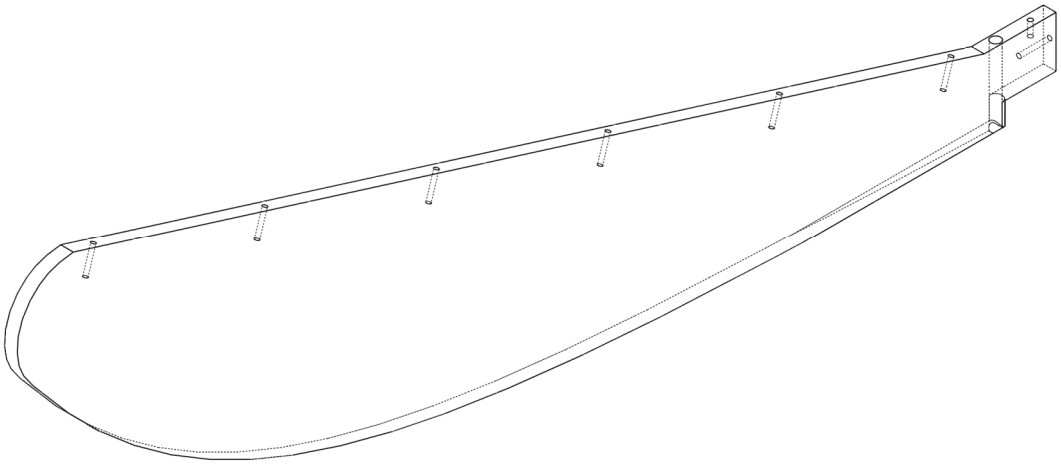

**Figure 5.13.** An isometric view of one of the four manufactured ridges.

The ridges are chamfered at the feed point where the four ridges are fitted closely together. The chamfer has a 45° angle and is cut by hand. The chamfer is only applied in the first section of the ridges and tapers out in a straight line in the boresight direction as shown in Figure 5.14. The chamfering prevents the ridges from touching each other close to the feed point. Threaded holes are cut into the ridges, so that the ridges can be attached to the waveguide transition and the sidewalls can be attached to the ridges.

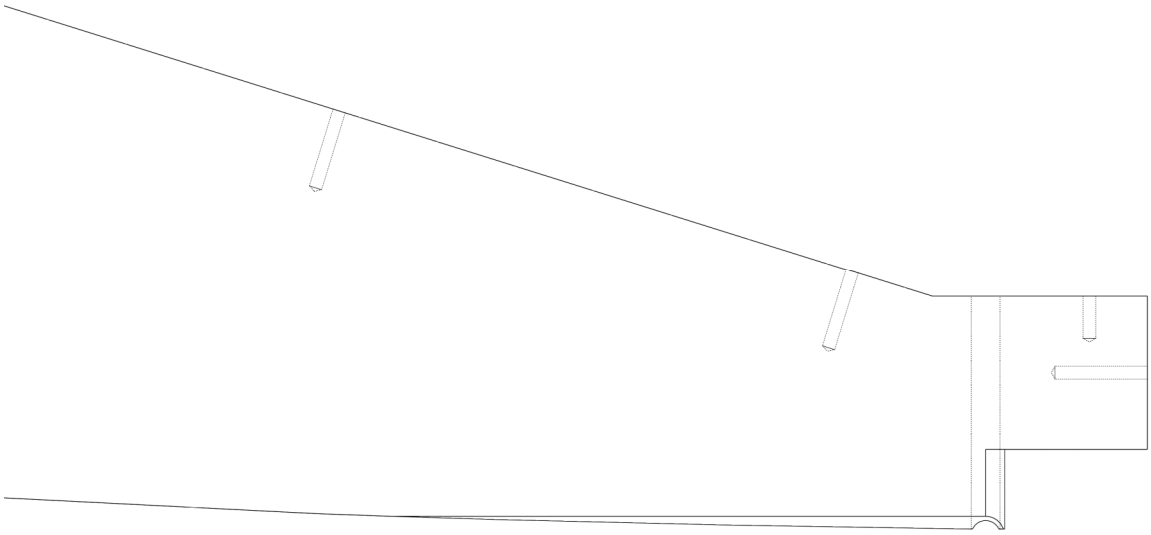

**Figure 5.14.** The detail of the chamfering of the ridges.

Two of the ridges have through-holes of 3.5 mm diameter cut into them at the feed points. In the other two ridges threaded holes of 1.4 mm diameter and 5 mm depth are cut into the ridges at the feed point. The two ridges with the 3.5 diameter holes are placed orthogonal to each other. The feed pins pass through the 3.5 mm holes and are screwed into the 1.4 mm threaded holes of the opposite ridges, as shown in Figure 5.15.

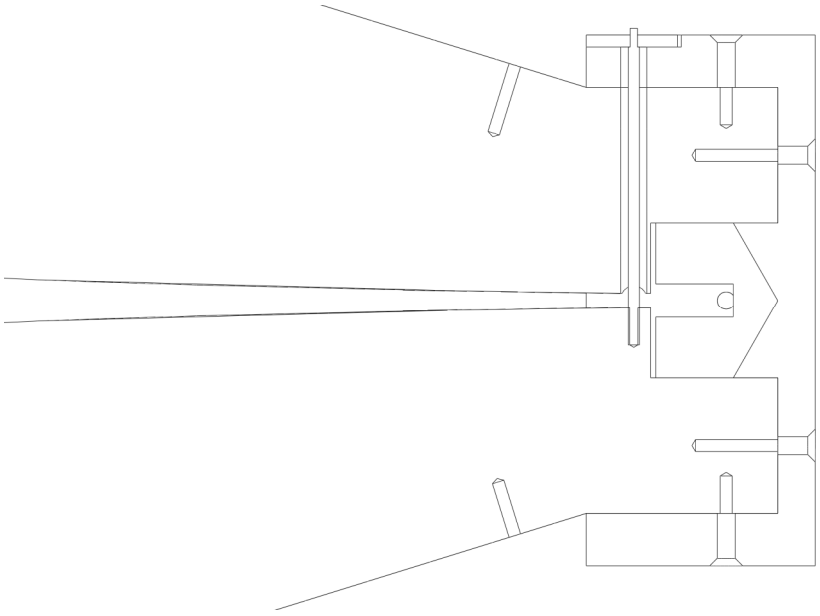

**Figure 5.15.** A section view through the assembly of one pair of ridges, one feed pin and the waveguide transition.

### 5.6.3 The feed pins

The feed pins are made from thin aluminium rods with diameters of 1.5 mm. They are machined on a conventional lathe. The total length of the feed pins is 42.4 mm. The diameter of the feed pin is cut down to 0.98 mm for 2.5 mm of the length at one end of the pin, as shown in Figure 5.16. The tips of the 0.98 mm sections are rounded so that they can slide into the tight collet of the Huber and Suhner SMA connectors. A 1.4 mm thread is cut, by hand, onto the opposite end of the pin with a dienut. It is shown in Figure 5.15 of the previous paragraph how the ridges and the feed pins are fitted together in an assembly with the waveguide transition. The feed pin is screwed into the one ridge by gripping the 0.98 mm diameter tip of the feed pin with the fingertips, and slowly turning it until the feed pin does not want to turn anymore. The 0.98 mm diameter tip is then slid into the collet of the SMA connector. The alignment of the feed pins and the connectors is ensured through the fitment of the connectors into the recessed squares that are cut into the sides of the waveguide transition.

**Figure 5.16**. The manufactured feed pin.

### 5.6.4 The sidewalls

The sidewalls are cut from standard size aluminium plates and sheets that are commercially available. The sidewalls are cut with a 3-axis CNC mill. Two of the sidewalls are cut from 1.2 mm sheets, while the other two sidewalls are cut from 4.5 mm plates. Threaded holes are cut into the sides of the thick sidewalls so that the thin sidewalls can be fastened to them with screws. Through-holes are also cut into the sidewalls so that they could be fastened to the ridges. The assembly of two of the sidewalls with the waveguide transition and two of the ridges is shown in Figure 5.17. The two sidewalls are fastened to each other as well.

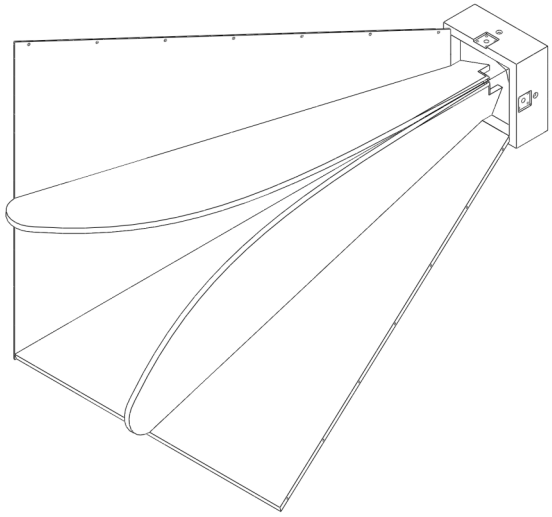

**Figure 5.17.** The partial assembly of the sidewalls, ridges and waveguide transition.

### 5.6.5 The assembly process

The steps of the assembly process are as follows:

i. The ridges are fitted into their slots in the waveguide transition. The ridges are fastened to the sides and the backplate of the waveguide transition with screws. Adjustments must be made to the ridges if the gaps between them are not equal, or if the ridges touch each other due to manufacturing tolerances. These adjustments can include scraping a little bit of metal off the ridges with a file or sandpaper at strategic positions. The gap between the ridges is a critical parameter and its dimensions must be checked to ensure that the desired performance is achieved.

ii. Insert the feed pins through the holes in the sidewalls of the transition section and the ridges with the 3.5 mm through-holes. Screw the feed pins into the other ridges with the 1.4 mm threaded holes. Attach the SMA connectors to the feed pins and fasten the connectors in their correct position in the recessed squares with screws. At this point it can be checked whether the feed pins touch each other. If they do, additional adjustments must be made.

iii. Fasten the thick sidewalls made from the aluminium plates to the ridges. Thereafter fasten the thin sidewalls to the ridges as well as to the thick sidewalls.

## 5.7 A comparison of the simulated and measured performance

The manufactured antenna is shown in Figure 5.18. It is tested in the Compact Antenna Test Range of the University of Pretoria as shown in Figure 5.19.

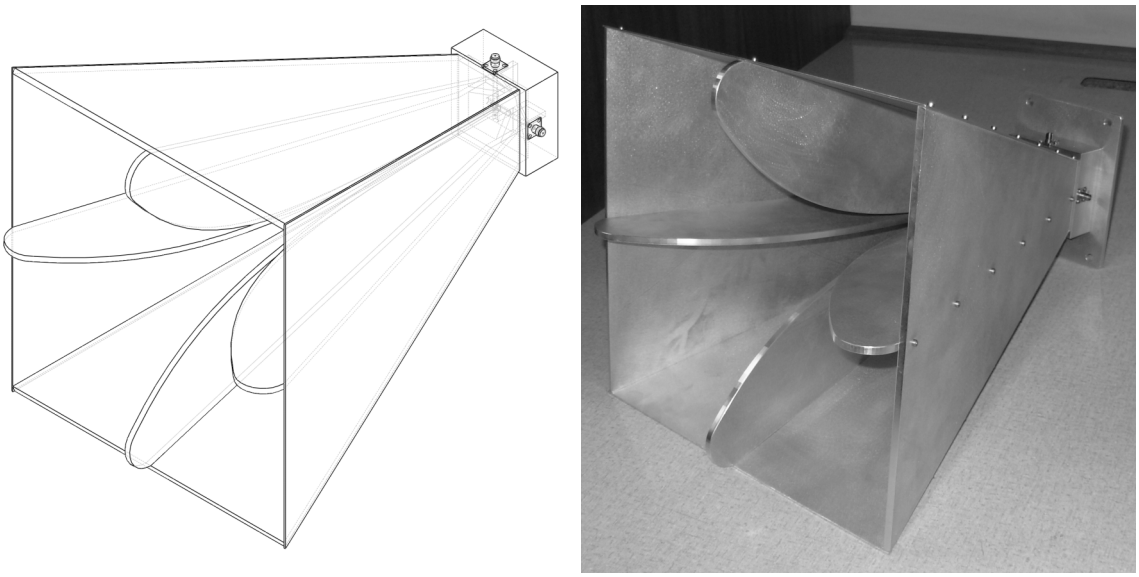

**Figure 5.18.** A machine drawing of the complete antenna (left) and the manufactured antenna (right).

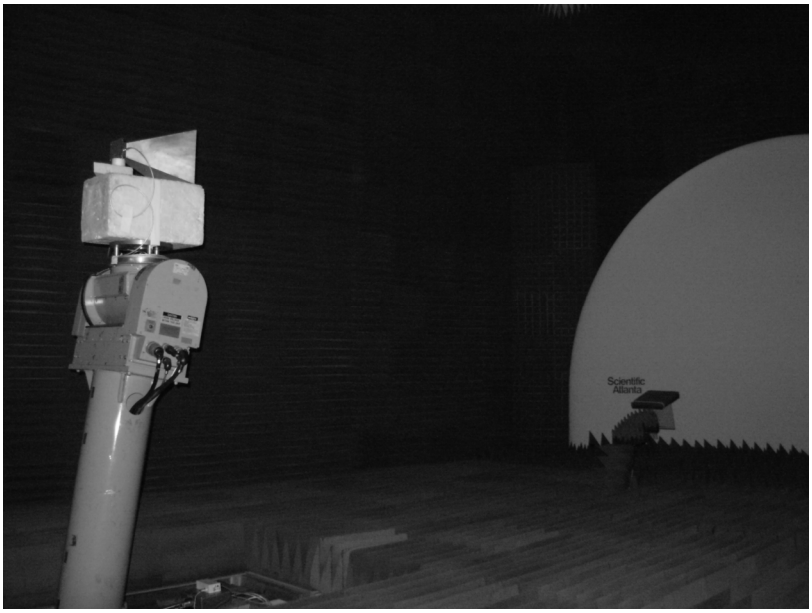

**Figure 5.19.** The antenna undergoing tests in the Compact Antenna Test Range of the University of Pretoria.

### 5.7.1 VSWR

The measured and simulated results for the VSWR for the complete antenna are shown in Figure 5.20 (port 1) and Figure 5.21 (port 2).

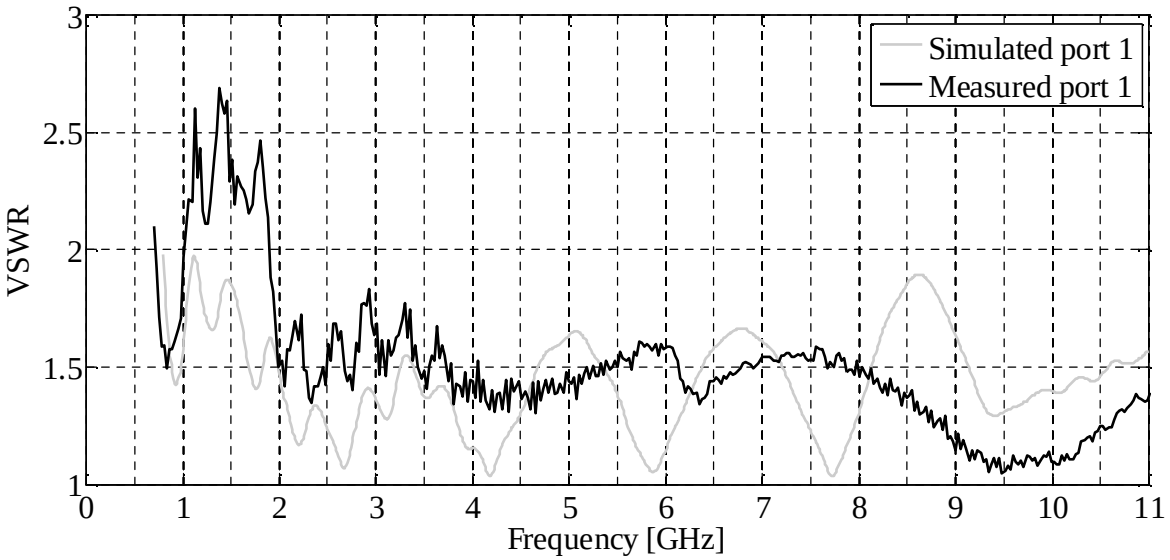


**Figure 5.20.** A comparison of the measured and simulated VSWR for port 1.

It can be seen from Figure 5.20 for port 1 that the maximum value for the VSWR is 2.7 in the measured results where it is 2 for the simulation results. The location of the first 3 peaks in the measured results compare well with the locations of the peaks in the simulated results. The differences in the VSWR at the lower frequencies between 0.8 and 2 GHz are ascribed to manufacturing tolerances, which cause the dimensions for the gap between the ridges to differ from the values in the simulations. It is shown in the parametric study of section 3.5.2 of Chapter 3 that the dimensions of the gap between the ridges is a critical parameter and even a slight difference in the gap dimension has a huge effect on the VSWR. It can be seen that the measured VSWR goes below 2 at approximately 1.9 GHz and stays below 2 across the rest of the bandwidth. Thus, the measured VSWR for port 1 is equal to or less than 2 for 88% of the bandwidth from 0.8 to 10 GHz. The measured VSWR actually remains below 2 for higher frequencies as well, but the operational bandwidth is limited by the gain performance as is shown later in this chapter. The simulated VSWR for port 1 is less than 2 across the entire 0.8 to 10 GHz bandwidth.

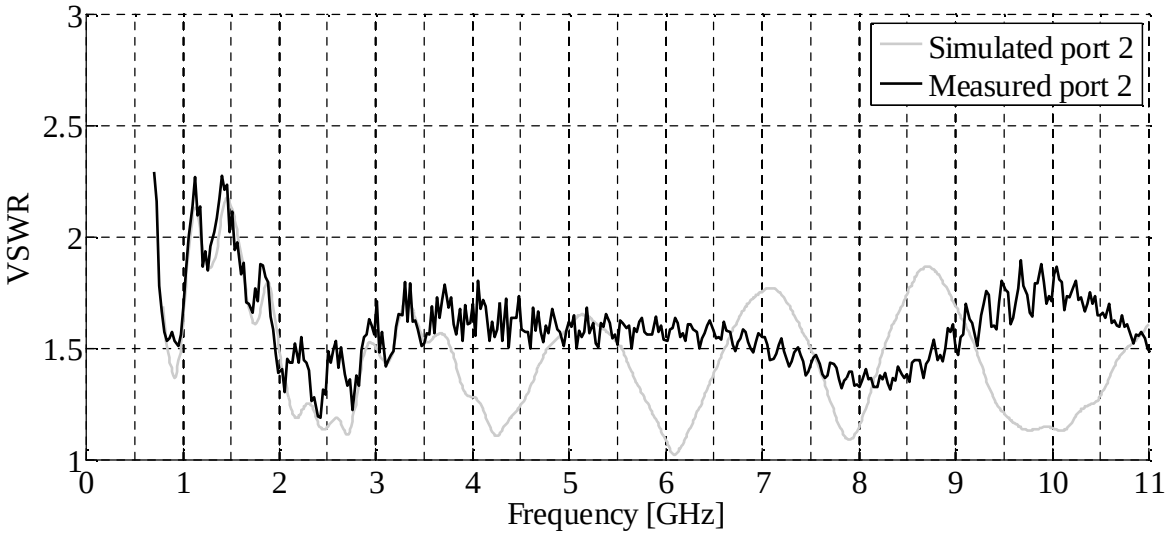


**Figure 5.21.** A comparison of the measured and simulated VSWR for port 2.

From Figure 5.21 for port 2 one can observe excellent agreement between the measured and the simulated results for the first three peaks in the VSWR between 0.8 and 3.5 GHz. Thereafter there is a larger difference between the results. However, the measured VSWR remains below 2 from 1.5 to 10 GHz. The measured VSWR remains below 2 for 92% of the 0.8 to 10 GHz bandwidth for port 2. The simulated VSWR is below 2 for 94% of this bandwidth. The maximum measured VSWR for port 2 is 2.3. The maximum simulated VSWR for port 2 is 2.2.

### 5.7.2 Coupling

The simulated and measured coupling between the ports of the complete antenna is shown in Figure 5.22. The measured coupling is below -25 dB from 0.8 to 2.5 GHz and from 2.5 GHz upwards it remains below -30 dB. Therefore, the measured coupling is below -30 dB for 82% of the 0.8 to 10 GHz bandwidth. The simulated coupling is below -30 dB across the entire 0.8 to 10 GHz bandwidth. It is very difficult to accurately measure signals that have amplitudes of less than -30 dB in the Compact Antenna Test Range facility. Special care has to be taken so that any reflections from surfaces in the measurement facility do not influence the measurements. Any asymmetry in the measurement set-up could also lead to differences between the simulated and measured results. Manufacturing tolerances could also contribute to the difference between the measured and simulated results, as it has been shown in section 3.5.6 that the offset between the ports has a significant influence on the amount of coupling between the ports.

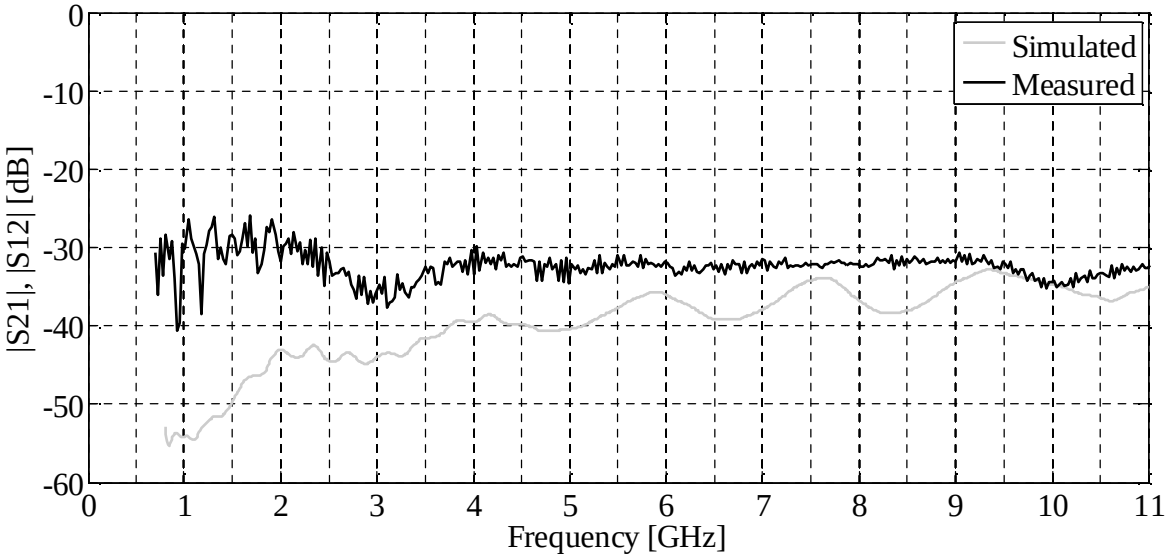


**Figure 5.22.** A comparison of the measured and simulated coupling between the ports.

### 5.7.3 Boresight gain

The measured and simulated values for the boresight gain of the complete antenna are shown in Figure 5.23 (port 1) and Figure 5.24 (port 2).

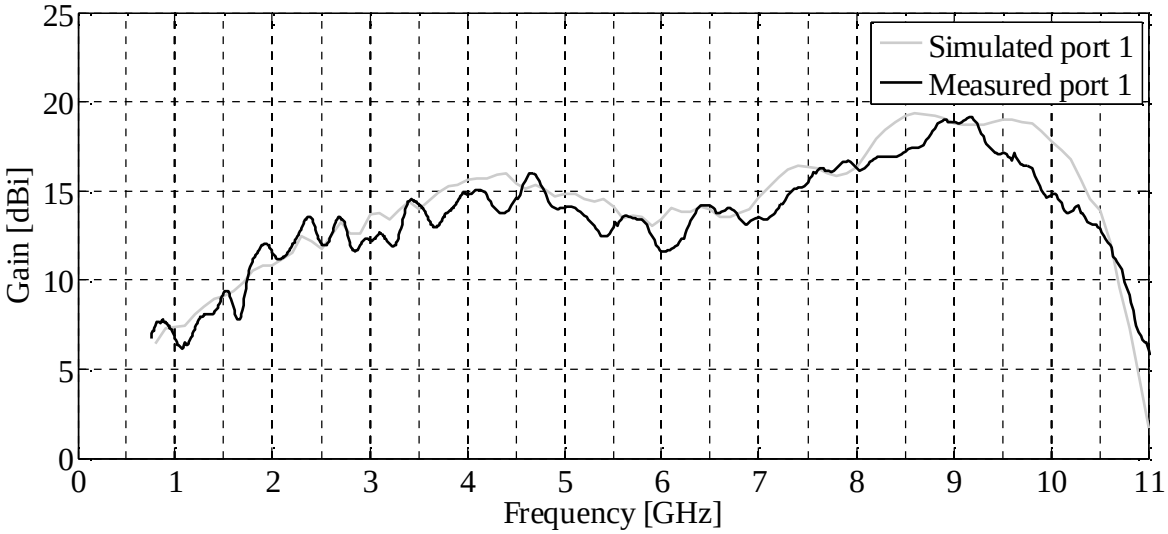


**Figure 5.23.** A comparison of the measured and simulated boresight gain for port 1.

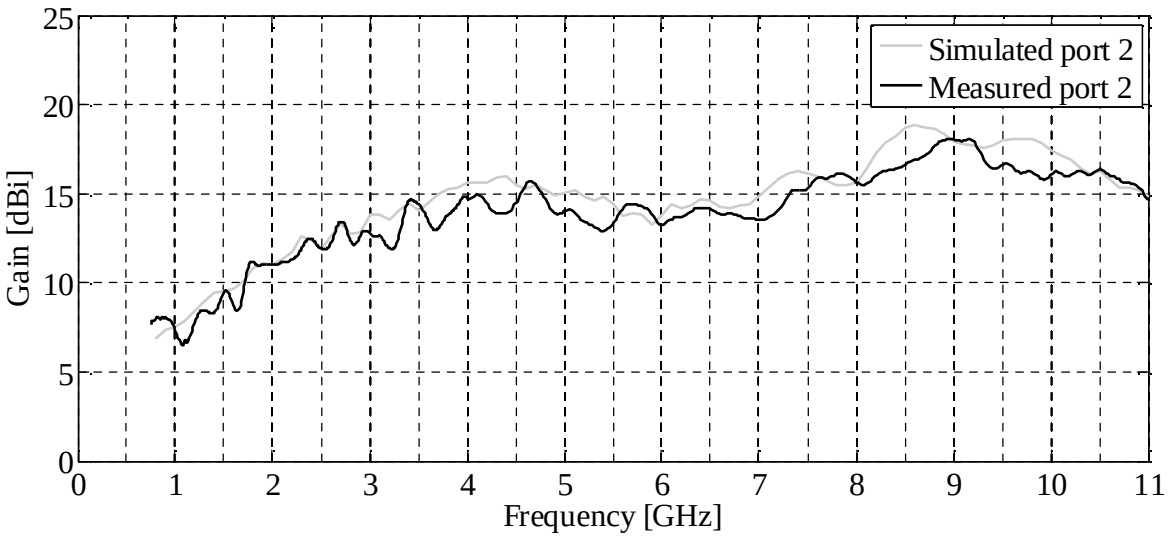


**Figure 5.24.** A comparison of the measured and simulated boresight gain for port 2.

It can be seen that there is good agreement between measured and simulated values in both sets of results. The measured results have a slightly larger variation in the gain when compared to the simulation results. The dips in the measured boresight gain are still less than 3 dBi across the 0.8 to 10 GHz bandwidth. The dips in the simulated boresight gain are less than 2 dBi. There is a large drop in the boresight gain for port 1 which starts at 9 GHz. This corresponds to the plots of the transmission coefficients of the modes inside configuration III for the transition section. It is shown in Figure 3.11 of Chapter 3 that at 9 GHz the higher order modes start to receive a significant amount of the input power. The value for $|S3_{TE\_n}1|$ of the higher order modes has a minimum at 11 GHz, which corresponds with the valley of the large drop in the boresight gain. Therefore, as soon as a significant amount of the input power is coupled into the higher order modes, a large dip in the boresight gain occurs, as is expected. It is shown that the electric fields of the higher order modes are not confined to the areas between the ridges. Consequently, the input power is radiated into directions that are not on boresight, causing the main beam to split into side beams with a resulting dip in the boresight gain. It can be seen that for port 2 this dip in gain does not occur, indicating that the higher order modes for port 2 only start to propagate at a higher frequency. Approximately the same boresight gain performance is achieved with both ports, except for frequencies higher than 9 GHz. At these frequencies the offset between the ports starts to produce different results.

It is concluded that the manufactured antenna delivers acceptable performance for both ports between 0.8 and 10 GHz in terms of the boresight gain. At 10 GHz the antenna has a

measured boresight gain of 15 dBi for port 1 and 16 dBi for port 2. The antenna is not considered functional above 10 GHz due to the drop in the gain for port 1. The measured gain range for port 1 is 6.2 to 19.2 dBi and 6.5 to 18 dBi for port 2.

### 5.7.4 Radiation patterns

The radiation patterns for port 1 of the complete antenna for 0.8, 1, 2, 4, 6, 8 and 10 GHz are shown in Figure 5.25 to Figure 5.31. As the radiation patterns for port 2 are very similar to those of port 1, they are not shown. The radiation patterns of the co-polarization (Co-pol) and cross-polarization (Cross-pol) are shown in both the E- and H-plane.

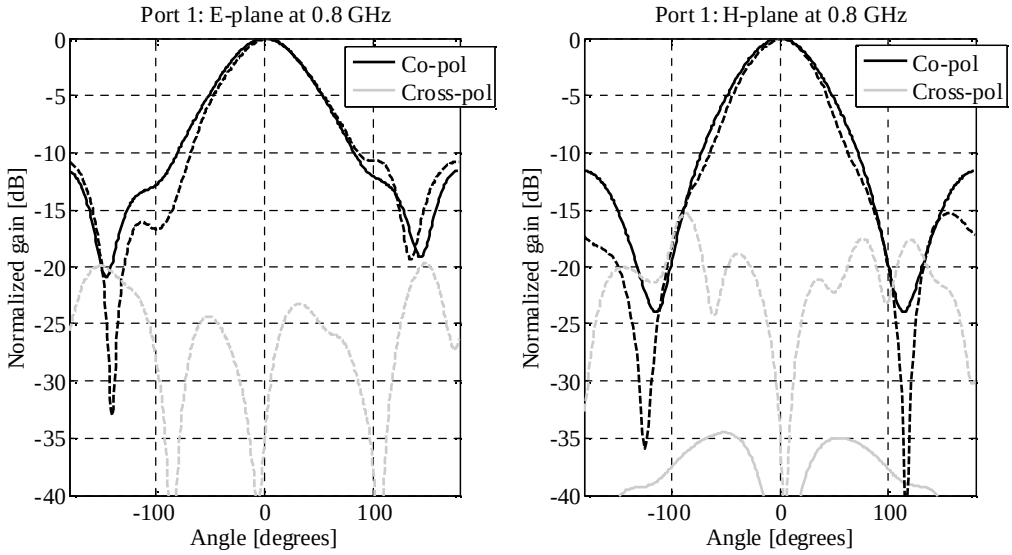


**Figure 5.25.** The simulated (solid lines) and measured (dashed lines) radiation patterns at 0.8 GHz.

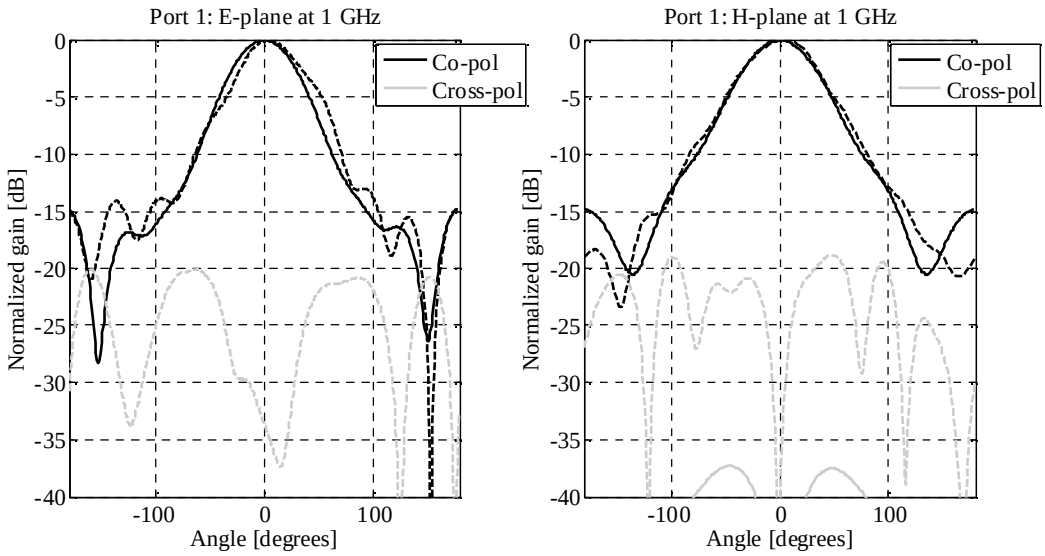


**Figure 5.26.** The simulated (solid lines) and measured (dashed lines) radiation patterns at 1 GHz.

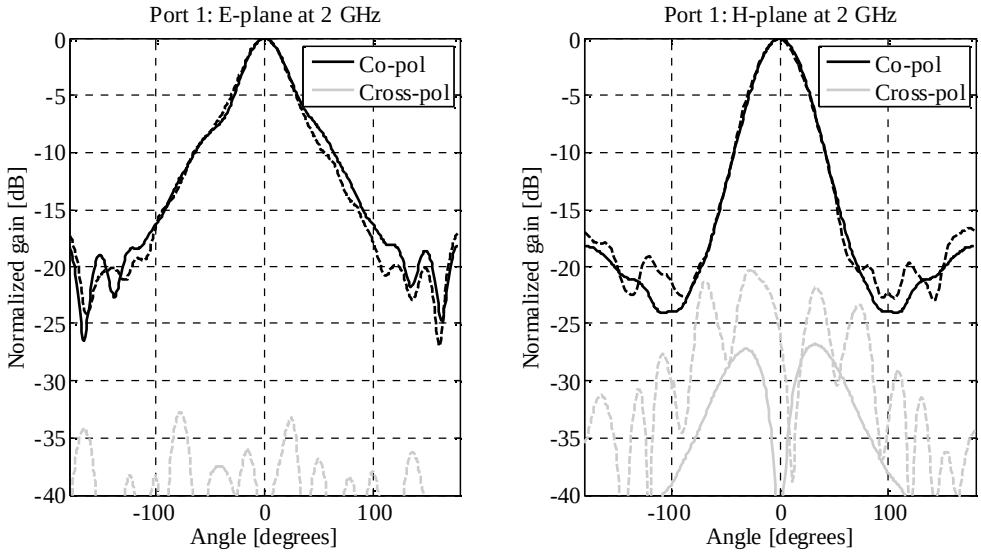


**Figure 5.27.** The simulated (solid lines) and measured (dashed lines) radiation patterns at 2 GHz.

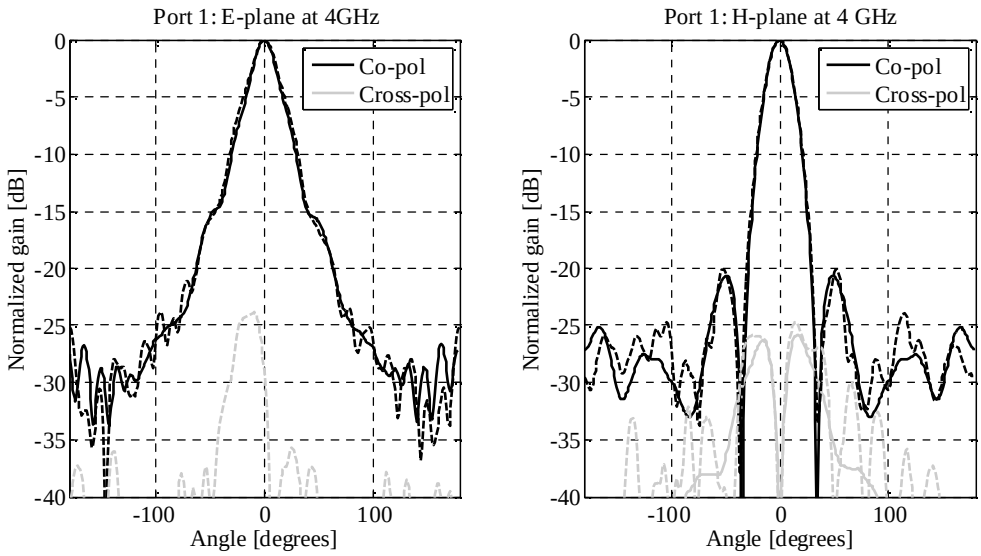


**Figure 5.28.** The simulated (solid lines) and measured (dashed lines) radiation patterns at 4 GHz.

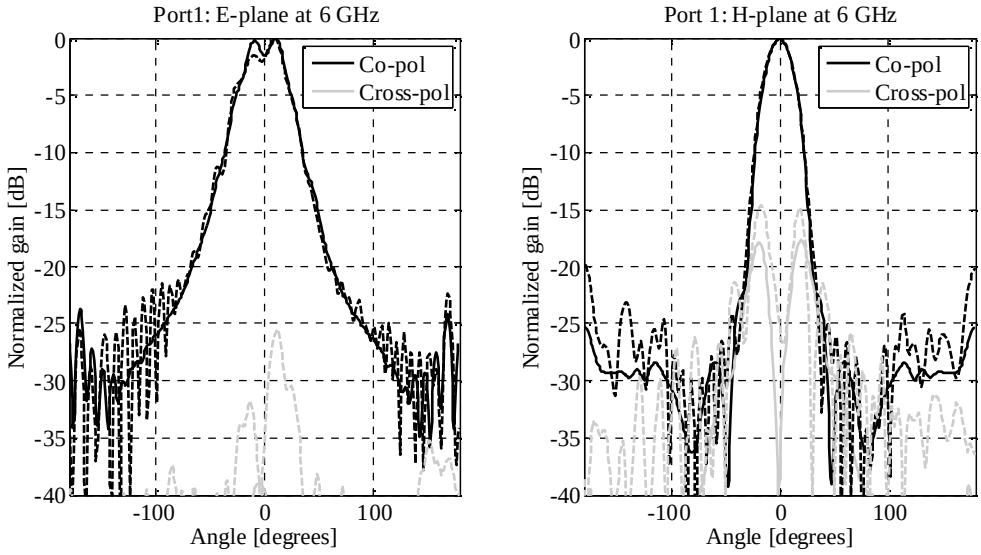


**Figure 5.29.** The simulated (solid lines) and measured (dashed lines) radiation patterns at 6 GHz.

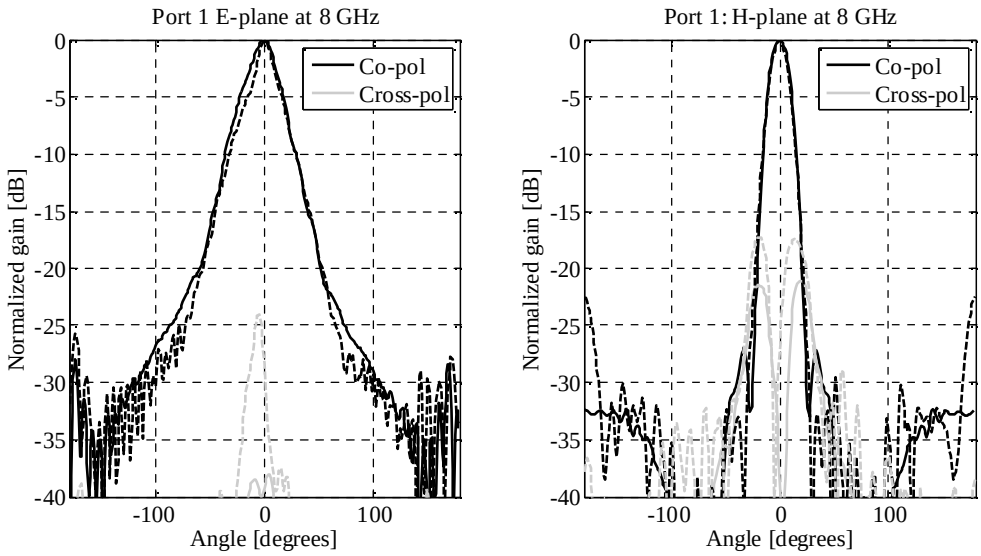


**Figure 5.30.** The simulated (solid lines) and measured (dashed lines) radiation patterns at 8 GHz.

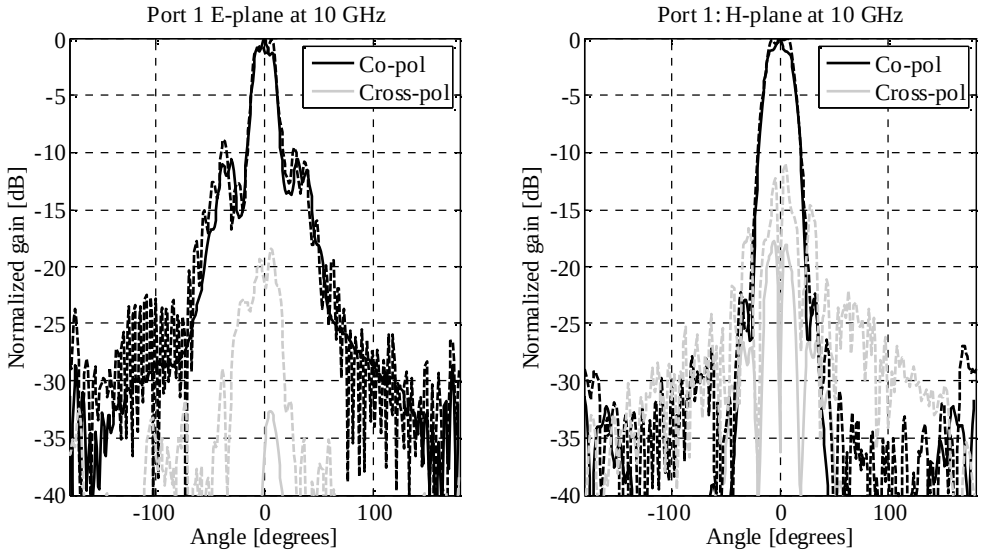


**Figure 5.31.** The simulated (solid lines) and measured (dashed lines) radiation patterns at 10 GHz.

It can be seen from Figure 5.25 to Figure 5.31 that good agreement is achieved between the measured and simulated results for the co-polarization in both the E- and H-plane. Almost exactly the same results are achieved for the main beam of radiation while the largest differences occur at the locations of the backlobes.

It is clear from the figures above that there are larger differences between the measured and simulated cross-polarization patterns, especially in the E-plane. They are ascribed to asymmetry in the measurement set-up, as well as manufacturing tolerances which lead to the manufactured antenna not being precisely symmetrical, as was the case in the simulated

model. The maximum level for the cross-polarization is still 10 dB below that of the co-polarization in the main beam, as shown in Figure 5.31. Across the rest of the bandwidth the cross-polarization is at least 15 dB lower than the co-polarization. At frequencies higher than 10 GHz there is a degradation in the radiation pattern performance as the higher order modes start to propagate.

It can be seen from Figure 5.29 that there is a slight break-up in the radiation pattern at 6 GHz in the E-plane. The main beam is slightly split into two sidelobes, indicated by the dip in the radiation pattern in the boresight direction. Therefore at 6 GHz is it concluded that a higher order mode is still being propagated even though a lot of effort is put into the suppression of the higher order modes inside the transition section. It can be observed from Figure 3.11 that at 6 GHz the transmission coefficient of the dominant modes starts to decrease slowly, which indicates that at 6 GHz some of the input energy is coupled to the higher order modes. Thus, the higher order modes are not entirely suppressed. However, as can be seen from the boresight gain plot in Figure 5.3, when a transition section is used where the higher order modes are not suppressed at all, there is a very large dip (larger than 10 dBi) in the boresight gain. This is in comparison to the 2 dBi dip in the gain for the manufactured antenna at 6 GHz as shown in Figure 5.23.

## 5.8 Summary

In this chapter the performance of the complete antenna was evaluated. The complete antenna was a combination of the transition and flared horn sections. It was firstly shown how the performance of the antenna with the best transition and flared horn section compared to the performance of antennas where another configuration was used for either the transition or the flared horn section. It was already discussed that configuration III with a pyramidal cavity and steps was the best configuration to use for the transition section. The configuration with an exponential profile with a circular segment for the ridges was the best configuration to use for the flared horn section. In the final design of the complete antenna the best transition and flared horn sections were combined.

A comparison was made between two antennas where in one case configuration I was used for the transition section and in the other case configuration III. The best flared horn

section was used for both antennas. It was shown that there was a large dip in the boresight gain between 5.7 and 6.5 GHz when configuration I for the transition section was used. It was shown in chapter 3 in the plots for the transmission coefficients that for configuration I the higher order modes received a significant amount of the input power at 5.6 GHz and started to propagate at this frequency. Thus, the first dip in the gain corresponds well with the frequency point where the higher order modes started to propagate in the transition section. The large dip in the boresight gain between 5.7 and 6.5 GHz was not present when configuration III for the transition section was used, as was expected. It was shown in chapter 3 in the plots for the transmission coefficients that the first higher order modes started to propagate at 9 GHz in configuration III of the transition section. The drop in gain for the complete antenna from 9 GHz onwards corresponds well with the 9 GHz frequency point where the higher order modes started to propagate in configuration III. It was therefore concluded that the transmission coefficients of the modes inside the transition section could be used to make predictions for the boresight gain performance of the complete antenna.

Another comparison between two antennas was made where two different configurations were used for the flared horn section. The best transition section was used for both antennas. In the one case an elliptical profile was used for the ridges in the flared horn section and in the other case an exponential profile with a circular segment. The antenna where an exponential profile with a circular segment for the ridges was used delivered the best VSWR performance. This was expected, since it was shown in chapter 4 that this configuration for the flared horn section delivered the best VSWR performance compared to that of the other configurations with different profiles for the ridges. The difference in the boresight gain performance of the two antennas was not significant. Therefore, the choice of profile used in the flared horn section had a significant influence on the VSWR but not on the gain performance of the complete antenna.

The VSWR performance of the best transition and flared horn sections were compared to that of the final design complete antenna. It was shown that the VSWR of the transition section determined the VSWR of the complete antenna at the higher frequencies of the bandwidth. The VSWR of the flared horn section determined the VSWR performance of the complete antenna at the lower frequencies of the bandwidth. In the middle of the

bandwidth the performance of the complete antenna was a combination of the performance of the two sections. It was also shown that time and memory resources could be saved if the transition or flared horn sections were simulated on their own, instead of simulating them as part of the complete antenna. Thus, it was faster to optimize the transition and flared horn sections separately and to combine them in the final design of the complete antenna, rather than to optimize the complete antenna by modifying the transition and flared horn sections as part of the complete antenna.

A comparison was made between the results achieved with CST Microwave Studio and FEKO when the final design of the complete antenna was simulated. Good agreement was achieved between the results of the two software packages. This verified the simulation results achieved with CST Microwave Studio.

The details of the mechanical implementation of the final design of the complete antenna were given. Thereafter the measured results were compared to the simulated results. The operational bandwidth of the final design was from 0.8 to 10 GHz, i.e. a 12.5:1 bandwidth. A simulated VSWR of less than 2 over the entire bandwidth was achieved for port 1. The simulated VSWR was less than 2 over 94% of the bandwidth with a maximum simulated VSWR of 2.2 for port 2. The simulated coupling between the ports was less than -30 dB over the entire bandwidth. Similar gain curves were achieved for both ports. The simulated boresight gain was relatively stable with no dips larger than 2 dBi. The range for the simulated gain was between 6.4 and 19.4 dBi for port 1 and between 6.8 and 18.9 dBi for port 2. The maximum measured VSWR over the 0.8 to 10 GHz bandwidth was 2.7 and 2.3 for port 1 and port 2 respectively. The measured VSWR was less than 2 for 88% and 92% of the bandwidth for port 1 and port 2 respectively. The measured coupling between the ports was below -25 dB from 0.8 to 2.5 GHz and below -30 dB across the rest of the bandwidth. The measured coupling was below -30 dB for 82% of the 0.8 to 10 GHz bandwidth. A relatively stable measured boresight gain curve with no dips larger than 3 dBi was achieved. There was a large drop in the measured gain at 10 GHz for port 1, which limited the operational bandwidth. The range for the measured gain was 6.2 to 19.2 dBi for port 1 and 6.5 to 18 dBi for port 2. Similar gain curves were achieved for the two ports. Good agreement was achieved between the measured and simulated results for the VSWR as well as the boresight gain. It was shown that good agreement was achieved between the

measured and simulated radiation patterns for the co-polarization. There were larger differences between the measured and simulated radiation patterns for the cross-polarization, as expected. The differences between the simulated and measured results could be ascribed to manufacturing tolerances as well as a slight asymmetry in the measurement set-up.

# CHAPTER 6 CONCLUSION

## 6.1 General conclusions

The main objective of this dissertation was to improve the performance of a dual-polarized, quad-ridged horn antenna with pyramidal sidewalls. The aim was to develop an antenna with a VSWR of less than 2 and a stable boresight gain across the widest possible bandwidth. The boxed dimensions of the antenna design of [17], in terms of wavelength at the lowest frequency of operation, were used as a benchmark. An optimized design of the antenna was developed through the application of the technique to separate the antenna into the transition and flared horn sections and to optimize these sections individually through simulation. The individual sections and the complete antenna were simulated with the FIT of the time domain solver of CST Microwave Studio.

Different configurations for the transition and flared horn sections were investigated to determine which configuration delivered the best performance. The best configuration for the transition and flared horn sections were combined in the final design of the complete antenna. Three configurations to use for the transition section were investigated. The configurations differed in the shape of the cavity and the inclusion of steps that connected the ridges to the backshort. All three configurations were optimized. The aim of the optimization was to achieve a VSWR of less than 2 and to suppress the excitation of higher order modes across the widest possible bandwidth. It was found that the configuration where a pyramidal cavity and steps were used delivered the best performance. The steps helped to suppress the excitation of higher order modes, which consequently led to a stable boresight gain, with no large dips, being achieved for the complete antenna. A parametric study was performed on the best transition section to determine the effect of manufacturing tolerances on the performance. It was shown that the gap between the ridges had a significant effect on the performance across the entire bandwidth and therefore the tolerance of this parameter should be made as small as possible during manufacturing to achieve the desired performance.

A parametric study was performed on the flared horn section to determine whether a design for the complete antenna that had smaller boxed dimensions than the benchmark could be obtained. It was determined that the optimum dimensions for the flared horn

section delivered a complete antenna that had the same boxed dimensions as those of [17]. Four profiles for the ridges were investigated in the flared horn section to determine which configuration delivered the lowest VSWR across the widest bandwidth. It was found that an exponential profile with a circular segment for the ridges delivered the best performance. This configuration was thus used for the flared horn section of the final design of the complete antenna.

The best transition and flared horn sections were combined in the final design of the complete antenna. The final design was simulated. A comparison was made between the optimized antenna and two other antennas where one of the other configurations was used for either the transition or flared horn sections. This comparison confirmed that, when the transition section with the pyramidal cavity and steps was combined with the flared horn section with the exponential profile with a circular segment for the profile for the ridges, the best performance was achieved. The accuracy of the results achieved with CST Microwave Studio was verified by a comparison of the results achieved with a simulation of the optimized antenna in FEKO.

The optimized antenna had the same boxed dimensions as the benchmark design of [17]. A 13.25:1 bandwidth was achieved with the published design of [17] with a VSWR of less than 3 specification. The maximum measured VSWR of the published design was 3 and 2.5 for the front and back ports respectively. The measured VSWR of the published design was below 2 for 41% and 65% of the operational bandwidth for the respective ports. The measured coupling between the ports was below -25 dB over almost the entire operational bandwidth. The measured coupling for the published design was below -30 dB for approximately 57% of its bandwidth. Only a few values for the measured boresight gain of the published design were presented in [17] and it was unclear whether the published design suffered from large dips in its gain. The range for the measured boresight gain of the published design was 6.4 to 16.1 dBi.

The final design of the optimized antenna was simulated. The optimized antenna had a 12.5:1 operational bandwidth from 0.8 to 10 GHz. Across this bandwidth the simulated maximum VSWR for port 1 was less than 2. The simulated maximum VSWR for port 2 was 2.2. The simulated VSWR for port 2 was less than 2 for 94% of the bandwidth. A

simulated coupling of less than -30 dB was achieved over the entire operational bandwidth. A relatively stable boresight gain was achieved. The dips in the simulated gain were smaller than 2 dBi. The gain curves for the two input ports were very similar. The range for the simulated gain was between 6.4 and 19.4 dBi for port 1 and between 6.8 and 18.9 dBi for port 2.

A prototype of the final design was built and the performance of the antenna was measured. Across the 0.8 to 10 GHz bandwidth a measured maximum VSWR of 2.7 and 2.3 was achieved for port 1 and port 2 respectively. The measured VSWR was equal or less than 2 for 88% and 92% of the bandwidth for the respective ports. The measured coupling between the ports was below -25 dB from 0.8 to 2.5 GHz and below -30 dB over the rest of bandwidth. The measured coupling was below -30 dB for 82% of the bandwidth. The measured boresight gain of the prototype was relatively stable with no sudden dips larger than 3 dBi. The range for the measured gain was between 6.2 and 19.2 dBi for port 1 and between 6.5 to 18 dBi for port 2. The gain performance of the two input ports was very similar. The operational bandwidth of the prototype was limited by higher order modes that started to propagate. The higher order modes caused a break-up in the main beam of the antenna with a consequent drop in the gain at 10 GHz. The simulated and measured radiation patterns of the optimized antenna were also shown. Overall, good agreement was achieved between the simulated and measured results. The differences in the simulated and measured VSWR performance were ascribed mainly to manufacturing tolerances. It was concluded that manufacturing tolerances as well as a slight asymmetry in the measurement set-up produced the differences in the simulated and measured coupling between the ports, as well as the radiation patterns.

It was concluded from the discussion above on the performance of the published design of [17] and the optimized antenna that an improvement in the performance of a quad-ridged horn antenna with pyramidal sidewalls was achieved. Thus the technique to improve the performance of the complete antenna, by separating the antenna into the transition and flared horn sections and to optimize the performance of the sections individually, was successful.

## 6.2 Future research

Possible research topics for the future that were identified during the course of this study are listed below.

- An investigation into what other modifications could be made to the transition section to further suppress higher order modes. This could lead to a possible further extension of the bandwidth, as it was found during the measurement phase that the bandwidth of the antenna was limited due to the drop in gain at 10 GHz caused by the excitation of higher order modes.
- An investigation into whether the technique of optimizing the transition and flared horn sections individually in order to optimize the performance of the complete antenna could be applied to the variations of the antenna with conical or shaped sidewalls as well as the open- and super-open-boundary variations of the antenna.
- An investigation to determine whether the use of gridded sidewalls in the flared horn section could help to improve the radiation performance of quad-ridged horn antennas.

# REFERENCES

[1] K.L. Walton and V.C. Sundberg, "Broadband ridged horn design," *Microwave Journal*, pp. 96-101, Mar. 1964.

[2] S.B. Cohn, "Properties of ridge waveguide," *Proceedings of the IRE*, vol. 35, no. 8, pp. 783-788, Aug. 1947.

[3] S.B. Cohn, "Design of simple broad-band wave-guide-to-co-axial-line junctions," *Proceedings of the IRE*, vol. 35, no. 9, pp. 920-926, Sep. 1947.

[4] S. Hopfer, "The design of ridged waveguides," *IRE Transactions on Microwave Theory and Techniques*, vol. 3, no. 5, pp. 20-29, Oct. 1955.

[5] P.J. Muenzer, "Broadbanding coax to ridged waveguide transitions," *Microwaves*, vol. 8, pp. 92-97, Aug. 1964.

[6] W.J.R. Hoefer and M.N. Burton, "Analytical expressions for the parameters of ridged and finned waveguides," *IEEE MTT-S International Microwave Symposium Digest*, pp. 311-313, 1982.

[7] W. Sun and C.A. Balanis, "MFIE analysis and design of ridged waveguides," *IEEE Transactions on Microwave Theory and Techniques*, vol. 41, no. 11, pp. 1965-1971, Nov. 1993.

[8] D.A. Jarvis and T.C. Rao, "Design of double ridged rectangular wave guide of arbitrary aspect ratio and ridge height," *IEE Proceedings on Microwaves, Antennas and Propagation*, vol. 147, pp. 31-34, Feb. 2000.

[9] W. Sun and C.A. Balanis, "Analysis and design of quadruple-ridged waveguides," *IEEE Transactions on Microwave Theory and Techniques*, vol. 42, no. 12, pp. 2201-2207, Dec. 1994.

[10] Y. Tang, J. Zhao, and W. Wu, "Mode-matching analysis of quadruple-ridged square waveguides," *Microwave and Optical Technology Letters*, vol. 47, no. 2, pp. 190-194, Oct. 2005.

[11] Y. Tao, Z. Shen, and G. Liu, "Efficient analysis of quadruple corner-cut ridged circular waveguide by hybrid mode-matching boundary-element method," *IEEE Transactions on Magnetics*, vol. 45, no. 3, pp. 1706-1709, Mar. 2009.

[12] J.L. Kerr, "Short axial length broad-band horns," *IEEE Transactions on Antennas and Propagation*, vol. 21, no. 5, pp. 710-714, Sep 1973.

[13] B. Jacobs, J.W. Odendaal, and J. Joubert, "An improved design for a 1-18 GHz double ridged guide horn antenna," *IEEE Transactions on Antennas and Propagation*, vol. 60, no. 9, pp. 4410-4418, Sep. 2012.

[14] V. Rodriguez, "A multi-octave, open-boundary, quad-ridge horn antenna for use in the S- to Ku-bands," *Microwave Journal*, vol. 49, no. 3, pp. 84-92, Mar. 2006.

[15] F. King, J.S. Yee and D.R. Erbach, “A broadband quadruple-ridged waveguide radiator,” Army Missile Research, Development and Engineering Laboratory, Alabama, RE-74-7, Jun. 1974.

[16] S.A. Soroka, “A physically compact quad ridge horn design,” in *Proceedings of the Antennas Propagation Society International Symposium*, Jun. 1986, vol. 24, pp. 903-906.

[17] Z. Shen and C. Feng, “A new dual-polarized broadband horn antenna,” *IEEE Antennas and Wireless Propagation Letters*, vol. 4, pp. 270-273, 2005.

[18] J. Qiu, Y. Suo, and W. Li, “Research and design on ultra-wideband dielectric hemispheric lens loaded quad-ridged horn antenna,” in *Proceedings of the International Conference on Antenna Theory and Techniques*, 17-21 Sep. 2007, Sevastopol, Ukraine, pp. 253-255.

[19] J. Qiu, Y. Suo, W. Li, “Design and simulation of ultrawideband quad-ridged horn antenna,” in *Proceedings of the International Conference on Microwave and Millimeter Wave Technology*, Builin, China, Apr. 2007, pp. 1-3.

[20] M. Gilbert, K. Higgins, and L. Romero, “Quad-ridge horn utilizing resistive films to reduce sidelobes,” in *Proceedings of the IEEE Antennas and Propagation Society International Symposium*, 9-15 Jun. 2007, pp. 5684-5687.

[21] R. Dehdasht-Heydari, H. Hassani, and A. Mallahzadeh, “Quad ridged horn antenna for UWB applications,” *Progress in Electromagnetics Research*, vol.79, pp. 23-38, 2008.

[22] R. Dehdasht-Heydari, H. Hassani, and A. Mallahzadeh, “A new 2-18 GHz quad-ridged horn antenna,” *Progress in Electromagnetics Research*, vol. 81, pp. 183-195, 2008.

[23] A. Rojatkar and S. Ananthakrishnan, “Quad-Ridge horn antenna analysis and design for radio astronomy applications,” in *Proceedings of the Indian Antenna Week*, 18-22 Dec 2011, Kolkata, India, pp. 1-4.

[24] A.R. Mallahzadeh, A.A. Dastranj and F. Karshenas, “Pattern squint elimination for quad-ridged conical and pyramidal horn antennas using bended probes,” *International Journal of RF and Microwave Computer-Aided Engineering*, vol. 20, no. 1, pp. 94-102, Jan. 2010.

[25] H. Lai, R. Franks, D. Kong, D. Kuck, and T. Gackstetter, “A broad band high efficient quad ridged horn,” in *Proceedings of the IEEE Antennas and Propagation Society International Symposium*, Jun. 1987, vol. 25, pp. 676-679.

[26] A.R. Mallahzadeh, A.A. Dastranj, and S. Akhlaghi, “Quad-ridged conical horn antenna for wideband applications,” *International Journal of RF Microwave and Computer-Aided Engineering*, vol. 19, no. 5, pp. 519-528, 2009.

[27] R.J. Bauerle, R. Schrimpf, E.Gyorko, and J. Henderson, “The use of a dielectric lens to improve the efficiency of a dual-polarized quad-ridge horn from 5 to 15

GHz," *IEEE Transactions on Antennas and Propagation*, vol. 57, no. 6, pp. 1822-1825, Jun. 2009.

[28] A. Akgiray, S. Weinreb, and W.A. Imbriale, "Design and measurements of dual-polarized wideband constant-beamwidth quadruple-ridged flared horn," in *Proceedings of the IEEE International Symposium on Antennas and Propagation*, 3-8 July 2011, Spokane, Washington, pp. 1135-1138.

[29] W.A. Imbriale and A. Akgiray, "Performance of a quad-ridged feed in a wideband radio telescope," in *Proceedings of the European Conference on Antennas and Propagation*, Apr. 2011, Rome, Italy, pp. 662-665.

[30] A. Akgiray and S. Weinreb, "Ultrawideband square and circular quad-ridge horns with near-constant beamwidth," in *Proceedings of the IEEE International Conference on Ultra-Wideband*, 17-20 Sept. 2012, Syracuse, New York, USA, pp. 518-522.

[31] O.B. Jacobs, J.W. Odendaal, and J. Joubert, "Quad ridge horn antenna with elliptically shaped sidewalls," in *Proceedings of the International Conference on Electromagnetics in Advanced Applications*, 12-16 Sep. 2011, Torino, Italy, pp. 259-262.

[32] O.B. Jacobs, J.W. Odendaal, and J. Joubert, "Elliptically shaped quad-ridge horn antennas as feed for a reflector," *IEEE Antennas and Wireless Propagation Letters*, vol. 10, pp. 756-759, Jul. 2011.

[33] V. Rodriguez, "An open-boundary quad-ridged guide horn antenna for use as a source in antenna pattern measurement anechoic chambers," *IEEE Antennas and Propagation Magazine*, vol. 48, no. 2, pp. 157-160, Apr. 2006.

[34] F.F. Dubrovka and S.I. Piltyay, "A high performance ultrawideband orthomode transducer and a dual-polarized quad-ridged horn antenna based on it," in *Proceedings of the International Conference on Antenna Theory and Techniques*, 20-23 Sep. 2011, Kyiv, Ukraine, pp.176-178.

[35] O. Franek and G.F. Pedersen, "Spherical horn array for wideband propagation measurements," *IEEE Transactions on Antennas and Propagation*, vol. 59, no. 7, pp. 2654-2660, Jul. 2011.

[36] O.S. Kim, S. Pivnenko, and O. Breinbjerg, "Wideband scalable probe for spherical near-field antenna measurements," in *Proceedings of the European Conference on Antennas and Propagation*, 11-15 Apr. 2011, Rome, Italy, pp. 1781-1785.

[37] A. Giacomini, A. Potenza, R. Morbidini, and L. Foged, "Quad-ridge dual polarized antenna for use in the 2-32GHz band," in *Proceedings of the European Conference on Antennas and Propagation*, 26-30 Mar. 2012, Prague, Czech Republic, pp. 769-772.

[38] V. Rodriguez, "Open boundary quadridge horn antenna for the 80 MHz to 1 GHz range: A dual polarized solution for testing antennas in the VHF and UHF ranges," in *Proceedings of the European Conference on Antennas and Propagation*, 12-16 April 2010, Barcelona, Spain, pp. 1-4.

[39] V. Rodriguez, "Super-open-boundary quadridge horn antennas," in *Proceedings of the IEEE International Symposium on Antennas and Propagation*, 3-8 July 2011, Spokane, Washington, USA, pp. 1251-1253.

[40] G. Virone, R. Sarkis, C. Craeye, G. Addamo, and O.A. Peverini, "Gridded Vivaldi Antenna Feed System for the Northern Cross Radio Telescope," *IEEE Transactions on Antennas and Propagation*, vol. 59, no. 6, pp. 1963-1971, Jun. 2011.

[41] Computer Simulation Technology (CST), "CST Microwave Studio," 2013, http://www.cst.com/Content/Products/MWS/Overview.aspx. Last accessed on 7 Feb. 2013.

[42] EM Software and Systems (EMSS), "Numerical methods," 2013, http://www.feko.info/product-detail/numerical_methods. Last accessed on 7 Feb. 2013.

[43] ANSYS, "ANSYS HFSS features," 2013, http://www.ansys.com/Products/Simulation+Technology/Electromagnetics/High-Performance+Electronic+Design/ANSYS+HFSS/Features. Last accessed on 7 Feb. 2013.

[44] T. Weiland, M. Timm, and I. Munteanu, "A practical guide to 3-D simulation," *IEEE Microwave Magazine*, vol. 9, no. 6, pp. 62-75, Dec. 2008.

[45] D.B. Davidson, *Computational electromagnetics for RF and microwave engineering*, Cambridge University Press, 2005.

[46] Huber and Suhner, "Data sheet coaxial panel connector: 23_SMA-50-0-167/199_N," Document number: DOC-0000188276I, Oct. 2010.

[47] J.A.G. Malherbe, "Extreme performance TEM horn," *Microwave and Optical Technology Letters*, vol. 50, no. 8, pp. 2121-2125, Aug. 2008.

[48] V. Rodriguez, "Dual ridge horn antenna," U. S. Patent 6 995 728 B2, Feb. 2006.

[49] M. Abbas-Azimi, F. Arazm, J. Rashed-Mohassel, and R. Faraji-Dana, "Design and optimization of a new 1-18 GHz double ridged guide horn antenna," *Journal of Electromagnetic Waves and Applications*, vol. 21, no. 4, pp. 501-516, 2007.

[50] D.E. Baker and C.A. van der Neut, "A compact, broadband, balanced transmission line antenna derived from double ridged waveguide," in *Proceedings of the Antennas and Propagation Society International Symposium*, 22-24 May 1982, pp. 568-571.